Aquatic Gravity Currents Through Emergent Vegetation

by

Yukie Tanino

S.B., Environmental Engineering Science (2003)
Massachusetts Institute of Technology

Submitted to the Department of Civil and Environmental Engineering
in partial fulfillment of the requirements for the degree of

Master of Science in Civil and Environmental Engineering

at the

MASSACHUSETTS INSTITUTE OF TECHNOLOGY

September 2004

Signature of Author .....
Department of Civil and Environmental Engineering
29 July 2004

Certified by .....
Heidi M. Nepf
Associate Professor of Civil and Environmental Engineering
Thesis Supervisor

Accepted by .....
Heidi M. Nepf
Chairman, Department Committee on Graduate Students

Aquatic Gravity Currents Through Emergent Vegetation

by

Yukie Tanino

Submitted to the Department of Civil and Environmental Engineering
on 29 July 2004, in partial fulfillment of the
requirements for the degree of
Master of Science in Civil and Environmental Engineering

Abstract

Differential heating and cooling can generate density-driven, lateral exchange flows in aquatic systems. Despite the ubiquity of wetlands and other types of aquatic canopies, few studies have examined the hydrodynamic effects of aquatic vegetation on these currents. This study investigates the dynamics of lock-exchange flows, a particular class of density currents, propagating through rigid emergent vegetation. First, previous mathematical formulation is extended to develop theoretical models of vegetated lock-exchange flows. The regime in which stem drag is inversely proportional to velocity is considered as a special case.

Lock-exchange flows were generated in a laboratory flume with rigid cylindrical dowels as model vegetation. Experimental observations were consistent with the theory. Under high stem drag or low stem Reynolds number conditions, the interface deviated from the well-documented block profile associated with unobstructed lock-exchange flows and approached a linear profile. Criteria are developed to categorize all flow conditions as inertial or non-inertial and the interface profile as linear, transitional, or non-linear, respectively, based on (a) the evolution of the velocity of the leading edge of the undercurrent and (b) the interface shape. Finally, the present model is enhanced to account for wind forcing and bed friction to better describe conditions found in nature. The theory highlights the sensitivity of currents to wind forcing.

Thesis Supervisor: Heidi M. Nepf
Title: Associate Professor of Civil and Environmental Engineering

Acknowledgments

I gratefully acknowledge the MIT Presidential Graduate Fellowship for supporting my graduate studies during the academic year 2003-2004. The material in this thesis is based upon work supported by the National Science Foundation under Grant No. EAR - 0309188. Any opinions, findings, and conclusions or recommendations expressed in this material are those of the author(s) and do not necessarily reflect the views of the National Science Foundation.

I am grateful to my supervisor, Professor Heidi M. Nepf, for her continued guidance, support, and enthusiasm. Current and past members of my research group have also assisted me on many issues, and I thank Marco Ghisalberti, Anne Lightbody, Molly Palmer, and Brian White for their insightful comments. In particular, I am indebted to Brian for assisting me with the setup of various equipment, for answering my endless technical questions, and for the numerous helpful discussions that took place over the past two years.

In addition, I would like to acknowledge two individuals, Laura Rubiano-Gomez and Paula Kulis, whose experimental data are incorporated into this thesis. Laura conducted experimental runs presented in this thesis between October - December 2003 as an undergraduate research assistant in the Nepf group. Paula shared with me data and experimental observations from her undergraduate thesis, which had initiated the research presented here.

The MATLAB® codes that were used to capture the interface position from images were developed by Blake Landry, a former graduate student in the Civil and Environmental Engineering Department. I thank Blake for sharing the codes with me and for his valuable assistance and insights regarding CCD imaging and image processing.

On a personal note, I would like to thank my family and friends for their moral support. Thanks for being who you are.

Contents

List of Figures

List of Tables

Chapter 1

Introduction

Wetlands, both coastal and freshwater, are important transition zones between land and water. By providing physical obstructions to flow, wetlands buffer storm waters and mitigate floods. From an ecological standpoint, wetlands provide a critical habitat for many birds and fish. In addition, wetlands control the transport of many dissolved and sorbed substances between land and water. Wetlands transform or remove from the water certain metals such as arsenic and nutrients such as nitrogen and sulfates, thereby improving the quality of the water as it flows through the system. For example, a wetland plant species has been observed to create conditions that enhance the removal of arsenic [Keon, 2002]. In fact, artificial wetlands are currently employed as economically feasible and environmentally benign treatment methods for industrial, agricultural, and domestic wastewater. However, wetlands may also release toxic substances into the environment. For example, wetlands have been observed to produce methyl mercury [St. Louis *et al.*, 1994]. In fact, a positive correlation was observed between monomethylmercury yield and the fractional surface area of a watershed attributed to wetlands [Hurley *et al.*, 1995]. With an estimated $4-6\%$ of Earth's total land area covered by wetlands [Mitsch & Gosselink, 2000], the ubiquity of these vegetated aquatic canopies exemplifies the importance of enhancing our understanding of transport processes in these systems.

While many biological and chemical processes take place in wetlands, hydrodynamic parameters such as the residence time influence how long substances remain in the wetland system and the physiochemical conditions these substances encounter during that period *e.g.*, by dictating nutrient loads. Thus, an understanding of the hydrodynamics of vegetated flow is critical

in accurately predicting the biological, chemical, and physical interactions between constituents in the water and the environment.

This study investigates one type of physical process commonly referred to as exchange flows or gravity / density currents. The term "exchange flows" broadly refers to currents driven by horizontal density gradients. These currents are not restricted to wetlands; in fact, they occur in many natural and artificial systems, both atmospheric and aquatic. For example, cold air outflows that are associated with thunderstorms result from density differences in air temperature below a thunderstorm cell. Another atmospheric example is the sea breeze generated by temperature gradients due to differential warming and cooling between the land and sea [Simpson, 1997]. Aquatic examples include exchange flows in estuaries that form where salt water flows inland and freshwater flows towards the sea [O'Donnell, 1993]. Many studies have also examined convective currents – exchange flows driven by temperature differences – in sidearms or littoral zones of reservoirs in the field [*e.g.*, Adams & Wells, 1984], in the laboratory [*e.g.*, Lei & Patterson, 2002; Sturman & Ivey, 1998], and through modelling [*e.g.*, Brocard & Harleman, 1980; Farrow & Patterson, 1993; Horsch *et al.*, 1994].

In inland aquatic systems density gradients commonly arise from differential heating and cooling, which may be caused by spatial variability in water depth [*e.g.*, Monismith *et al.*, 1990; Roget & Colomer, 1996], groundwater discharge [Roget *et al.*, 1993], light compensation depth [*e.g.*, MacIntyre *et al.*, 2002; Nepf & Oldham, 1997], shading due to floating macrophytes [Coates & Ferris, 1994], or sheltering from the wind [MacIntyre *et al.*, 2002]. The presence of vegetation in an aquatic system may affect both the generation and behavior of exchange flows. Because it can only be established in shallower regions of a water body, aquatic vegetation enhances the spatial variability in an aquatic system. For example, water in the littoral zones of lakes may warm and cool at a different rate than the pelagic zone not only because the water is shallow, but also because of shading or inhibited evaporation due to sheltering by the macrophytes. These effects may thus enhance or inhibit the temperature – and hence density – gradient between different zones in the system. Also, vegetation may suppress an exchange flow by exerting drag on the flow and dissipating its kinetic energy. In turn, exchange flows may have a feedback effect on the vegetation by enhancing the transport of dissolved and suspended nutrients and contaminants between different areas of the aquatic system, thereby

creating conditions that either promote or inhibit vegetation growth [Kalff, 2002; Stefan *et al.*, 1989]. Observations by Oldham & Sturman (2001) demonstrate the significance of these effects. The authors report a quadrupling of the residence time of the vegetated region in a wetland mesocosm due to dense emergent vegetation suppressing the flow rate of convective currents [Oldham & Sturman, 2001].

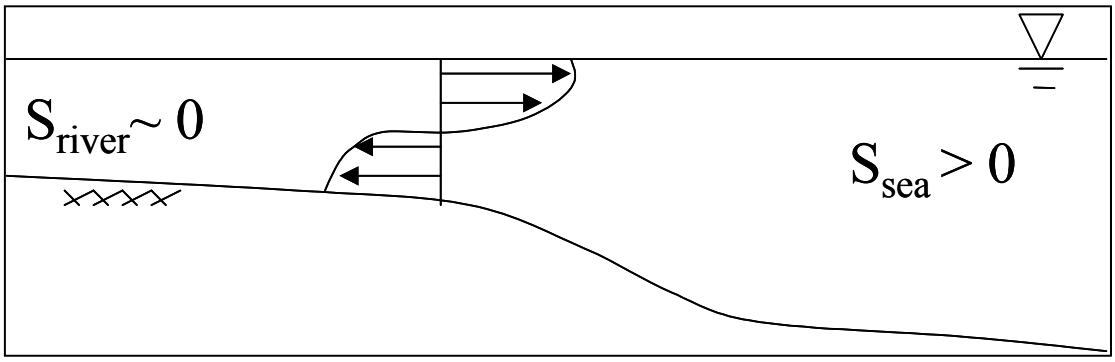

Figure 1-1: Schematic of gravity currents in an estuary. S denotes salinity.

This thesis specifically investigates exchange flows through rigid emergent vegetation, such as is found in wetlands and salt marshes. In the laboratory, the density gradient was established through differences in salinity instead of temperature. Such gradients are commonly found at freshwater - salt water interfaces in tidal estuaries. Lock-exchange flows are one result of such gradients. A salinity gradient that develops between the sea water and freshwater on opposite sides of a closed lock gate drives such flows. When the gate is opened, the heavier sea water collapses and flows along the bottom into the freshwater. The freshwater compensates for this movement by flowing in the opposite direction along the surface [Simpson, 1997]. In this study, wooden dowels, selected to model rigid plants because of their morphology, were introduced into this flow. The dowels were a source of drag, and contributed to the dissipation of energy in the system. Previous work has shown that the presence of dowels significantly alters the shape of the interface between the two fluids [Deardon, 2003]. In this thesis, a method of classification of the interface profile based on measurable parameters will be developed to explain Deardon (2003)'s observations. Then, a mathematical model of the front will be developed for the high vegetation drag regime. Subsequently, predicted front velocities will be compared to

experimental observations over a range of density differences and vegetation densities. The observations will be recorded with a Charge Coupled Devices (CCD) camera and processed using the software MATLAB®.

The remainder of this chapter introduces previous studies conducted on exchange flows. In Chapter 2, mathematical descriptions of the exchange flow velocity are developed from the conservation of energy and momentum. Chapter 3 describes the setup and procedure of the laboratory experiments. Chapter 4 presents the results of these experiments and the analyses of these results. First, Deardon (2003)'s observations are compared with theoretical predictions to validate the mathematical models. Then, quantitative measures are developed to categorize exchange flows as inertial or non-inertial and as having a nonlinear, transitional, or linear interface profile. Finally, a stem drag constant C' is estimated from the experimental data. In Chapter 5, the model is enhanced to examine the effects of wind forcing. Chapter 6 summarizes the main findings of this study and identifies several aspects of the study that merit further research.

1.1 Literature Review

1.1.1 Exchange flows in freshwater systems – convective currents

Convective currents have been studied extensively through both field measurements and numerical modeling because of their importance as a large-scale transport mechanism in many lentic systems. Because convective currents are induced by spatial variability, they tend to span large distances, and may significantly enhance basin-scale mass transport.

A number of field studies have reported the impact convective currents have on the residence time of lentic systems. This hydraulic parameter is a measure of the period that a volume of water is exposed to the physical, chemical, and biological processes taking place in the system, and thus dictates to some extent the magnitude of nutrient fluxes and productivity associated with the system [Kalff, 2002]. For example, Roget *et al.* (1993) established from temperature measurements that convective currents induced by differential cooling in a $1.11\,\mathrm{km}^2$, 42 m-deep lake was the dominant mode of water exchange between the two constituent lobes. The convective current consisted of an undercurrent from the shallower and cooler lobe to the

deeper lobe, whose speed fluctuated between $0.015\,\mathrm{m\,s^{-1}}$ and $0.08\,\mathrm{m\,s^{-1}}$ over a 27-day period [Roget *et al.*, 1993]. The authors determined that the flow rate of the exchange current was more than an order of magnitude greater than the estimated total inflow into the lake, and that the current reduced the residence time of the shallow lobe to 0.9% of what would be expected in the absence of such currents [Roget *et al.*, 1993]. Similarly, Monismith *et al.* (1990) estimated the residence time in a reservoir sidearm to be 0.05% of the timescale for horizontal diffusion based on observed flow velocities in the epilimnion, which were on the order of $0.02\,\mathrm{m\,s^{-1}}$.

Furthermore, field studies suggest that these convective currents recur frequently. Based on temperature profiles taken at various distances from the shore in a 6 m-deep embayment in a $275\,\mathrm{km^2}$ reservoir, James *et al.* (1994) found that conditions to induce convective currents by differential heating were satisfied on 74% of the days over one month during which the measurements were taken.

Residence times have also been predicted through modeling. A number of models based on heat budgets have been developed [*e.g.*, Stefan *et al.*, 1989; Sturman *et al.*, 1999], to which field data may be applied to predict the convective flow rate. For example, Stefan *et al.* (1989) estimated a residence time of $2 - 5\,\mathrm{h}$ in a 60 m-long and 1.32 m-deep sloping littoral zone. Residence times of similar magnitudes were predicted by laboratory studies and numerical simulations as well. Sturman *et al.* (1996) examined convective currents induced in a long, rectangular flume with a cooling region at the top of one end of the tank and a warming region at the bottom of the opposite end. The authors used scaling arguments to predict that, under typical conditions found in a reservoir sidearm, the resulting steady-state convective current velocity and the timescale for the entire system to reach steady state (defined as the filling time) would be on the order of $0.04\,\mathrm{m\,s^{-1}}$ and $6\,\mathrm{h}$, respectively. Similarly, Horsch & Stefan (1988)'s model for surface cooling, which is summarized below, predicted a maximum flow rate of $2\,\mathrm{l\,s^{-1}}$ and a residence time on the order of $6\,\mathrm{h}$ for the littoral region of a 20 m long and 4 m deep triangular domain. These predictions, together with field observations discussed above, emphasize the importance of convective currents in promoting exchange between littoral and pelagic zones.

It is necessary to mention here, as a caveat, that many of the field measurements in literature that were obtained in the context of convective currents research were taken over a period of a

few days in a single lake. Consequently, the results cannot be generalized beyond anticipating that similar temperature variations may occur in lakes of similar morphology that are situated in a similar climate. Nonetheless, the studies mentioned here demonstrate that convective currents are a significant transport mechanism in some natural systems.

1.1.2 Unsteady gravity currents

Previous studies have predominantly treated convective currents as steady flows. However, under conditions found in nature, convective currents may display transient behavior. Wells & Sherman (2001), for example, estimated the timescale of convective circulation formation to be 16 h and 25 h in consecutive years in a sidearm whose length was 1500 m and 3000 m at the respective times. Similarly, Sturman *et al.* (1999)'s model yielded a residence time on the order of 21 h for the 3 m-deep littoral region of a 0.684 km^2 lake. These values are of the same order as the timescale of the diurnal forcing (= 12 h) and suggest that the forcing was not maintained long enough for the convective currents to become steady. Also, Farrow & Patterson (1993) examined the response time of convective currents to diurnal forcing in a triangular cavity and found that the flow response may lag diurnal forcing by as much as 12 h in a sidearm of a reservoir. Such delays were also observed in the field, which were partly attributed to the fact that the water was in motion prior to the reversal of the forcing [Monismith *et al.*, 1990]. Furthermore, Wells & Sherman (2001) postulated, based on the dependence of the timescale of flow formation on the length of the sidearm, that steady flow may be established only in reservoirs less than $2 - 3$ km long. These estimates of flow development timescales strongly suggest that diurnally forced convective currents are rarely steady in nature. Moreover, the exchange flows recreated in the laboratory in the present study were unsteady, as lock-exchange flows are in general. As such, unsteady convective currents are relevant in understanding both the lock-exchange flows in the present study and convective currents in general.

Observing that the timescale of flow development in nature is often of a similar magnitude to the period of diurnal forcing [*e.g.*, Farrow & Patterson, 1993; Sturman *et al.*, 1996; Wells & Sherman, 2001], a number of numerical and experimental studies have recently examined the transient behavior of exchange flows as they developed from an isothermal and stationary state into a basin-scale circulation.

One of the earlier works on unsteady convective currents was by Patterson & Imberger (1980), in which the transient behavior of initially stationary and isothermal fluid in a rectangular domain was modeled. The authors categorized transient flow behavior according to the magnitude of the Rayleigh number $\left(Ra = \frac{g\alpha(T_2-T_1)\Delta l^3}{\nu\kappa}\right)$ relative to the Prandtl number $\left(Pr = \frac{\nu}{\kappa}\right)$ and the aspect ratio of the tank, where g is the gravitational acceleration, α is the coefficient of expansion, ν is the kinematic viscosity, κ is the thermal diffusivity, and T_1 and T_2 are temperatures separated by distance Δl [Tritton, 1988]. Three categories defined the mode of heat transfer associated with the flow: conductive, convective, and transitional, where both conductive and convective mechanisms are significant. The authors found that flows approached steady state differently depending on their classification; flows in the conductive regime approached monotonically, whereas those in the convective regime oscillated. Accordingly, the timescale for the approach to steady state differed between the categories as well [Patterson & Imberger, 1980].

Horsch *et al.* (1994) also identified three Ra-dependent regimes of flow development in a similar numerical study. Unlike Patterson & Imberger (1980)'s work, however, the domain in Horsch *et al.* (1994)'s simulations was triangular instead of rectangular, and convective currents were induced by surface cooling instead of differential heating of the end walls. Despite the differences in the shape of the domain and the nature of the forcing, the approach to steady state was similar to that observed by Patterson & Imberger (1980). Steady state was achieved in low and intermediate Ra regimes, which consisted of a main cell that spanned the entire domain [Horsch *et al.*, 1994]. Similar to transient behavior in the convective regime in Patterson & Imberger (1980)'s study, the approach to steady state velocities was oscillatory in the intermediate Ra regime. In contrast, in the high Ra regime, only a time-averaged steady state was achieved [Horsch *et al.*, 1994].

Horsch & Stefan (1988) also developed a numerical model for the same configuration (*i.e.*, continuously-cooled top boundary in a triangular domain) to describe the flow development from the onset of surface cooling. The authors identified three phases in the flow development. Following the onset of surface cooling, a horizontal temperature gradient developed locally at the shallow end of the domain because the sloping bottom hindered the downward growth of the surface boundary layer. Next, thermals sank from the surface boundary layer, mixing

the cooler surface water with the deeper water. In the final phase of flow development, the horizontal temperature gradient generated an undercurrent down the slope and a surface current in the opposite direction. Similar to steady flow conditions observed by Patterson & Imberger (1980) and Horsch *et al.* (1994), these currents created a single-cell circulation that spanned the domain [Horsch & Stefan, 1988]. However, because of the continuous surface cooling, thermals continued to form periodically, and were entrained by the undercurrent propagating down the slope. The quasi-steady state that results was characterized by the periodic development of thermals and the circulation [Horsch & Stefan, 1988].

Experimental work by Lei & Patterson (2002) identified three stages in the response of a triangular cavity to solar radiation. Initially, a thermal boundary layer developed at the top and the bottom of the system. The presence of the bottom layer, which arose because the incoming radiation that was absorbed into the bottom was subsequently re-emitted, resulted in water at the bottom of the tank being warmer than the water in the middle. Lei & Patterson (2002) subsequently observed the development of rising thermals as a physical manifestation of the instability in such temperature distributions. In this second stage of flow development, a return flow also developed along the surface towards the deeper end of the cavity to compensate for the rising thermals flowing up the sloping bottom. The up-slope flow transferred warmer water at the bottom to the surface. Eventually, a quasi-steady state was achieved in which temperature increased at a steady rate in response to the constant radiation [Lei & Patterson, 2002]. Also, the thermals were markedly smaller. The same stages of transient response were identified in subsequent numerical simulations [Lei & Patterson, 2003].

Coates & Patterson (1993) conducted a laboratory study with differential heating in a rectangular cavity. In this study, differential heating was achieved through exposing only one part of the surface to uniform surface radiation while the rest of the surface received no radiation. Through scaling arguments, the authors identified five different timescales, and observed that flow development depended on the relative magnitudes of the timescales [Coates & Patterson, 1993]. These timescales characterize when (i) the isotropic lengthscale of thermal diffusion exceeds the vertical radiation attenuation lengthscale; (ii) the (horizontal) advective lengthscale exceeds the diffusive lengthscale; (iii) the viscous lengthscale exceeds the radiation attenuation lengthscale; (iv) the advective lengthscale exceeds the horizontal length of

the region exposed to surface radiation; and (v) the diffusion lengthscale exceeds the horizontal length of the region sheltered from surface radiation [Coates & Patterson, 1993].

Sturman & Ivey (1998) examined the effects of temporal variability of the forcing in a rectangular laboratory flume by switching the forcing from destabilizing to stabilizing after some period of time. Steady conditions under stabilizing forcing is characterized by the balance between conduction and convection [Sturman & Ivey, 1998]. Because the former is a diffusive process, the discharge generated by stabilizing forcing is expected to be smaller than that induced by destabilizing forcing. Indeed, the authors observed that the discharge induced by cooling, which scaled as $Q \sim (Bl)^{1/3} H$, was greater than that by warming, which scaled as $Q \sim (Bl)^{1/3} \delta$, where Q is the steady-state discharge, B is the buoyancy flux, l is the forcing region length, H is the depth at the forcing plate, and δ is the thermal boundary layer thickness. The boundary layer thickness is not expected to exceed the water depth, and $H > \delta$ in a given system [Sturman & Ivey, 1998].

1.1.3 Effects of obstructions on gravity currents

Gravity currents are forced to flow through obstructions in many contexts. While the focus of this thesis is restricted to the effects of aquatic vegetation, gravity currents encounter vegetation in both aquatic and atmospheric systems. Artificial structures such as buildings and solid boundaries such as walls or artificial structures for pollutant containment also interfere with or even halt the propagation of gravity currents.

Studies of gravity currents through a cluster of obstacles offer insight into possible effects aquatic vegetation may have on unsteady flows such as lock-exchange flows. For example, Davies & Singh (1985) investigated the effect of porous screens on otherwise unobstructed unsteady dense gas currents, where the screens represented localized obstacles such as a finite number of rows of trees or buildings. As anticipated, with an introduction of any source of energy dissipation, the longitudinal velocity of the gravity current decreased, with the reduction in velocity increasing with the density of the obstacles (the number of screens, in this case). Also, an increase in the vertical thickness of the current was observed [Davies & Singh, 1985]. Parallel to Davies & Singh (1985)'s report, Rottman *et al.* (1985) developed a mathematical model to predict the effect of a porous screen on the shape of steady gravity currents and then

qualitatively predicted the transient behavior of the gravity currents as they passed through the screens. The authors described the slope of the interface between the heavy gas and the ambient air for steady flows as:

$$\frac{dz}{dx} = -\frac{\mathrm{C}_D F^2}{1 - F^2} \tag{1.1}$$

where z is the elevation of the interface above the impermeable horizontal bed, x is the direction of propagation of the gas, $F^2 = \frac{(uz)^2}{g' z^3}$, $g' = g\left(\frac{\rho_1 - \rho_2}{\rho_2}\right)$, ρ_1 and ρ_2 are the densities of the heavy and light fluid, respectively, and C_D is the drag coefficient. Equation 1.1 demonstrates the C_D-dependence of the interface slope, and predicts that the slope of the interface will be steeper when it travels through a region of high drag. Conversely, the slope vanishes as C_D approaches zero. In addition, Rottman *et al.* (1985) predicted that, when the gravity current front reached the porous screen, a weak hydraulic jump would propagate upstream and the depth of the heavy current would increase. These predictions were confirmed by qualitative observations during laboratory studies of lock-exchange flows [Rottman *et al.*, 1985].

A few studies have examined specifically the hydrodynamic effects of vegetation. One approach was to incorporate vegetative drag retroactively in a mathematical model of unobstructed exchange flows. Horsch & Stefan (1988) first developed a model for a non-vegetated system, in which viscous drag contribution came from the shear stress at the bed and at the interface of the undercurrent and the return flow. The undercurrent was subject to both shear stresses, whereas the return current at the surface was only subject to the shear stress at the interface. Horsch & Stefan (1988) then incorporated vegetation into their numerical model by adding vegetative drag linearly to the mathematical expression for viscous drag in the undercurrent and return flow. Vegetative drag was defined as $\frac{1}{2} C_D \rho \overline{u_i}^2 d h_i$, where d is the stem diameter, ρ is the density, C_D is the stem drag coefficient, and h_i and $\overline{u_i}$ are the depth and the local mean velocity of the undercurrent and return flow, respectively. The stem drag was estimated as $\mathrm{C}_D = \frac{10.0}{\sqrt{\mathrm{Re}}}$ for $0.4 \leqslant \mathrm{Re} \leqslant 40$, where Re is the stem Reynolds number. To include the effect of vegetative drag retroactively, Horsch & Stefan (1988) replaced the kinematic viscosity with a new parameter ε, the "apparent viscosity," in the numerical model. The linear sum of the viscous drag and the vegetative drag was equated with the viscous drag expression with ε instead of ν, the kinematic viscosity. Solving this expression for ε yielded

[Horsch & Stefan, 1988]:

$$\varepsilon_L = \nu + \frac{C_D \overline{u_L} d}{2\,(1+\lambda)\,G} \left(\frac{h_L}{s}\right)^2 \tag{1.2}$$

and

$$\varepsilon_U = \nu + \frac{C_D \overline{u_U} d}{2\lambda G} \sqrt{\frac{h_L}{h_U}} \left(\frac{h_L}{s}\right)^2 \tag{1.3}$$

for the undercurrent and return flow, respectively, where λ is the ratio of the shear stress at the interface and at the bed ($z = 0$), G is a constant of proportionality $G = \frac{h_L}{\overline{u_L}} \frac{\partial u}{\partial z}|_{z=0}$, and s is the plant spacing. The subscripts L and U refer to the undercurrent (lower layer) and return flow (upper layer), respectively. An average of ε_U and ε_L replaced ν in the numerical simulations.

Another approach was to model vegetation as porous media [Oldham & Sturman, 2001]. Their scaling analysis assumed steady conditions; as discussed earlier in this chapter, this assumption deviates from lock-exchange flows, which are inherently unsteady. Nevertheless, the model represents one method of incorporating vegetative drag into a mathematical description of the convective flow rate [Oldham & Sturman, 2001]:

$$Q \sim \left[B \frac{\sqrt{k_x}}{c} \left(\frac{k_x}{k_z}\right)^{1/3} \right]^{1/3} l \tan\theta \tag{1.4}$$

where B is the buoyancy flux, c is the Forchheimer coefficient, k_x and k_z are the longitudinal and vertical permeabilities of the vegetated region, respectively, l is the length of the forcing region, and θ is the slope of the vegetated region. Since $\frac{c}{\sqrt{k_x}} \left(\frac{k_z}{k_x}\right)^{1/3}$ corresponds to the drag exerted by the vegetation, the model correctly predicts that an increase in drag results in a decrease in the discharge [Oldham & Sturman, 2001].

Oldham & Sturman (2001) then compared model predictions with laboratory and mesocosm observations in model wetlands with a solid volume fraction of 17% and 16%, respectively. Note that the flushing timescale for the vegetated region in the mesocosm was approximately 4h, which was a third of that for diurnal forcing. The difference in magnitude of the timescales was consistent with the steady state assumption of the model. However, the velocity profiles were taken between 4AM and 10AM in April in Perth, Western Australia, and it is possible that the measurements coincided with the diurnal reversal of the forcing (*i.e.*, from cooling to heating), and the exchange flows present at the time of recording may have been unsteady.

Nonetheless, the model accurately predicted the convective current flow rates.

Most recently, Deardon (2003) investigated the speed of a lock-exchange flow as it propagated through a random array of rigid dowels. A mathematical solution was developed for toe velocity by applying a rectangular lock-exchange flow approximation to an energy balance analysis (see top figure in Figure 2-1). Most relevant to the present thesis, however, is the observation of a linear interface under low density gradient-high stem density conditions ($\rho_1 - \rho_2 \leqslant 0.01\,\mathrm{kg\,l^{-3}}$ and $a \geqslant 0.0855\,\mathrm{cm^{-1}}$, where a is the frontal area per unit volume) [Deardon, 2003]. Moreover, Deardon (2003) reported that the disagreement between theoretical predictions and observed velocities increased as the stem density increased, suggesting the need for modifications to the model when describing exchange flows in the linear interface regime. To our knowledge, the impact of aquatic vegetation on the shape of exchange flows has not been studied extensively. One of the goals of this study is to develop a mathematical model to analyze exchange flows with such morphology.

To our knowledge, linear interfaces have not been reported in lock-exchange flows before. However, such interfaces have been observed in the context of seawater intrusion into ambient freshwater in coastal aquifers. As stated above, flows through porous media are analogous to surface water flows through obstacles such as vegetation; the former has significantly higher drag dissipation than the latter because the solid volume fractions in sand are much higher than those associated with aquatic canopies. Indeed, Keulegan (1954) investigated the seawater-freshwater interfaces in aquifers by examining lock-exchange flows in a partitioned laboratory flume filled with sand. Dagan & Zeitoun (1998) later advanced Keulegan (1954)'s solution to account for spatial heterogeneities.

The exchange flow in Keulegan (1954)'s experiments shared the same features as the high stem density-low density difference lock-exchange flows in Deardon, 2003 and the present study. First, Keulegan (1954) consistently observed a linear interface at all times and under all flow conditions. The mean porosities in Keulegan, 1954 were 0.432 and 0.459, which are equivalent to, in terms of equal porosity, stem densities approximately 8 times greater than the highest stem density scenarios examined in Deardon, 2003. Keulegan (1954) also reports that the linear interface rotated about a point on the interface at mid-depth and that the upper half of the interface moved at the same speed as the bottom half of the interface, but in the opposite

direction. That is, the interface was consistently symmetric about its middle, but in the opposite direction. These two characteristics are assumed in the mathematical models developed in the present study. Because of the flow visualization and imaging method used in the present study, the position of the upper half of the interface is difficult to determine, and no effort was made to quantitatively test these assumptions. While we observed qualitatively that the rotation of the interface is about the mid-point, we could not resolve the vertical symmetry.

Chapter 2

Extension of Theory to Vegetated Exchange Flows

Deardon (2003)'s observations suggest that the interface can have a range of behavior depending on flow and canopy conditions. Three regimes of front propagation can be identified from previous studies of lock-exchange flows: (a) the traditional inertia-dominated regime characterized by a horizontal interface in the middle and a constant front velocity; (b) an intermediate regime where velocity decreases due to drag and the interface is no longer perfectly horizontal; and (c) a drag-dominated regime marked by a linear interface and decreasing velocity. Exchange flows in the first scenario have traditionally been treated as "blocks," where the longitudinal cross-section is treated as rectangular (top image in Figure 2-1). In contrast, exchange flows in the third scenario have a triangular cross-section (bottom image in Figure 2-1). One would anticipate actual flows to fall within the continuum of possible interface shapes between the two extremes.

2.1 Energy Balance

In modeling exchange flows in the linear interface regime, it is clearly more appropriate to assume a linear velocity profile than the traditional block flow profile, which assumes a constant velocity in each layer. A modified energy balance with a linear velocity profile assumption is presented below as an alternative to Deardon (2003)'s model of flows propagating through a

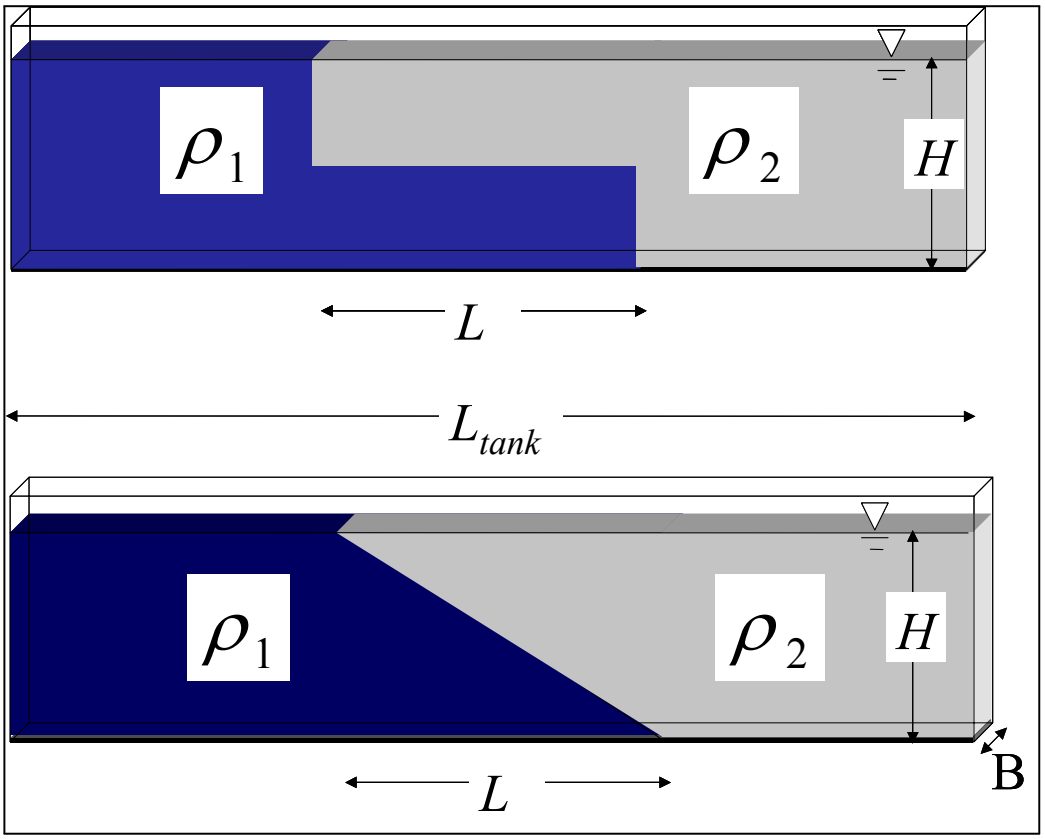

Figure 2-1: Three-dimensional sketch of the tank and the definition of the key parameters included in the mathematical models. H is water depth; L is the longitudinal length of the interface; B and L_{tank} are the width and length of the tank, respectively; and ρ_1 and ρ_2 are the density of the two fluids. Top and bottom figures are associated with the block flow and linear velocity profile assumptions, respectively. Not to scale.

canopy with a block interface profile.

The Cartesian coordinate system is defined with its origin ($x = z = 0$) at the bottom of the tank. The x-axis is aligned with the direction of propagation of the undercurrent and the z-axis is in the vertical direction normal to the bottom of the tank, where $z = H$ is the free surface.

At time t, the potential energy in the system is the linear sum of the potential energy in each fluid:

$$PE\left(t\right) = g\frac{1}{6}LH^2B\left(\rho_1 + 2\rho_2\right) + g\frac{\left(L_{tank} - L\right)H^2B}{4}\left(\rho_1 + \rho_2\right) \tag{2.1}$$

where L_{tank} and B are the total length and width of the tank, respectively, H is the water

depth, $\rho_1\,(>\rho_2)$ and ρ_2 are the densities of the two fluids, and $L(t)$ is the longitudinal length of the interface between the two fluids (Figure 2-1). The time dependence of $PE(t)$ comes entirely from $L(t)$.

The total kinetic energy at time t is:

$$KE\,(t) = \int_0^H \frac{1}{2}\rho B L u^2 dz \tag{2.2}$$

In this thesis, the flow is assumed to be purely horizontal. Accordingly, the velocity, u, is treated as a horizontal scalar term. Although vertical speeds may be induced by the formation of billows along the interface [Lowe *et al.*, 2002], this is not a concern in the present study, as the presence of vegetation has been observed to suppress any observable non-uniformities along the interface [Deardon, 2003]. In the absence of turbulence along the interface, the horizontal flow assumption is appropriate everywhere in the tank, except near the toe of the exchange flow where the interface slope is the sharpest and fluid moving along the interface has the greatest vertical velocity component [*e.g.*, Figure 6, Kneller *et al.*, 1999; Lowe *et al.*, 2002; Figure 7, Middleton, 1966]. Note that the assumption that the vertical component of the velocity is small is more appropriate for runs where the interface is approximately linear, and is the least appropriate when the run has a block interface profile. Preliminary observation indicates that fluid in front of the leading edge of the undercurrent is stationary. Then, by conservation of mass, there must be vertical movement of water at the toe. In an ideal block flow, the vertical velocity must equal longitudinal velocity immediately in front of the toes. In contrast, in a predominantly linear interface, the displaced fluid flows along the interface at an angle. Then, assuming that ambient fluid flows upward along the interface as the undercurrent propagates into it, the vertical component of the velocity immediately in front of the undercurrent may be described as $v = u \sin\theta$ where the angle between the interface and the bed is θ.

A linear velocity profile assumption yields:

$$u\,(z) = 2u_{toe}\left(\frac{1}{2} - \frac{z}{H}\right) \tag{2.3}$$

Applying the Boussinesq assumption $\left(\text{the maximum } \frac{(\rho_1-\rho_2)}{\bar{\rho}} \text{ is } 0.05\right)$and Equation 2.3 to Equa-

tion 2.2, the total kinetic energy can be expressed as:

$$KE\,(t) = \frac{\overline{\rho} LHBu_{toe}^2}{6} \tag{2.4}$$

where $\overline{\rho}$ is the mean density of the two fluids. The total energy in the system at any given time is the sum of the kinetic and potential energy of the system:

$$E(t) = \frac{\overline{\rho} LHBu_{toe}^2}{6} + g\frac{LH^2B}{6}\left(\rho_1 + 2\rho_2\right) + g\frac{\left(L_{tank} - L\right)H^2B}{4}\left(\rho_1 + \rho_2\right) \tag{2.5}$$

The rate of change in the total energy of the system can be evaluated from Equation 2.5:

$$\frac{\partial E(t)}{\partial t} = \frac{\overline{\rho} HB}{6}\frac{\partial\left(Lu_{toe}^2\right)}{\partial t} - \frac{BH^2g\left(\rho_1 - \rho_2\right)}{12}\frac{\partial L}{\partial t} \tag{2.6}$$

The only time-dependent variables are L and u_{toe}. Equation 2.6 can be simplified by substituting $\frac{\partial L}{\partial t} = 2u_{toe}$:

$$\frac{\partial E(t)}{\partial t} = \frac{\overline{\rho} HB}{3}u_{toe}\left[L\frac{\partial u_{toe}}{\partial t} + u_{toe}^2\right] - \frac{BH^2g\left(\rho_1 - \rho_2\right)}{6}u_{toe} \tag{2.7}$$

Assuming quasi-steady conditions, $\frac{\partial u_{toe}}{\partial t} \ll \frac{u_{toe}^2}{L}$, the above equation simplifies to:

$$\frac{\partial E(t)}{\partial t} = \frac{\overline{\rho} BH}{3}u_{toe}^3 - g\frac{BH^2\left(\rho_1 - \rho_2\right)}{6}u_{toe} \tag{2.8}$$

The validity of this assumption of quasi-steady conditions is explored in Appendix B with experimental observations.

The time rate of change of the total energy in the system must equal energy dissipation. Assuming that energy dissipation only arises from drag on the stems,

$$\frac{\partial E(t)}{\partial t} = -Du \tag{2.9}$$

where $D = \frac{1}{2}C_D\rho u^2 aHBL$ is the total drag force required to move $\frac{a}{d}BL$ stems through a viscous fluid with velocity u, a is the frontal area per unit volume, and d is the stem diameter. Let us

assume that C_D and a are independent of z. Then:

$$Du = \frac{1}{2} C_D \rho a B L \int_0^H u^3 dz \tag{2.10}$$

The linear velocity profile assumption (Equation 2.3) describes the depth-dependence of u. Substituting Equation 2.3 into Equation 2.10 and integrating over the depth yields:

$$Du = \frac{1}{8} C_D \rho a B L u_{toe}^3 H \tag{2.11}$$

Substituting Equations 2.8 and 2.11 into Equation 2.9 yields:

$$u_{toe}^2 + \frac{3 C_D a L}{8} u_{toe}^2 - g \frac{(\rho_1 - \rho_2)}{\rho} \frac{H}{2} = 0 \tag{2.12}$$

This quadratic equation can be solved for velocity:

$$u_{toe} = \pm 2 \sqrt{\frac{gH}{8 + 3 C_D a L} \frac{(\rho_1 - \rho_2)}{\rho}} \tag{2.13}$$

The energy balance derivation for the block flow regime is identical to this derivation except for the difference in the z-dependence of the velocity. Readers are referred to the derivation presented in Deardon, 2003. The equivalent solution for toe velocity under the block flow assumption is:

$$u_{toe} = \pm \sqrt{\frac{gH}{4 + 2 C_D a L} \frac{(\rho_1 - \rho_2)}{\rho}} \tag{2.14}$$

2.2 Momentum Balance

Because the energy balance assumes an interface shape, it cannot be used to predict the interface shape, but only the velocity at $z = 0$. The interface can be modeled through conservation of momentum, which does not make any *a priori* assumptions about the interface shape.

The Navier-Stokes equation in the longitudinal direction can be written as:

$$\frac{du}{dt}\hat{i} = \frac{\partial u}{\partial t} + u\frac{\partial u}{\partial x} + v\frac{\partial u}{\partial y} + w\frac{\partial u}{\partial z} = -\frac{1}{\rho}\frac{\partial P}{\partial x} - \frac{C_D a u^2}{2} + \nu \frac{\partial^2 u}{\partial z^2} \tag{2.15}$$

where P is the pressure, ν is the kinematic viscosity, and v and w are lateral and vertical components of the fluid velocity. Several assumptions can be made that justify the omission of some of the terms in Equation 2.15. First, viscous and turbulent stresses can be neglected because their magnitudes are insignificant relative to the drag term for flow conditions examined in this study. (An order-of-magnitude comparison of the viscous stress term and the drag term is presented in Appendix A.) Second, the $\frac{\partial}{\partial y}$ term can be omitted when the longitudinal length scale is significantly greater than the lateral scale, *i.e.*, $L > B$. Additionally, because the forcing mechanism is uniform in y, the resulting flow is expected to be uniform in y as well. Third, w can be assumed to be negligible relative to $u\,(t)$ based on a dimensional analysis. The continuity equation for two-dimensional flow can be expressed as: $\frac{\partial u}{\partial x} + \frac{\partial w}{\partial z} = 0$, with $\frac{\partial u}{\partial x}$ scaling as $\frac{\partial u}{\partial x} \sim \frac{u(t)}{L(t)}$. Then, the vertical component of the velocity scales as $w \sim \frac{u(t)}{L(t)} H$. Accordingly, $w \ll u$ if $\frac{H}{L} \ll 1$, *i.e.*, when the horizontal length scale is greater than the vertical scale. Note that, conversely, the assumption of horizontal flow is invalid where $H \gtrsim L$. Fourth, and last, $\frac{\partial u}{\partial t}$ is removed by assuming quasi-steady conditions, as discussed in Section 2.1.

By applying these assumptions, Equation 2.15 can be simplified to:

$$u\frac{\partial u}{\partial x} = -\frac{1}{\rho}\frac{\partial P}{\partial x} - \frac{C_D a u^2}{2} \tag{2.16}$$

The familiar hydrostatic equilibrium assumption is applied to describe the horizontal pressure gradient in terms of the density gradient. This entails the assumption that vertical acceleration is negligible except for gravitational acceleration, which is consistent with the horizontal flow assumption. Where there is a significant vertical velocity component, however, the hydrostatic assumption is inappropriate. Substituting $\frac{\partial P}{\partial z} = -\rho g$ into Equation 2.16 yields:

$$u\frac{\partial u}{\partial x} = -\frac{1}{\rho}\left[\rho g \frac{\partial H}{\partial x} + g\,(H - z)\,\frac{\partial \rho}{\partial x}\right] - \frac{C_D a u^2}{2} \tag{2.17}$$

where $z\,(x,\, t)$ is the distance of the interface from the bottom. The longitudinal density gradient can be scaled as $\frac{\partial \rho}{\partial x}\,(t) \sim \frac{\rho_2 - \rho_1}{L(t)}$. Then,

$$u\frac{\partial u}{\partial x} = -\frac{g}{\rho}\left[\rho \frac{\partial H}{\partial x} - (H - z)\,\frac{(\rho_1 - \rho_2)}{L\,(t)}\right] - \frac{C_D a u^2}{2} \tag{2.18}$$

If the flow is in a closed basin, mass conservation dictates that there be no net flow, *i.e.*, $\int_0^H u\ dz = 0$, which then yields $u = 0$ at $z = \frac{H}{2}$. That is, the interface at $x = 0$ is always at $z = \frac{H}{2}$. Implicit in this derivation is the Boussinesq approximation, which assumes that variations in density are small enough that they only affect buoyancy. Similarly, variations in H are assumed to be insignificant for mass conservation purposes, *i.e.*, no net-flux occurs. This condition can be expressed mathematically as:

$$\rho\frac{\partial H}{\partial x} - \frac{H}{2}\frac{(\rho_1 - \rho_2)}{L(t)} = 0 \tag{2.19}$$

By scaling the inertial term as $u\frac{\partial u}{\partial x} \sim \frac{u^2}{L(t)}$ and applying Equation 2.19, Equation 2.18 can be rewritten as:

$$\frac{u^2}{L(t)} + \frac{C_D a u^2}{2} = g\frac{(\rho_1 - \rho_2)}{\rho L(t)}\left(\frac{H}{2} - z\right) \tag{2.20}$$

The corresponding solution for the interface velocity $u(z,t)$ is:

$$u(z,t) = \pm\sqrt{\frac{2g}{(2 + C_D a L(t))}\frac{(\rho_1 - \rho_2)}{\rho}\left(\frac{H}{2} - z\right)} \tag{2.21}$$

and describes the velocity profile as a function of depth. According to our definition of the Cartesian coordinates, the positive solution corresponds to the undercurrent. In addition, this equation can be evaluated at $z = 0$ to describe the toe velocity:

$$u_{toe}(t) = \sqrt{\frac{gH}{(2 + C_D a L(t))}\frac{(\rho_1 - \rho_2)}{\rho}} \tag{2.22}$$

2.3 Comparison of the Models

The three models can be compared by examining the respective solutions for the toe velocity. Equations 2.13, 2.14, and 2.22 reveal that for any set of conditions, toe velocity predictions based on the energy balance assuming a linear velocity profile are greater than or equal to those based on the momentum balance. These predictions are in turn strictly greater than that by the energy balance assuming a block profile. Thus, the momentum balance predictions, by definition, always fall between the two energy balance predictions. This relationship

between the energy balance predictions arises because a flow with a linear interface must elongate to maintain the same flux, whereas a flow with a block interface may maintain its shape. Consequently, the toe propagation must be faster for a linear interface.

With no drag, both the energy balance solution assuming a linear velocity profile (Equation 2.13) and the momentum balance solution (Equation 2.22) for the toe velocity collapse to:

$$u_{toe}\left(a=0\right)=\pm\sqrt{g\frac{\left(\rho_1-\rho_2\right)}{\rho}\frac{H}{2}} \tag{2.23}$$

On the other hand, the energy balance assuming a block profile becomes:

$$u_{toe}\left(a=0\right)=\pm\sqrt{g\frac{\left(\rho_1-\rho_2\right)}{\rho}\frac{H}{4}} \tag{2.24}$$

The lack of time-dependence is consistent with previous observations of unobstructed lock-exchange flows [Simpson, 1997]. Also, Equation 2.24 agrees with the traditional result for unobstructed lock-exchange flows, where uniform toe velocity is assumed in the two fluids [*e.g.*, Yih, 1980]. This solution agrees well with previous experimental observations. For example, the solution:

$$u_{toe}=0.462\sqrt{g\left(\frac{\rho_1-\rho_2}{\overline{\rho}}\right)H} \tag{2.25}$$

was determined empirically, where $\overline{\rho}$ is the average density of the salt water and freshwater [Keulegan, 1957].

It is less obvious why, in the absence of vegetation ($a = 0$), the momentum balance toe velocity solution agrees with that for the linear velocity profile assumption and not the block flow assumption. This may be explained in terms of differences in the suitability of the hydrostatic assumption made in the momentum balance derivation. As stated above, the hydrostatic assumption implies horizontal flows: since $w = 0$ at the bottom of the tank, if the flow velocity has a vertical component at some point, then there is a finite vertical acceleration. Obviously, lock-exchange flows in a finite tank must involve vertical fluid motion and, as stated earlier, vertical flow is most prominent at the toe where the interface slope is the sharpest. Because of their geometry, however, vertical flow is more significant for block flows than for linear velocity profile flows for a given propagation speed. In idealized block flows, the slope of

the interface is infinite everywhere except at $z = \frac{H}{2}$, where the slope is zero. Therefore, fluid motion at the interface immediately in front of the toe (the lighter fluid near the bottom and heavier fluid near the free surface) is predominantly vertical. In contrast, a linear interface has a constant slope, and the lighter fluid moves at an angle along the interface. As such, the vertical acceleration is smaller than that for the block flow for a given toe velocity. In summary, block flows deviate farther from the hydrostatic assumption. This argument offers a physical explanation as to why the momentum balance solution approaches that for the linear velocity profile energy balance model in the limit of $a = 0$.

Equations 2.13, 2.14, and 2.22 provide means of predicting the toe velocity of an exchange flow given the density difference between the two fluids, water depth, stem density, and drag. While the first three parameters are easily measurable in the environment, little data are available for drag in arrays in the Reynolds number and stem density ranges relevant to the present study. Thus, a method for expressing C_D, which is known to be a function of velocity, is necessary to predict exchange flow behavior. In the following section, the energy and momentum balance derivations presented earlier in this chapter are repeated for the special case where C_D is inversely proportional to the velocity.

2.4 Application of a Linear Drag Law Assumption to the Theoretical Models

If $C_D \propto u^{-1}$ a constant of proportionality can be defined as $C' \equiv C_D u$. Because the velocity-dependence of drag is then linear on a log-log scale, this scenario will be referred to as the "linear drag" regime.

2.4.1 Linear velocity profile energy balance model

Replacing C_D with $\frac{C'}{u}$,the total drag force can be rewritten as:

$$D_{linear} = \frac{1}{2} C' \rho u a H B L \tag{2.26}$$

Then, Equation 2.10 becomes:

$$D_{linear}u = \frac{1}{2}C'\rho aBL2\int_0^{\frac{H}{2}} u^2 dz \tag{2.27}$$

Replacing u with the linear velocity profile assumption (Equation 2.3) to capture the depth-dependence of the velocity, $D_{linear}u$ becomes:

$$D_{linear}u = C'\rho aBL\frac{H}{6}u_F^2 \tag{2.28}$$

Applying Equation 2.28 to Equation 2.9 yields the quadratic equation:

$$u_{toe}^2 + \frac{C'aL}{2}u_{toe} - g\frac{(\rho_1 - \rho_2)}{\rho}\frac{H}{2} = 0 \tag{2.29}$$

which can be solved for u_{toe}:

$$u_{toe} = -\frac{C'aL}{4} + \frac{1}{2}\sqrt{\left(\frac{C'aL}{2}\right)^2 + 2g\frac{(\rho_1 - \rho_2)}{\rho}H} \tag{2.30}$$

2.4.2 Momentum balance

The linear drag law assumption yields the modified momentum balance:

$$\frac{u^2}{L\left(t\right)} + \frac{C'au}{2} - g\frac{(\rho_1 - \rho_2)}{\rho L\left(t\right)}\left(\frac{H}{2} - z\right) = 0 \tag{2.31}$$

The solution for the interface velocity then becomes:

$$u\left(z,\, L\left(t\right)\right) = -\frac{C'aL}{4} + \sqrt{\left(\frac{C'aL}{4}\right)^2 + g\frac{(\rho_1 - \rho_2)}{\rho}\left(\frac{H}{2} - z\right)} \tag{2.32}$$

and the solution at $z = 0$ is:

$$u_{toe}\left(L\right) = -\frac{C'aL}{4} + \frac{1}{2}\sqrt{\left(\frac{C'aL}{2}\right)^2 + 2g\frac{(\rho_1 - \rho_2)}{\rho}H} \tag{2.33}$$

Note that with the linear drag law assumption, the toe velocity solutions in the linear velocity profile energy balance and momentum balance models are identical with or without vegetation.

When drag dominates, *i.e.*, $\frac{u^2}{L} \ll \frac{C'au}{2}$, Equation 2.31 approaches:

$$\frac{C'au}{2} - \frac{(\rho_1 - \rho_2)}{\rho}\frac{g}{L}\left(\frac{H}{2} - z\right) = 0 \tag{2.34}$$

which yields:

$$u\,(z,\,L) = \frac{2g}{C'aL}\frac{(\rho_1 - \rho_2)}{\rho}\left(\frac{H}{2} - z\right) \tag{2.35}$$

Note that this solution is equivalent to Equation 2.3, and the velocity profile predicted from the momentum balance, in the linear drag regime and at the limit where inertia is negligible, exactly matches the assumed profile in the linear velocity profile energy balance model.

In conclusion, the solution for toe velocity derived from the momentum balance matches that derived from a linear velocity profile energy balance if a linear drag law is assumed. Otherwise, the two models match only in the absence of vegetative drag.

2.4.3 Drag coefficients in random arrays

As detailed above, the mathematical models employed in this study require the stem drag coefficient as an input parameter to predict the exchange flow velocity. Unfortunately, not enough is known about C_D in arrays for a value to be estimated with great confidence. C_D for isolated cylinders may be estimated by applying the observed toe velocities to the empirical equation [White, 1974]:

$$C_D \approx 1 + 10.0\,\mathrm{Re}^{-2/3} \tag{2.36}$$

However, complications arise for stem drag in an array of cylinders, which is more relevant to the present study. Nepf (1999) observed previously that drag in an array is suppressed for $\mathrm{Re} \geqslant 200$, a dependence that is not captured in White (1974)'s equation. In contrast, the presence of other stems appears to enhance drag in low Re ranges. An expression for cylinder drag in a random array of 5% solid volume fraction for $\mathrm{Re} < 35$ was obtained from numerical simulation results [Figure 26, Koch & Ladd, 1997]:

$$C_D \approx \frac{2}{\mathrm{Re}}\,(12 + 1.07\,\mathrm{Re}) \tag{2.37}$$

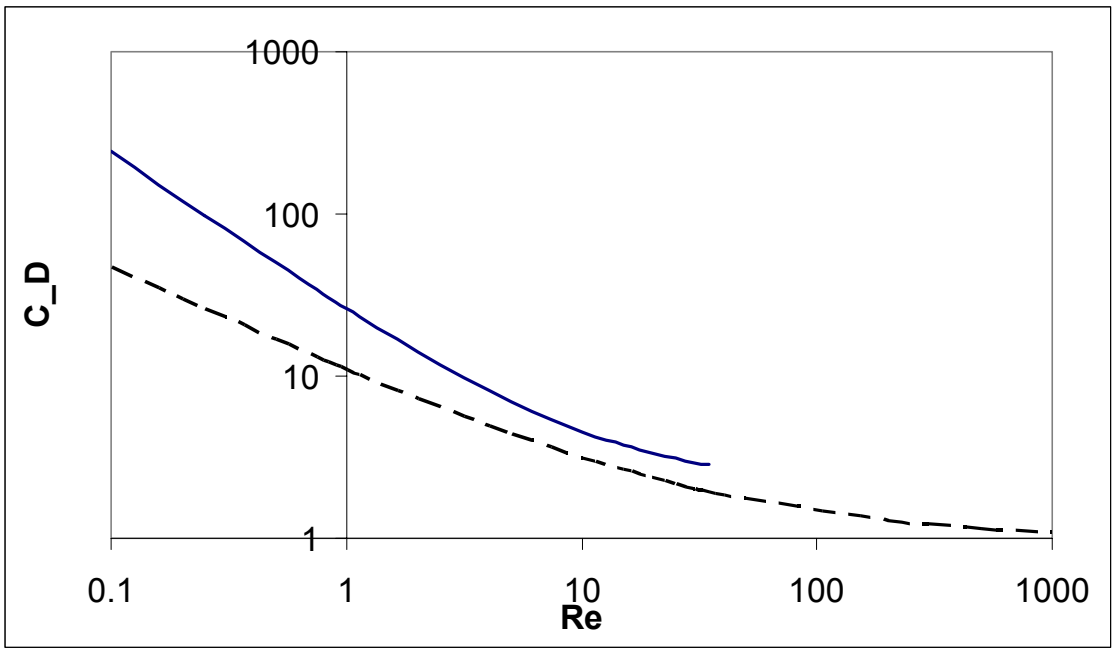

Figure 2-2: Re-dependence of the cylinder drag coefficient, C_D. Solid line represents an expression for C_D in a random cylinder arrays with a solid volume fraction of 5% presented in Koch & Ladd, 1997 (Equation 2.37). Perforated line represents drag for an isolated cylinder (Equation 2.36) from White, 1974.

which predicts a higher C_D than Equation 2.36 for $Re < 35$, as shown in Figure 2-2. A solid volume fraction of 5% is equivalent to a stem density of $a = 0.1\,\mathrm{cm}^{-1}$ for stems used in this study, and falls within the range of array conditions investigated in the laboratory.

In the Re range where both equations are valid, the difference in the C_D values obtained from these equations can be treated as a measure of uncertainty in the C_D. However, because $Re > 35$ in most scenarios, Equation 2.37 cannot be used to provide bounds on the drag in most of the flow conditions covered in this study.

Chapter 3

Experimental Methodology

As stated previously, lock-exchange flows is one type of gravity current that have been studied extensively through both laboratory experiments and numerical modeling. These flows can be reproduced easily in a laboratory tank by installing a removable partition in the middle. The two reservoirs in the tank are filled with fluids of different densities. When the partition is removed and the two fluids come in contact with each other, the resulting horizontal density gradient generates an exchange flow. The heavier fluid propagates towards the lighter fluid along the bottom of the tank and the lighter fluid compensates for this movement and propagates along the free surface in the opposite direction [Simpson, 1997].

The purpose of the experiments presented in this section was to estimate the frontal velocity and interface slope for a range of conditions. Specifically, the stem density and horizontal density gradient were varied between experimental runs to investigate the sensitivity of exchange flows to the presence of emergent vegetation under different flow velocities. The density gradient was generated by filling one reservoir with salt water and the other with tap water. By increasing the amount of salt added, a range of density differences could be tested.

3.1 Experimental Configuration

3.1.1 Tank and array characteristics

All experiments were conducted in a $71\,\text{in} \times 6\frac{1}{8}\,\text{in} \times 8\,\text{in}$ glass-walled tank with a horizontal metal bottom (Figure 3-1). The tank was separated into two reservoirs by a removable 3

± 0.5 mm thick vertical partition made of plastic that was positioned approximately $35\frac{1}{4}$ in from one end of the tank.

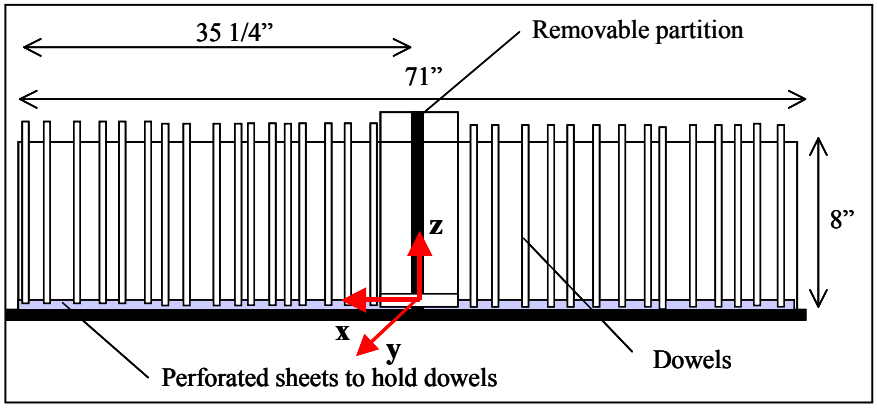

Figure 3-1: Schematic of the experimental tank and dowel arrays. Dimensions are in inches. Not to scale.

The Cartesian coordinate system used in this thesis is defined with its origin at the center of the tank and level with the perforated sheet surface that is in contact with the water, as illustrated in Figure 3-1. That is, all measurements of depth are relative to the perforated sheets and not the bottom of the tank. The x-axis is aligned with the direction of the underflow (longitudinal) and the z-axis is in the vertical direction normal to the bottom of the tank. This tank is modeled as a two-dimensional system.

Rigid maple dowels, $d = 0.6$ cm in diameter, were used as experimental models of aquatic vegetation. The dowels spanned the water column and penetrated the free surface at all times. Perforated polypropylene sheets with a density of 4 holes per in^2, in which these dowels were inserted, were placed at the bottom of the tank as a means of holding the dowels in place. Each sheet was $\frac{1}{4}$ in thick; two of these sheets were overlapped in each reservoir creating a $\frac{1}{2}$ in-thick base for the dowel array. The circular holes were $\frac{1}{4}$ in in diameter with staggered centers. In addition, as depicted in Figure 3-2, dowels were also glued onto the elevated portion at the middle of the tank to minimize the gaps in the dowel array due to the presence of the pieces of plastic that create the partition slot.

Under high density gradient and low stem density conditions, the exchange flow lifts the perforated sheets and the dowel array, which interferes with the experiments [Deardon, 2003].

Therefore, during experimental runs under such conditions, the dowel array was taped to the sides of the tank to keep it in place. This taping did not interfere with the experiment in any way.

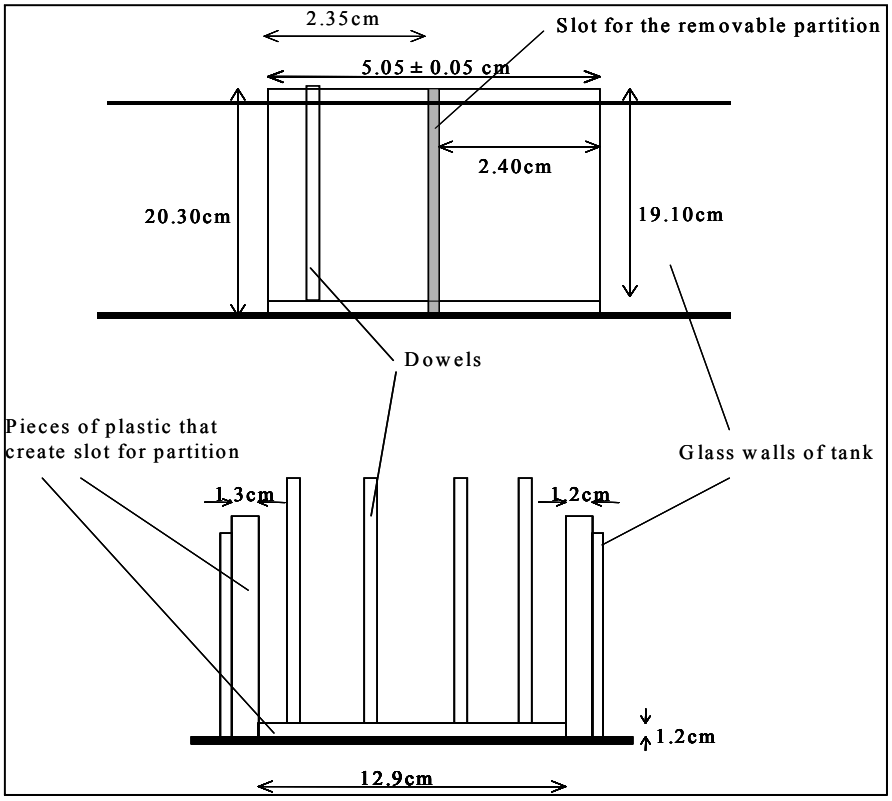

Figure 3-2: Sketch of the vertical partition at the middle of the tank. Dimensions are in cm, with an uncertainty of ± 0.05 cm. The top picture is a side view and the bottom picture is a cross-sectional view. Because perforated sheets could not be placed on the elevated portion at the middle of the tank, dowels were glued directly onto the plastic blocks that hold the partition at the bottom of the tank. Not to scale.

3.2 Experimental Procedure

3.2.1 Experimental scenarios

A range of stem densities and density gradients were reproduced in the laboratory by changing the total number of stems in the tank (N) and the amount of salt added (m_{salt}). One reservoir

was filled with salt water, the density of which (ρ_1 [kg / l]) was a function of m_{salt} and temperature. The other reservoir was filled with unaltered tap water, and its density (ρ_2 [kg / l]) varied only with temperature. The density difference between the two fluids is represented by the reduced gravity $\left[\mathrm{cm\,s^{-2}}\right]$:

$$g' \equiv g\frac{(\rho_1 - \rho_2)}{\overline{\rho}} \tag{3.1}$$

where $g = 9.8 \times 100\ \mathrm{cm\,s^{-2}}$ is the gravitational acceleration and $\overline{\rho}$ is the mean of ρ_1 and ρ_2. Its fractional uncertainty was estimated from the uncertainty in the density measurements using the Kline-McClintock (1953) uncertainty estimation method.

The stem density is described by the frontal area per unit volume $\left[\mathrm{cm^{-1}}\right]$:

$$a \equiv \frac{Nd}{A} \tag{3.2}$$

where A $\left[\mathrm{cm^2}\right]$ is the horizontal footprint of the tank and d [cm] is the dowel diameter. The fractional uncertainty of a is ± 0.005 based also on the Kline-McClintock (1953) method and assuming that the uncertainty in d is negligible. The estimated uncertainty in the mean water depth (H [cm]) is ± 0.6 cm, based on the maximum difference observed between the measured depths in the two reservoirs. The source of this discrepancy between the water depths in the two reservoirs is discussed in detail in the description of the experimental procedure.

The complete set of measurements taken during the experiments is tabulated in Chapter 4 (Table 4.1). Additionally, the relevant parameters that characterize the flow conditions in each of the experimental runs are summarized in Table 3.1. Note that the g' values presented here have been corrected for temperature, and the density values used to calculate them were slightly different from the uncorrected measurements presented in Table 4.1.

3.2.2 Comparison of flow and canopy conditions in the laboratory and the environment

Experimental conditions in this laboratory study were selected to reproduce characteristics of aquatic canopies and exchange flows that occur in the environment. Plant rigidity and height

are irrelevant in the present study, which is restricted to rigid, emergent vegetation. Therefore, the aquatic vegetation is characterized by its diameter and stem density. The plant diameter is typically on the order of 10^{-1} to 1 cm in the environment [*e.g.*, Leonard & Luther, 1995]. Accordingly, rigid circular dowels $d = 0.6$ cm in diameter were used in this study to model cylindrical wetland plants such as *Spartina alterniflora*. The dimensionless stem Reynolds numbers $\left(\mathrm{Re} = \frac{ud}{\nu}\right)$ calculated in this project are computed using this value for d. In all calculations, u is the longitudinal velocity of the denser fluid and ν is the mean kinematic viscosity of the two fluids. Stem densities in the environment are commonly on the order of $ad = 0.01 - 0.1$ [*e.g.*, Kadlec, 1990; Kalff, 2002], where ad is the dimensionless stem density parameter. Obviously, the lower limit on the stem density is $ad = 0$, which indicates the absence of vegetation. The range of stem densities examined in this thesis, $a = 0.0009\,\mathrm{cm}^{-1}$ to $0.115\ \mathrm{cm}^{-1}$, is equivalent to $ad = 0.0005 - 0.07$, which falls within the range observed in nature.

Flow can be characterized by its depth and velocity. Depths of vegetated waters vary significantly, but are typically on the order of 1 to 10 cm in natural aquatic systems [Kadlec, 1990; Leonard & Luther, 1995]. In this thesis, water depths were on average $H = 13.5$ cm. Velocities of exchange flows also vary significantly depending on the morphology of the aquatic system and the local conditions. Reported velocities for flows induced in shallow regions of a lake by spatial variations in temperature vary from 0.5 to 15 $\mathrm{cm\,s}^{-1}$ [*e.g.*, Kalff, 2002; MacIntyre *et al.*, 2002; Stefan *et al.*, 1989]. Frontal velocities of up to 10 $\mathrm{cm\,s}^{-1}$ ($\mathrm{Re} = 600$) were investigated in this study. Hence, the flow conditions recreated in the laboratory were within the range of conditions observed in nature.

As described in Chapter 1, density gradients are often driven by a gradient in salinity or temperature in natural systems. In freshwater systems, differential heating and cooling can generate spatial variability in temperature. For example, density gradients on the order of $10^{-8}\ \mathrm{kg\,cm}^{-1}\,\mathrm{l}^{-1}$ were observed between a littoral wetland and a lake based on temperature differences of $1-2\,^{\circ}\mathrm{C}$ [Andradóttir, 2000]. Salinity gradients typically develop across freshwater-salt water interfaces such as is found in estuaries and fjords [*e.g.*, Kalff, 2002; Simpson, 1997], and generally create larger density gradients. For example, density differences observed in oceans are 3% or less [Simpson, 1997]. The fractional density differences in the present study

ranged from 1% to 5%, which are similar to salinity gradients found in nature. Consequently, given that the length scale of the laboratory tank is several orders of magnitude smaller than that in nature, one would anticipate the density gradient in the experiments to be significantly larger than values typically observed in the environment. Indeed, the density gradients in the present laboratory experiments were on the order of 10^{-6} to $10^{-3}\,\mathrm{kg\,cm^{-1}\,l^{-1}}$.

3.2.3 Experimental procedure

The lock-exchange experiment requires two fluids of different densities. As stated above, unaltered tap water and salt water were used as the light and heavy fluid, respectively. The salt water was dyed with food coloring for flow visualization.

The initial step of the procedure was to prepare the dyed salt water fluid. For each run (Table 3.1) approximately 18 l of tap water and m_{salt} (CAS number: 7647-14-5) were added to a 20 ± 0.2 l plastic carboy. Then, approximately $2 - 10$ g of food dye was weighed and carefully rinsed into the carboy with tap water. Black dye was used in most of the experiment runs as it appeared to produce the best contrast in black-and-white images. The carboy was filled with tap water to the 20 l mark. Next, the carboy was placed on its side and rolled along the table until the salt had dissolved completely. Visual observation confirmed that observable amount of salt did not remain at the bottom of the tank, undissolved. Rolling the carboy for 2 minutes was sufficient for solutions with less than 400g of salt. In contrast, solutions with more than 1000 g of salt were left in the carboy overnight to allow the salt to dissolve completely.

Once the solution was well-mixed, the density of the dyed salt water from the carboy (ρ_1) and tap water (ρ_2) were measured using a hydrometer to $\pm 0.00025\,\mathrm{kg\,l^{-1}}$ (half of the smallest increment on scale). For tap water and salt water with density less than 1.040 $\mathrm{kg\,l^{-1}}$, a VWR $0.990 - 1.040$ $\mathrm{kg\,l^{-1}}$ hydrometer (Cat. number 34780-020) was used. A ERTCO^{TM} specific gravity hydrometer with a range 1.000 to 1.070 (Cat. number 2560) was used to measure the density of salt water when it exceeded 1.040 $\mathrm{kg\,l^{-1}}$. Because density is a function of temperature, the fluid temperature was also measured to $\pm 1\,^{\circ}\mathrm{C}$ using a thermometer immediately after the density measurement. Note that the density of the fluids was not measured in runs conducted before July 10, 2003. However, because the density of each fluid in each run was ultimately determined by a linear regression on the density and temperature measurements for

each salt mass, the lack of density measurements for runs 6, 8, 9, 11, and 12 were not critical. The temperature corrections of density measurements are discussed in detail in Section 3.4.

The carboy was emptied into the reservoir that is to the right from the camera's perspective (the side corresponding to negative x-coordinates in Figure 3-1). The other reservoir was filled simultaneously with tap water at a similar rate.

Once the dyed salt water was completely emptied into the reservoir, the water level of the tap water was adjusted to insure that the fluid level in the two reservoirs were the same. This adjustment was made by adding and removing the tap water until its free surface was aligned with that of the dyed salt water, taking advantage of the fact that the free surface of fluids are always horizontal. This alignment of the free surfaces was performed in experiments conducted after October 29th, 2003 (see Table 4.1 for a list of all experimental runs and the corresponding dates). In prior runs, the water level was adjusted by filling the tap water reservoir until both reservoirs had the same *measured* water depth.

Adjustment of water level was necessary because the free surfaces were discontinuous across the partition when the water level was determined by setting the water depths to be equal between the reservoirs. Under close inspection, it was observed that when the free surface in the two reservoirs were aligned, the water depth, the distance between the array sheet and the free surface, differed not only between the two reservoirs, but varied within each reservoir as well. This variation is attributed to the non-uniformities in the perforated sheets that are placed at the bottom of the tank. These flexible sheets do not lie perfectly flat at the bottom of the tank because of the sealant around the perimeter of the tank bottom and the sealant used to hold the plastic blocks that make the slot for the partition in place. Indeed, the elevation of the perforated sheet above the bottom of the tank varies by about 5 mm in each reservoir. For the purposes of mathematical analysis, water depth was assumed to be constant at the mean water depth with an uncertainty of ± 0.6 cm to account for the spatial variations in the water depth. The water depths were measured using a ruler to ± 0.1 cm.

The fluids were left undisturbed for approximately 5 minutes to allow them to equilibrate with the room temperature prior to measuring their temperature. However, persistent differences in temperature between the fluids in the two reservoirs were observed in some runs even after half an hour. The cause of the temperature differences, which were as large as 3 °C in

some runs, could not be determined. The temperature in both reservoirs were recorded using a partially-submerged thermometer. The uncertainty in the temperature measurements were $\pm 1\,^{\circ}\mathrm{C}$.

Each experimental run consisted of removing the partition in the middle of the tank and capturing the propagation of the two fluids into each other's reservoirs with the CCD camera. An experimental run ended when the front was approximately one water depth away from the end of the tank. This procedure was repeated for all experimental runs tabulated in Table 3.1.

3.3 Image Processing

The quality of the captured images was very sensitive to lighting. Four 40 W, 48 in fluorescent lamps were held horizontally behind the tank on clamp stands so that the tank was in between the camera and the lights (see Figure 3-3). Two lights were positioned behind each reservoir: one just below the free surface and one just above the perforated sheet. A layer of thin, white craft paper was taped onto the side of the tank to diffuse the light and to provide a uniform background in the images. This lighting format was only developed at the end of October 2003; experiments prior to October 28, 2003 (run numbers 20 and less) were conducted under room lighting only.

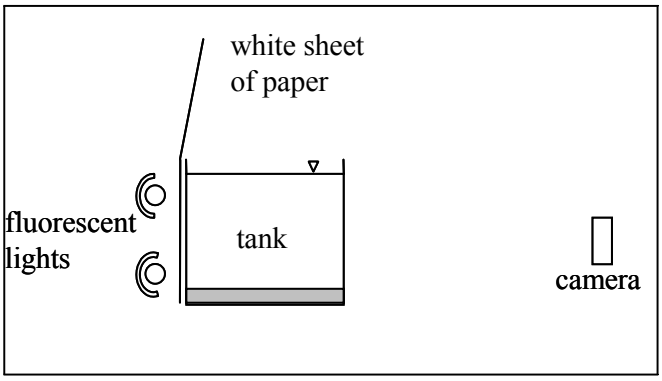

Figure 3-3: Sketch of the relative positions of the lights and camera with respect to the tank. Not to scale.

All experiments were recorded using a Pulnix TM-9701 CCD camera mounted on a tripod. The camera and tripod were aligned visually to the tank and the free surface so that the camera

axes were parallel with the free surface and the edges of the tank. Both the aperture and the capture rate varied between runs. The amount of light that passed through the tank was sensitive to the stem density, with dowels acting as obstructions between the light source and the camera. After the aperture was set to maximize the contrast between the dowels and the dyed fluid, the capture rate was selected for each experimental run by comparing the specific experimental scenario to that of prior experiments and choosing a rate that was likely to capture approximately 10 images during the course of the experiment. However, the maximum capture rate available was 2 s per frame. With this restriction, only 6 images could be captured during the highest density difference experiments.

A sequence of 640 $\times$ 480 bitmap images were captured by the CCD camera at the specified rate and transferred to a PC with a Windows NT operating system using the software FlashBus^{TM} MV Version 3.91 09/07/00 by Integral® Technologies, Inc.. Image processing was conducted entirely using MATLAB® 6.5, the Optimization Toolbox 2.2, and the Image Processing Toolbox 3.2 on a Dell Inspiron 8200 notebook with a Windows XP operating system.

First, the bitmap images were converted to binary images using a manually selected threshold that appeared, by visual inspection, to most accurately identify the pixels corresponding to the dyed fluid as black. This threshold varied between runs due to the sensitivity of the images to small changes in lighting and stem densities. The position of the interface in each image was extracted and stored in MAT files (*.mat) by a code that was modified from one developed by Landry (2003). This code found the position closest to the free surface where the pixels first changed their value from 1 (white) to 0 (black) or vice versa in each of the 640 columns. In this manner, the interface position in each column was converted to data points, each with a $x-$ and $z-$ coordinate.

The presence of dowels greatly affected the appearance of the interface in the images. Its most significant impact was the spatial variation in the lighting intensity that resulted from dowels blocking the light along its longitudinal position. As can be seen in Figure 3-4, the interface position appears lower where there are no dowels behind it because of the greater light intensity in such positions. Because the data analysis assumes that the interface position (z-coordinates of the data points) is monotonously decreasing with increasing x, data points either in the parts where light intensity is reduced because of dowels or in the parts without

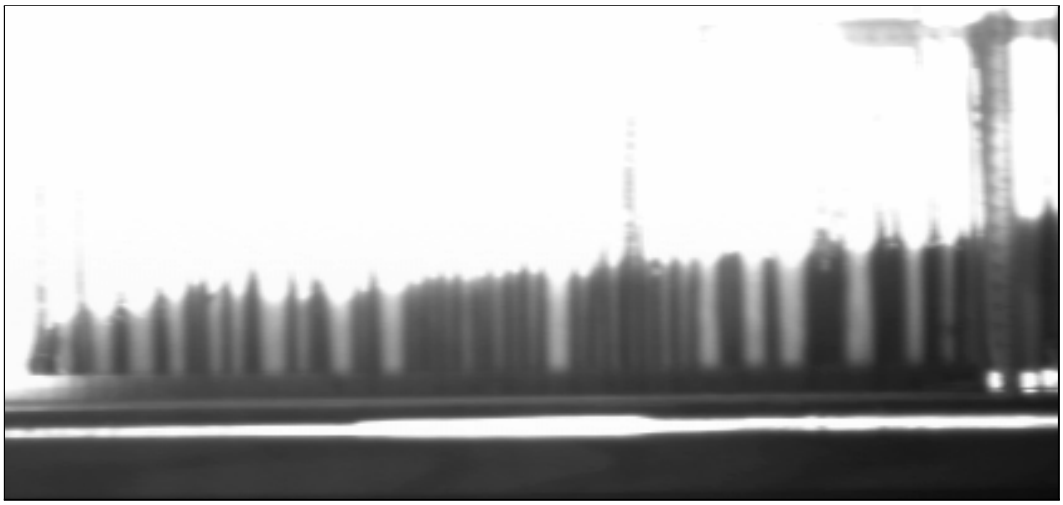

Figure 3-4: Example of a bitmap image taken during an experimental run. This image was taken during run 22: $a = 0.0428 \pm 0.0002$ cm^{-1} and $g' = 7.5 \pm 0.5\,\mathrm{cm\,s^{-2}}$.

dowels had to be removed to ensure that the data points that were analyzed were obtained with similar background light intensities. Which points were removed varied between each run, and the method that removed the least number of data points were chosen. Where large gaps in the interface formed as a result of this procedure, data points were added manually so that the data points were as evenly distributed along the interface as possible. The addition and removal of data points were performed manually using a MATLAB® code developed by Landry (2003).

Lastly, the images from each run were spatially calibrated by scaling the minimum and maximum z-coordinates in all of the images in each run with the corresponding mean water depth. Using the resulting spatial calibration, the interface positions were translated from pixels into units of length [cm].

3.4 Analysis

3.4.1 Temperature corrections to density measurements

As explained previously, the density of the dyed salt water and tap water were measured prior to each experimental run using a hydrometer. However, the temperatures of the fluids –

hence their densities – often changed while the fluids settled in the tank after the density measurements were taken. Linear regressions were performed on density measurements for each m_{salt} value with more than one measurement: $m_{salt} = 0\,g$ (tap water), $10.00\,g$, $50.00\,g$, $100.00\,g$, $190.00\,g$, and $300.00\,g$. Note that the linear regression for tap water and $m_{salt} = 100.00\,g$ solution was performed prior to runs 21, 23, 26-29. Note also that density and temperature measurements not associated with runs that were analyzed in this study were also included in the linear regressions. Linear functions were also fitted to measurements for salt water with $m_{salt} = 500.00\,g$, $502.43\,g$, and $503.38\,g$ (Equation 3.6) and $m_{salt} = 750.00\,g$ and $750.76\,g$ despite the slight inconsistencies in the amounts of salt added. From observation, the minor differences in salt masses appear to have had a negligible impact on the linear regressions, which justifies the inclusion of measurements for slightly different salt masses in the linear regressions for $m_{salt} \sim 500\,g$ and $750\,g$. Also, differences in the mass of dye added was assumed to have had negligible impact on the density, which is consistent with Deardon (2003)'s observations.

Equations 3.3 - 3.6 describe the best-fit lines in the least-squared sense through the density and the corresponding temperature measurements that were made for m_{salt} values with four or more density measurements. Temperature T is in units of [°C] and density ρ_1 is in units of $\left[\mathrm{kg\,l^{-1}}\right]$.

$$\rho_1\,(m_{salt} = 0.00\,g) = -1.3467 \times 10^{-4} T + 1.0001 \qquad r^2 = 0.86 \tag{3.3}$$

$$\rho_1\,(m_{salt} = 10.00\,g) = -1.3998 \times 10^{-5} T + 0.9987 \qquad r^2 = 0.0025 \tag{3.4}$$

$$\rho_1\,(m_{salt} = 100.00\,g) = -1.5784 \times 10^{-4} T + 1.0046 \qquad r^2 = 0.88 \tag{3.5}$$

$$\rho_1\,(m_{salt} \sim 500\,g) = -8.1822 \times 10^{-5} T + 1.0185 \qquad r^2 = 0.18 \tag{3.6}$$

These linear regressions were then used to compute the temperature-adjusted densities of the tap water and the dyed salt water in each run to correct for any changes in temperature that occurred immediately before the runs. The slope of these linear regressions is consistent with published work [UNESCO, 1987]. For example, a linear regression on density predictions for water ($m_{salt} = 0.00\,g$) at linearly equally spaced temperatures in the range $T = 5\,°C$ to $25\,°C$

by UNESCO (1987)'s expression yields:

$$\rho\,(\mathrm{m}_{salt} = 0.00\,\mathrm{g}) = -1.48 \times 10^{-4} T + 1.0011 \qquad r^2 = 0.95 \tag{3.7}$$

In contrast, robust linear regressions could not be derived for m_{salt} values for which 3 or less measurements were available. These were m_{salt} = 50.00 g, 190.00 g, 300.00 g, 700.00 g, 750 g, 1000.00 g, 1393.80 g, and 1468.77 g. However, all twelve runs associated with these m_{salt} values (Table 3.1) experienced a temperature difference that was within the uncertainty range of the thermometer. As such, the linear regressions obtained from the limited measurements were used to estimate temperature-adjusted density values. For runs with m_{salt} that were not repeated (runs 1, 2, 16, and 17), temperature corrections were not made to the measurements.

The maximum difference in temperature observed during the preparation of any experiment was 3 °C. This translates to a 0.04% density change in tap water. Figure 3-5 displays hydrometer measurement data against their temperature and the corresponding linear regressions. Note that not all density measurements taken during the experimental runs analyzed were included in the linear regressions. The measurements taken in 2004 were excluded, as the analysis was conducted prior to those runs. Furthermore, some of the measurements that were included in the linear regressions were made during experiments that were later excluded from analyses due to technical problems with imaging. Because these problems did not affect density measurements in any way, the density data were included in the linear regressions to improve the accuracy of the regressions.

3.4.2 Computation of the linear drag constant C' from the images

In Chapter 2, a constant of proportionality $C' \equiv C_D u$ was defined for the linear drag regime. A best fit C' was computed for pairs of consecutive images in each experimental run that exhibited a linear interface and non-inertial front propagation by the momentum balance model. Because C' is independent of Re and z, the parameter was evaluated in a given run based on the propagation of the interface between pairs of images, as described below.

Because the interface rotates about $z = \frac{H}{2}$, the velocity near the middle of the interface is very small and the fractional uncertainty correspondingly large. Also, the interface was clearer

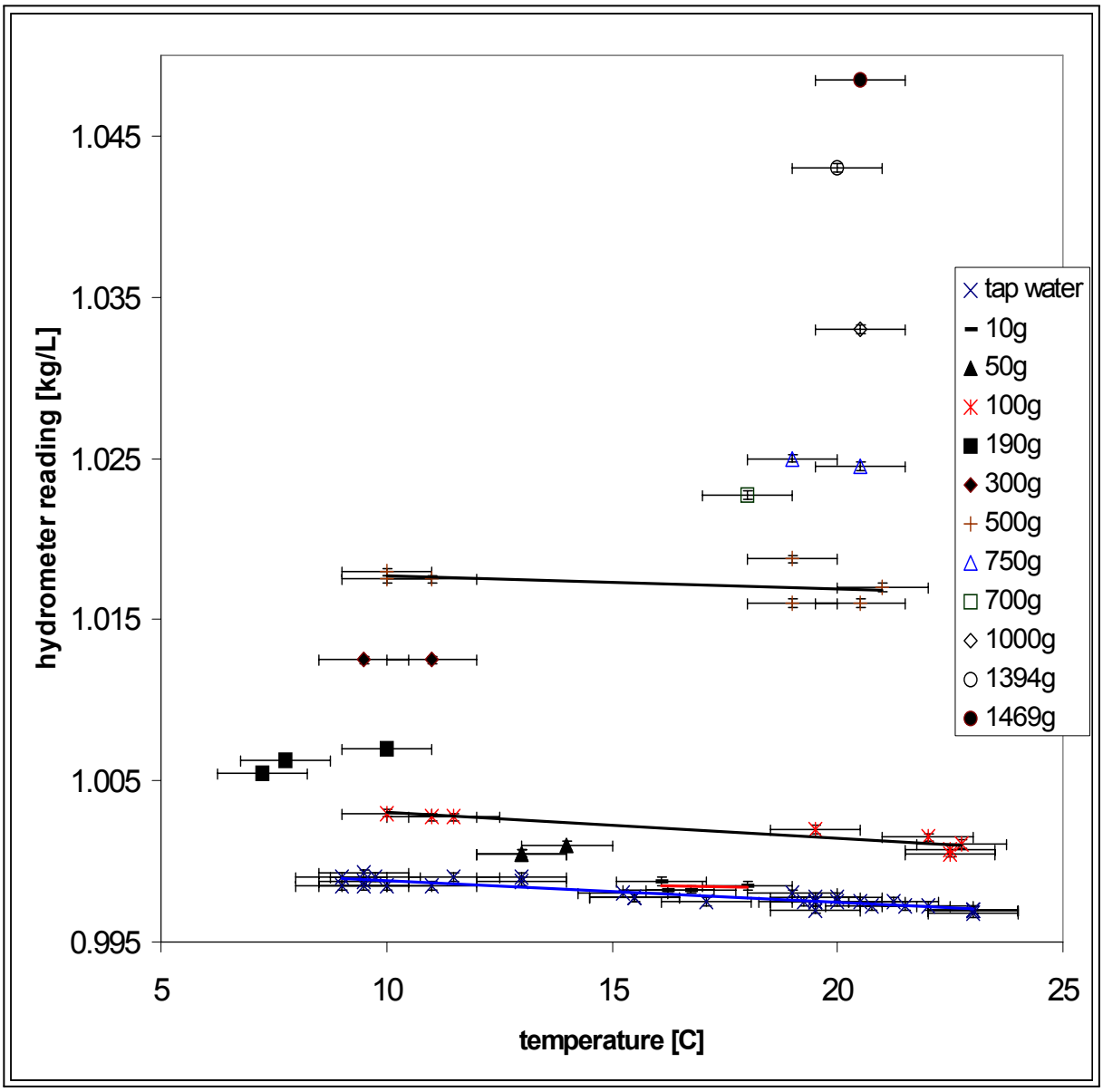

Figure 3-5: Temperature-dependence of density measurements. Key indicates m_{salt}. Vertical bars represent uncertainty in the hydrometer readings: $\pm 0.00025\,\mathrm{kg\,l^{-1}}$. Horizontal bars represent uncertainty in the temperature readings: $\pm 1\,^{\circ}\mathrm{C}$. The four solid lines represent the linear regressions for m_{salt} = 0.00g, 10.00g, 100.00g, 500g (Equations 3.3 - 3.6).

where dyed fluid was moving into clear water. Therefore, fitted data were restricted to $z < \frac{H}{4}$ to maximize the accuracy of the data.

Not all images available can be used to determine C'. Because the toe position was required to determine L, a necessary parameter in the momentum balance model, images in which the presence of the stems interfered with the identification of the toe had to be neglected from the analysis. Furthermore, to ensure that the initial disturbance from removing the partition and the effects of the end of the tank do not manifest in the results, only images where the toe had propagated a minimum of $1.5H$ but was more than H away from the ends of the tank were considered.

The MATLAB® code started at the fourth image ($i = 4$) and tested subsequent images until an image with an extractable L that satisfied the condition $3H \leqslant L < 180 - 2H$ was found. This image was now defined as $i_{current}$. Then, the code searched images prior to the present one for an image with an extractable L. To insure sensitivity, the search was restricted to the three images prior to the present image. That is, the previous image $i = i_{current} - 1$ was examined first. If L could not be determined, the code proceeded to the image $i = i_{current} - 2$, and then image $i = i_{current} - 3$. If none of these three images satisfied the condition, the process was repeated with the next image that has an extractable L until a pair of images within 3 images of each other with known L were found. Then, the code calculated a C' that best described the interface progression between the pair of images in the least-squares sense. In the following description of this computation of C', the two images in the pair are referred to as $i_{previous}$ and $i_{current}$.

First, the interface position in both images was determined. Because data points were not necessarily available at the same depths in both images, the interface positions were interpolated from the available data points. This was done by fitting a polynomial of degree 3 to the data points in that image at $z < \frac{H}{4}$ and evaluating the polynomial at 10 specified depths.

Then, if $L\left(i_{current}\right) > L\left(i_{previous}\right)$, a C' that best predicted the interface position at the 10 specified depths was determined. The interface position was predicted by stepping from image $i_{previous}$ to $i_{current}$ with a given C'. Starting at the interpolated interface position at each of the specified 10 depths in image $i_{previous}$, the program stepped 60 times with a given C' to predict the position of the interface in image $i_{current}$. Note that doubling the number of

time steps between images from 60 steps to 120 steps had negligible impact on the estimated C': the difference in the two C' estimates as a fraction of their average ranged from -0.01% to -0.29% across the runs. These differences are negligible compared to the variability in the C' estimate within each run, with the standard deviation of C' estimates in individual runs ranging from 5% to 44%. In each step, the velocities at the specified depths were calculated using the solution for velocity $u(z)$ derived from the momentum balance (Equation 2.32). The expression for velocity in step n was:

$$u(z)_n = -\frac{C'aL_n}{4} + \sqrt{\left(\frac{C'aL_n}{4}\right)^2 + g'\left(\frac{H}{2} - z\right)} \tag{3.8}$$

where L at step n was estimated by:

$$L_n = 2x_n|_{z=0} \tag{3.9}$$

$x_n|_{z=0}$ is the interface position at $z = 0$ for step n.

Then, the interface traveled a distance of $\Delta x(z)_n = u(z)_n \times \Delta t$ where $\Delta t = \frac{t_{i_{current}} - t_{i_{previous}}}{60}$ was the time step between each incremental step. The new position of the interface was then calculated to be:

$$x(z)_{n+1} = \Delta x(z)_n + x(z)_n \tag{3.10}$$

After $n = 60$ time steps the difference between the predicted and observed position was noted. The entire process was iterated over a range of C' values with the initial guess at $C' = 2\,\mathrm{cm\,s^{-1}}$. C' values were restricted to the range $-0.5\,\mathrm{cm\,s^{-1}} < C' < 30\,\mathrm{cm\,s^{-1}}$, which generously encompassed C' values that were anticipated based on previously published C_D data. Moreover, an increase in the specified upper limit of C' from $C' < 30\,\mathrm{cm\,s^{-1}}$ to $C' < 60\,\mathrm{cm\,s^{-1}}$ did not affect the results in any way; this lack of sensitivity verifies that the chosen range for C' is conservative. The value of C' giving the minimum difference between the observed and predicted longitudinal position at the specified depths in the least-squared sense was chosen as C'. In this manner, a C' was determined for every pair of images analyzed in a run.

Figure 3-6 represents this algorithm graphically. In the example depicted in Figure 3-6,

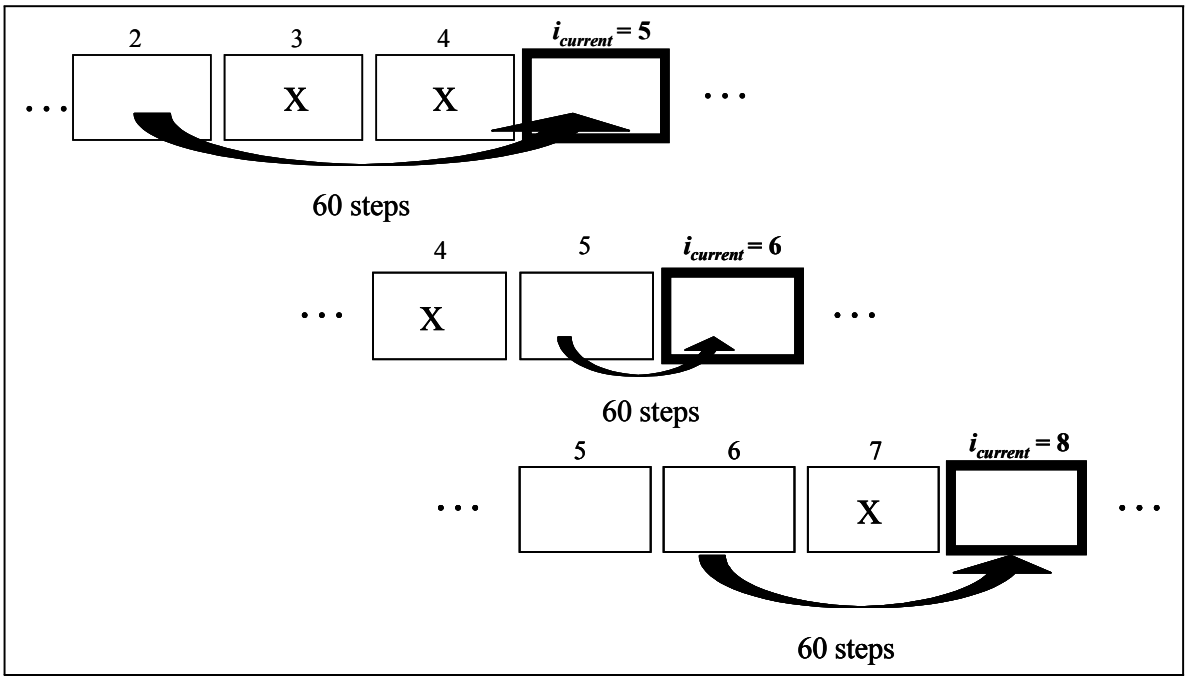

Figure 3-6: Schematic representation of the algorithm employed to determine C' values between pairs of images. Each rectangle represents an image; the bold rectangle is the current image for that pair of images. "X" indicates images from which the toe position, hence L, of the front could not be extracted; the code neglected these images. The arrow indicates the pair of images between which C' is determined.

the first image after $i = 3$ that has an extractable L is image $i_{current} = 5$. The code searches earlier images $i < i_{current}$ in descending order to find the closest image with an extractable L; in this example image $i = 2$ is selected as the starting point. The code then determines the C' that best predicts the interface position in image $i = 5$. The code then proceeds to the next image with an extractable L, $i_{current} = 6$, and the process is repeated and a C' is estimated between images $i = 5$ and $i = i_{current}$. The next pair of images is images $i = 6$ and $i_{current} = 8$, because L could not be extracted from image $i = 7$. This procedure continues until the last image in the sequence.

run number	total number of stems, N	frontal area per unit volume, a	mass of salt added	reduced gravity, g'	uncertainty in g' as a fraction of g'	mean water depth, H
	[stems]	[stems/cm]	[g]	[cm/s2]	[ ]	[cm]
1	540	0.1155	1393.80	44.2	0.01	14.0
2	540	0.1155	1468.77	49.2	0.01	14.2
3	540	0.1155	500.00	19.1	0.03	13.5
4	400	0.0855	100.00	3.8	0.1	13.5
5	300	0.0642	100.00	4.0	0.1	13.7
6	100	0.0214	100.00	3.9	0.1	13.3
7	540	0.1155	100.00	3.9	0.1	13.9
8	20	0.00428	100.00	3.9	0.1	13.2
9	50	0.01069	100.00	3.9	0.1	13.3
11	4	0.000855	100.00	3.9	0.1	13.5
12	540	0.1155	10.00	1.2	0.4	13.9
13	400	0.0855	100.00	3.9	0.1	13.7
14	540	0.1155	502.43	18.9	0.03	13.7
16	540	0.1155	700.00	24.4	0.02	14.3
17	540	0.1155	1000.00	34.4	0.01	13.8
18	540	0.1155	500.00	18.9	0.03	13.9
19	540	0.1155	750.00	26.6	0.02	14.0
20	540	0.1155	100.00	4.0	0.1	14.0
21	200	0.0428	100.00	3.9	0.1	13.0
23	400	0.0855	100.00	4.2	0.1	13.4
26	50	0.01069	190.00	7.1	0.07	12.8
27	100	0.0214	190.00	6.5	0.07	12.9
28	20	0.00428	100.00	4.2	0.1	12.8
29	50	0.01069	100.00	4.4	0.1	13.0
30	300	0.0642	10.00	0.6	0.8	13.6
31	300	0.0642	10.00	0.5	1	13.4
32	300	0.0642	10.00	0.5	1	13.4
33	300	0.0642	50.00	2.2	0.2	13.4
34	300	0.0642	50.00	2.1	0.2	13.5
35	300	0.0642	50.00	1.9	0.3	13.3
36	300	0.0642	100.00	4.0	0.1	13.5
37	300	0.0642	100.00	4.0	0.1	13.4
38	300	0.0642	100.00	4.0	0.1	13.3
39	300	0.0642	300.00	13.3	0.04	13.1
40	300	0.0642	300.00	13.3	0.04	13.4
42	300	0.0642	500.00	18.3	0.03	13.3
43	300	0.0642	500.00	18.3	0.03	13.4
44	300	0.0642	500.00	18.3	0.03	13.3

Table 3.1: Summary of experimental conditions for each run.

Chapter 4

Results and Discussion

4.1 Comparison of Experimental Observations and Theoretical Predictions of Toe Velocity

This section presents a comparison between experimental observations and theoretical predictions of toe velocity made by the mathematical models described in Chapter 2. Recall that the mathematical expressions for toe velocity (u_{toe}) were derived in Chapter 2 from the momentum balance and energy balance models by evaluating them at $z = 0$ (Equations 2.13, 2.14, and 2.22). The expressions are reiterated here for convenience:

$$u_{toe} = \sqrt{\frac{g'H}{2 + \frac{3}{4}C_D aL}} \tag{4.1}$$

$$u_{toe} = \sqrt{\frac{g'H}{2\,(2 + C_D aL)}} \tag{4.2}$$

$$u_{toe} = \sqrt{\frac{g'H}{2 + C_D aL}} \tag{4.3}$$

Equations 4.1 and 4.2 were derived from energy conservation assuming a linear velocity profile and block flow, respectively. Equation 4.3 was derived from momentum conservation. The parameters g', H, and a were controlled in each run (Table 3.1) and L is the length of the density current, which varies from 0 cm to 180 cm in these experiments. In lock-exchange flows,

						temperature		hydrometer (uncorrected)			
Run Number	Date	N	a	salt	dye	water	dyed saltwater	density : water	T	density : dyed saltwater	T
			+- 0.5%	+- 0.05g	+- 0.05g	+- 1 C	+- 1 C	+- 0.00025 kg/L	+- 1 C	+- 0.00025 kg/L	+- 1 C
		[stems]	[stems/cm]	[g]	[g]	[C]	[C]	[kg/L]	[C]	[kg/L]	[C]
1	07/23/03	540	0.1155	1393.80	2.70	22.8	20.5	0.9970	23.0	1.0430	20.0
2	07/24/03	540	0.1155	1468.77	2.79	22.0	21.0	0.9970	23.0	1.0485	20.5
3	07/13/03	540	0.1155	500.00	2.22	21.5	21.0	0.9975	21.25	1.0170	21.0
4	07/12/03	400	0.0855	100.00	2.25	22.0	22.5	0.99675	23.0	1.00075	22.5
5	07/10/03	300	0.0642	100.00	2.07	23.0	22.5	0.9970	23.0	1.0005	22.5
6	07/09/03	100	0.0214	100.00	2.79	22.2	**N/R**	**N/R**	**N/R**	**N/R**	**N/R**
7	07/14/03	540	0.1155	100.00	2.24	22.0	22.0	0.99725	21.5	1.0011	22.75
8	07/09/03	20	0.00428	100.00	2.11	22.5	**N/R**	**N/R**	**N/R**	**N/R**	**N/R**
9	07/09/03	50	0.01069	100.00	2.60	22.5	**N/R**	**N/R**	**N/R**	**N/R**	**N/R**
11	07/08/03	4	0.000855	100.00	2.39	22.5	**N/R**	**N/R**	**N/R**	**N/R**	**N/R**
12	07/07/03	540	0.1155	10.00	**N/R**	22.0	**N/R**	**N/R**	**N/R**	**N/R**	**N/R**
13	07/11/03	400	0.0855	100.00	2.22	22.0	22.0	0.99725	22.0	1.0015	22.0
14	10/07/03	540	0.1155	502.43	2.08	19.0	19.0	0.9970	19.5	1.01875	19.0
16	10/07/03	540	0.1155	700.00	2.50	18.5	18.0	0.9975	19.5	1.02275	18.0
17	10/09/03	540	0.1155	1000.00	2.32	20.0	20.0	0.9975	19.5	1.0330	20.5
18	10/09/03	540	0.1155	500.00	2.11	19.0	19.0	0.9975	20.0	1.0160	19.0
19	10/09/03	540	0.1155	750.00	2.10	19.0	19.0	0.9978	19.5	1.0250	19.0
20	10/09/03	540	0.1155	100.00	2.01	19.0	19.0	0.9975	19.25	1.0020	19.5
21	02/04/04	200	0.0428	100.00	8.00	7.0	9.5	0.9990	8.75	1.0020	9.0
23	02/04/04	400	0.0855	100.00	**N/R**	7.0	7.5	0.9988	10.00	1.0025	8.0
26	01/29/04	50	0.01069	190.00	7.1	10.0	8.0	0.9990	8.0	1.0055	7.3
27	01/29/04	100	0.0214	190.00	9.6	9.0	7.0	0.9993	9.5	1.00625	7.8
28	01/29/04	20	0.00428	100.00	7.60	7.5	8.0	0.9990	7.5	1.0025	7.3
29	01/29/04	50	0.01069	100.00	6.45	8.5	7.0	0.9993	10.0	1.00225	7.0
30	10/28/03	300	0.0642	10.00	4.18	16.9	17.5	0.9975	17.1	0.9985	18.0
31	11/04/03	300	0.0642	10.00	8.44	16.0	16.3	0.9980	15.3	0.99825	16.8
32	11/04/03	300	0.0642	10.00	8.01	15.9	16.0	0.9978	15.5	0.99825	16.3
33	11/20/03	300	0.0642	50.00	8.93	14.0	13.0	0.9990	13.0	1.001	14.0
34	11/20/03	300	0.0642	50.00	8.61	13.0	13.0	0.9988	13.0	1.0005	13.0
35	12/02/03	300	0.0642	50.00	9.16	11.5	13.0	0.9990	11.5	1.0005	13.0
36	12/02/03	300	0.0642	100.00	8.58	10.5	11.5	0.9985	11.0	1.00275	11.5
37	12/09/03	300	0.0642	100.00	9.45	10.0	11.0	0.9993	9.5	1.00275	11.0
38	12/09/03	300	0.0642	100.00	9.05	9.0	10.0	0.9990	9.0	1.003	10.0
39	12/11/03	300	0.0642	300.00	8.64	9.0	11.0	0.9985	10.0	1.0125	11.0
40	12/11/03	300	0.0642	300.00	9.74	9.0	10.0	0.9985	9.0	1.0125	9.5
42	12/09/03	300	0.0642	500.00	9.25	9.0	10.0	0.9988	9.5	1.0175	11.0
43	12/09/03	300	0.0642	500.00	8.60	9.0	10.0	0.9990	9.8	1.01795	10.0
44	12/09/03	300	0.0642	500.00	8.64	9.0	10.0	0.9985	9.5	1.0175	10.0

N/R denotes not recorded.

Table 4.1: All measurements recorded during the experiments

the latter increases monotonously with time; hence, L is analogous to time. For consistency between cases, Equation 2.36 was used to calculate the drag coefficient, with an expectation that as stem density (ad) increases, the actual drag coefficient diverges from the values for an isolated stem, as discussed in Chapter 2. It should be noted that the disagreement may be substantial: C_D may drop as much as 50% between $ad \approx 0.01$ and $ad \approx 0.1$ at Re $\geqslant 200$ [Nepf, 1999]. Any disagreement in C_D will contribute to the uncertainty in the predictions.

The toe velocity for each run is determined from experimental observations as the rate of displacement of the toe. The current data are not ideal for this analysis, because the images were recorded to allow for the observation of the shape of the interface. To satisfy this requirement, the CCD camera was placed on a stationary tripod, as described in Chapter 3; the entire length of the tank was captured in all runs except for runs 21, 23 and 26-29, in which half of the tank was recorded. Accordingly, the precision of the images was decreased, with pixel-to-length scales approximately in the range 3 pix cm^{-1} to 9 pix cm^{-1}. Furthermore, the toe was difficult to distinguish from a dowel in high stem density scenarios because the images were captured from a distance and were not in color. Owing to these factors, the position of the toe could not be determined in many of the images, and where the position could be estimated, the anticipated uncertainty in L is large in magnitude and difficult to quantify.

Instead, data obtained by Deardon (2003) in the same laboratory facility were used in this analysis. Contrary to the present study, Deardon (2003)'s work focused solely on observing the toe velocity of the undercurrent. As a result, the toe was recorded with a camcorder that moved with the front, and the position of the toe was obtained directly by a reading the measuring tape that was glued to the bottom of the tank [Deardon, 2003]. Consequently, Deardon (2003)'s toe velocity data are more accurate than the experimental observations in the present study.

Deardon (2003)'s observed toe velocities are presented as discrete data points in Figures 4-1 − 4-4. First and foremost, note that the density current propagated with a constant velocity in the absence of stems, as displayed in Figure 4-1, with a coefficient of determination of $r^2 = 0.04$, 0.02, 0.12, 0.28, and 0.23 associated with the linear regression for $g' = 4.1\,\mathrm{cm\,s^{-2}}$, $8.9\,\mathrm{cm\,s^{-2}}$, $13.2\,\mathrm{cm\,s^{-2}}$, $18.5\,\mathrm{cm\,s^{-2}}$, and $24.0\,\mathrm{cm\,s^{-2}}$, respectively. These r^2 values indicate that there is insignificant evidence of a linear correlation between the toe velocity and L in the absence

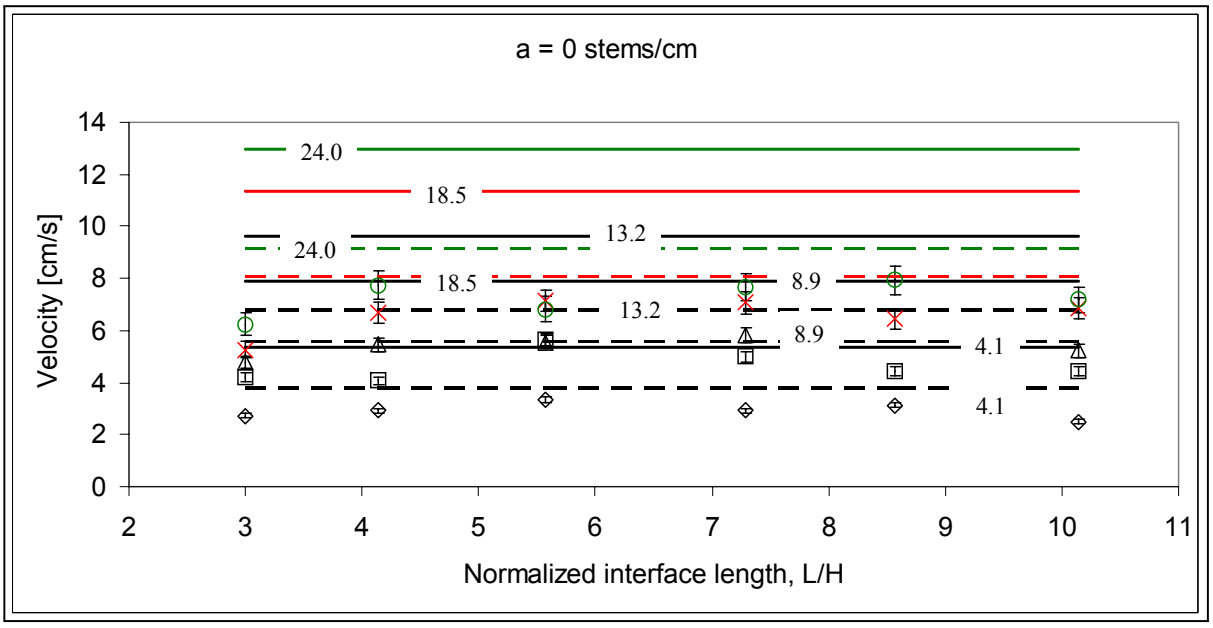

Figure 4-1: Toe velocity time series for runs with no vegetation. Five runs with different density differences are presented: $g' = 4.1\,\mathrm{cm\,s^{-2}}$ ($\diamond$); $8.9\,\mathrm{cm\,s^{-2}}$ ($\square$); $13.2\,\mathrm{cm\,s^{-2}}$ ($\triangle$); $18.5\,\mathrm{cm\,s^{-2}}$ ($\times$); and $24.0\,\mathrm{cm\,s^{-2}}$ ($\circ$). Vertical bars represent uncertainty in the toe velocity observations. Numerical labels on the solid lines represent g' [$\mathrm{cm\,s^{-2}}$]. Solid lines represent predictions based on Equation 4.1. Dashed lines represent predictions based on Equation 4.2. Data from Deardon, 2003.

of stems [Taylor, 1997]. This lack of variability of the toe velocity with L is consistent with previous studies on lock-exchange flows, which have found the front velocity to be constant with time in the absence of obstructions [Simpson, 1997]. This signifies that energy dissipation due to friction is negligible, further supporting the removal of the stress term from the momentum balance model. The experimental observations display better agreement with the block flow energy balance model predictions than the other two models, consistent with previous studies and the observed interface profile. Since the behavior of unobstructed lock-exchange flows has been studied extensively, no further comments will be made on these non-vegetated runs.

In contrast, the density currents exhibit a significant decrease in toe velocity with L when propagating through stems, as shown in Figures 4-2 – 4-4. This decrease in velocity observed in the runs with $a \geqslant 0.0428\,\mathrm{cm^{-1}}$ can be ascribed to the stem drag and the associated energy dissipation.

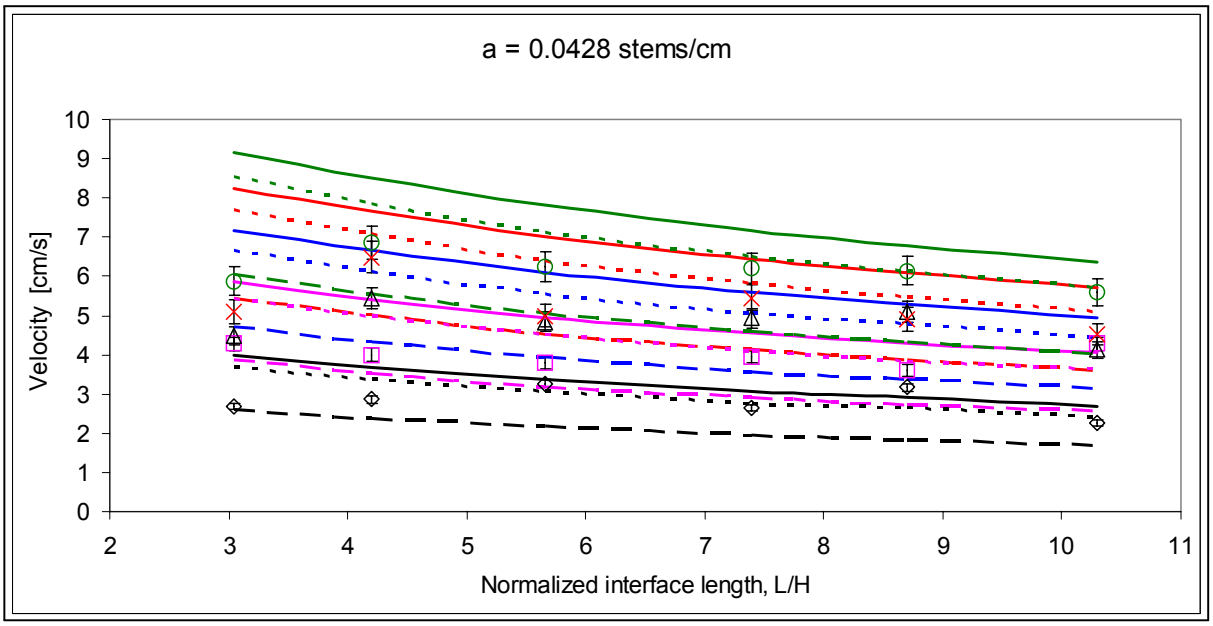

Figure 4-2: Toe velocity time series for runs with stem density $a = 0.0428\,\mathrm{cm}^{-1}$. Five runs with different density differences are presented: $g' = 4.3\,\mathrm{cm\,s}^{-2}$ ($\diamondsuit$; black); $9.2\,\mathrm{cm\,s}^{-2}$ ($\square$; pink); $13.7\,\mathrm{cm\,s}^{-2}$ ($\triangle$; blue); $18.0\,\mathrm{cm\,s}^{-2}$ ($\times$; red); and $22.1\,\mathrm{cm\,s}^{-2}$ ($\circ$; green). Vertical bars represent uncertainty in the toe velocity observations. Solid lines represent predictions based on Equation 4.1. Perforated lines represent Equation 4.3, and dashed lines represent the traditional energy balance solutions assuming a block flow (Equation 4.2). Data from Deardon, 2003.

Predictions of toe velocity were made by applying the experimental conditions of each run to Equations 4.1, 4.2, and 4.3, and the results were superimposed on Figures 4-1 − 4-4 as solid, dashed, and perforated curves, respectively. Note that only the momentum balance model and the linear velocity profile energy balance model predictions are presented in Figures 4-3 and 4-4 because they display better agreement with experimental observations than the block flow energy balance model, which confirms that the current interface in these high stem density runs were closer in shape to a linear profile than a block profile. As discussed in Chapter 2, Deardon (2003)'s observations suggest that predictions based on a linear velocity profile assumption will agree better with data from high a runs. In contrast, the predictions based on a block front are expected to have better agreement with data from runs with low or zero stem density. Figure 4-5 presents the percentage difference between Deardon (2003)'s experimental observations and predictions based on the linear velocity profile and block flow energy balance models. Only

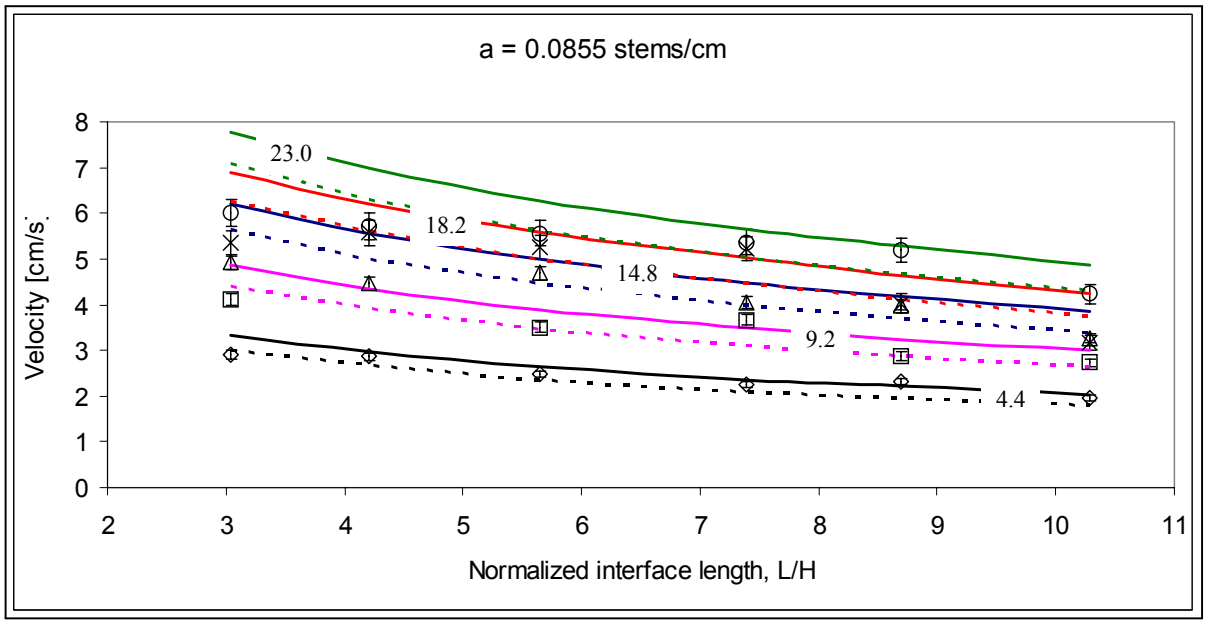

Figure 4-3: Toe velocity time series for runs with stem density $a = 0.0855\,\mathrm{cm}^{-1}$. Five runs with different density differences are presented: $g' = 4.4\,\mathrm{cm\,s}^{-2}$ ($\diamondsuit$; black); $9.2\,\mathrm{cm\,s}^{-2}$ ($\square$; pink); $14.8\,\mathrm{cm\,s}^{-2}$ ($\triangle$; blue); $18.2\,\mathrm{cm\,s}^{-2}$ ($\times$; red); and $23.0\,\mathrm{cm\,s}^{-2}$ ($\circ$; green). Vertical bars represent uncertainty in the toe velocity observations. Numerical labels on the solid lines represent g' [$\mathrm{cm\,s}^{-2}$]. Solid and perforated lines represent predictions based on Equations 4.1 and 4.3, respectively. Data obtained from Deardon, 2003.

the last observation in each run is plotted $\left(\frac{L}{H} \approx 10\right)$, because these measurements were least affected by the initial disturbance created by the removal of the partition.

For the highest stem density runs, the energy balance prediction assuming a linear velocity profile fits well with the observed data, with an average difference of -9% across the different g', as opposed to 33% average disagreement for the block flow energy balance model predictions. As a decreases from $a = 0.1497\,\mathrm{cm}^{-1}$, the discrepancy between the linear velocity profile model predictions and the observed data increases to -15% for $a = 0.0428\,\mathrm{cm}^{-1}$. In contrast, the average discrepancy for $a = 0.0428\,\mathrm{cm}^{-1}$ is 27% for the block flow model predictions. This trend may be attributed to a similar trend in the deviation of the flow shape from the ideal linear profile: as a approaches zero, the exchange flow shape approaches the traditional block shape that is well-documented in previous studies [Simpson, 1997]. For Deardon (2003)'s data, the toe velocity was more accurately described by the linear velocity profile energy balance

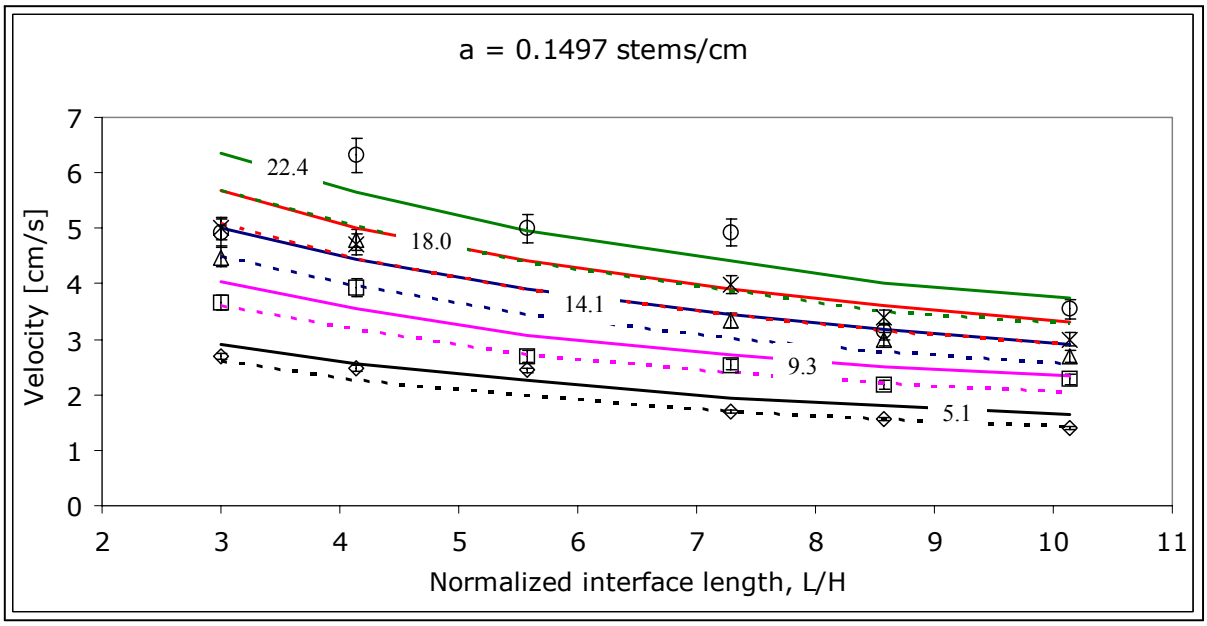

Figure 4-4: Toe velocity time series for runs with stem density $a = 0.1497\,\mathrm{cm}^{-1}$. Five runs with different density differences are presented: $g' = 5.1\,\mathrm{cm\,s}^{-2}$ ($\diamondsuit$; black); $9.3\,\mathrm{cm\,s}^{-2}$ ($\square$; pink); $14.1\,\mathrm{cm\,s}^{-2}$ ($\triangle$; blue); $18.0\,\mathrm{cm\,s}^{-2}$ ($\times$; red); and $22.4\,\mathrm{cm\,s}^{-2}$ ($\circ$; green). Vertical bars represent maximum uncertainty in the toe velocity observations for that run. Numerical labels on the solid lines represent g' [$\mathrm{cm\,s}^{-2}$]. Solid lines represent predictions based on the energy balance assuming a linear velocity profile (Equation 4.1). Perforated lines represent predictions by Equation 4.3. Data obtained from Deardon, 2003.

model than the block flow energy balance model for all $a > 0$ runs, with the exception of $g' = 18\,\mathrm{cm\,s}^{-2}$ runs through stem densities $a = 0.0428\,\mathrm{cm}^{-1}$ and $a = 0.0855\,\mathrm{cm}^{-1}$ (Figure 4-5). The cause of the poor agreement of the linear velocity profile model for these two experimental conditions were not identified.

In this context, the two energy balance models may be treated as two limits on the possible interface behavior, with exchange flows falling between the respective predictions under any condition. Recall from the discussion in Section 2.3 that the linear velocity profile energy balance model predictions are strictly greater than those by the block flow energy balance model. As displayed in Figure 4-5, with the exception of one run, the linear velocity profile energy balance model consistently overpredicts the toe velocity, which is consistent with this theory. In contrast, the block flow energy balance model consistently underpredicts the undercurrent

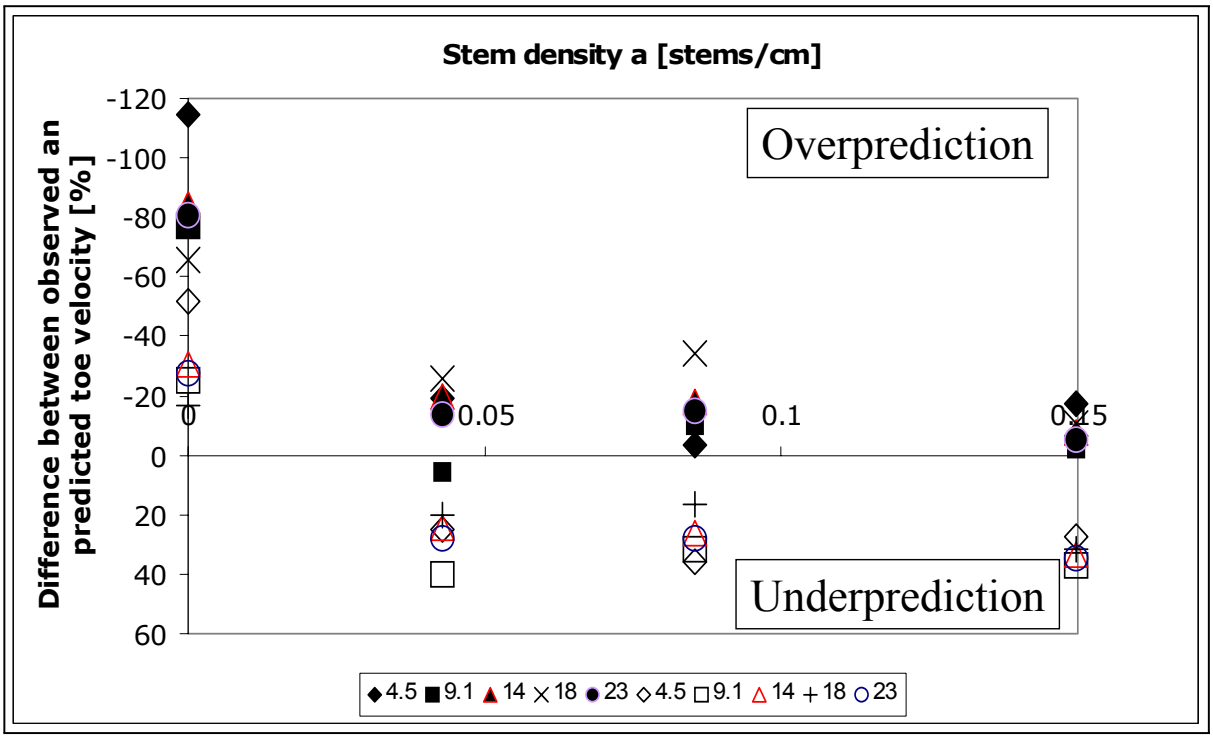

Figure 4-5: Difference between observed toe velocites and predictions based on the energy balance with the linear velocity profile assumption (Equation 4.1) and the block flow assumption (Equation 4.2). The discrepancy is calculated as the difference between the observation and prediction as a percentage of the observation. A positive and negative percentage indicates underprediction and overprediction, respectively. Each run is represented by a single data point at $\frac{L}{H} = 10.1 - 10.3$. The data point shapes represent different g' $\left[\mathrm{cm\,s^{-2}}\right]$, as indicated in the key. Solid markers and $\times$ represent predictions by Equation 4.1. Open markers and $+$ represent predictions by Equation 4.2. Data taken from Deardon, 2003.

propagation through stems, $a > 0$. For example, for $a = 0.0428\,\mathrm{cm}^{-1}$, the linear velocity profile energy balance and the momentum balance models both overpredict the toe velocities, while the block flow energy balance model underpredicts. Thus, the observed toe velocities fall in between the two energy balance predictions, as anticipated (Figure 4-2).

In addition, an overprediction may, to some extent, be a manifestation of unidentified sources of energy dissipation [Deardon, 2003] or an underestimated drag coefficient. Deardon (2003) attributes the overestimation in the $a = 0$ runs to turbulence. However, turbulence was not observed in higher stem density runs, which suggests that turbulence had little impact on these runs. While the C_D estimates have significant uncertainty at higher stem densities, the use

of drag coefficients for isolated cylinders can not be responsible for the overprediction of toe velocity. As discussed above, previous studies suggest that stem drag in an array is suppressed at $\mathrm{Re} \geqslant 200$ [Nepf, 1999] which, in Deardon (2003)'s experimental conditions, translates to a velocity of $u > 3\,\mathrm{cm\,s^{-1}}$. In this range, the use of drag coefficients for an isolated cylinder tends to overestimate the actual drag in the array, and therefore underpredict the toe velocity. Thus, inaccuracies in the drag coefficients used in the predictions contribute negatively to the overprediction for most of Deardon (2003)'s runs, suggesting that the actual overprediction may in fact be more significant.

The difference in the three velocity solutions complicates the behavior of exchange flows that transition between interface regimes during its propagation. All runs are theoretically inertial immediately after the partition is removed, as the density gradient is theoretically infinite at the instance of partition removal. While the flow is inertial, its toe velocity may be best described by the block flow equation (Equation 4.2). As the exchange flow propagates, the density gradient decreases and energy is dissipated through drag. Once the velocity has diminished such that the system enters the linear drag regime, a sufficiently vegetated flow is anticipated to approach a linear interface, at which point the toe velocity will behave according to the linear velocity profile model (Equation 4.1), which, for the same set of parameters, predicts higher velocities than the block flow model. Consequently, the transition from the block flow regime to the linear interface regime temporarily suppresses the decrease in toe velocity. (Note that the depth-averaged velocity of the advancing front – which reflects the energy of the system – decreases continuously, as required.) This delay makes the regime transition harder to identify from experimental observation. First, the period of velocity measurements must be able to resolve the regime transition. Second, sufficient measurements are required in both regimes to identify the transition point.

This transition from one regime to the other offers one possible explanation for the increase in velocity observed in Deardon (2003)'s data for the run $a = 0.0428\,\mathrm{cm^{-1}}$, $g' = 9.2\,\mathrm{cm\,s^{-2}}$ (Figure 4-6). At the beginning ($\frac{L}{H} \leqslant 4.2$) the observed toe velocities agreed within uncertainty with the block flow energy balance model predictions. As the exchange flow propagated, the toe velocity did not decrease as quickly as the block flow model predicts, and it deviated from the block flow predictions and approached the linear velocity profile energy balance model

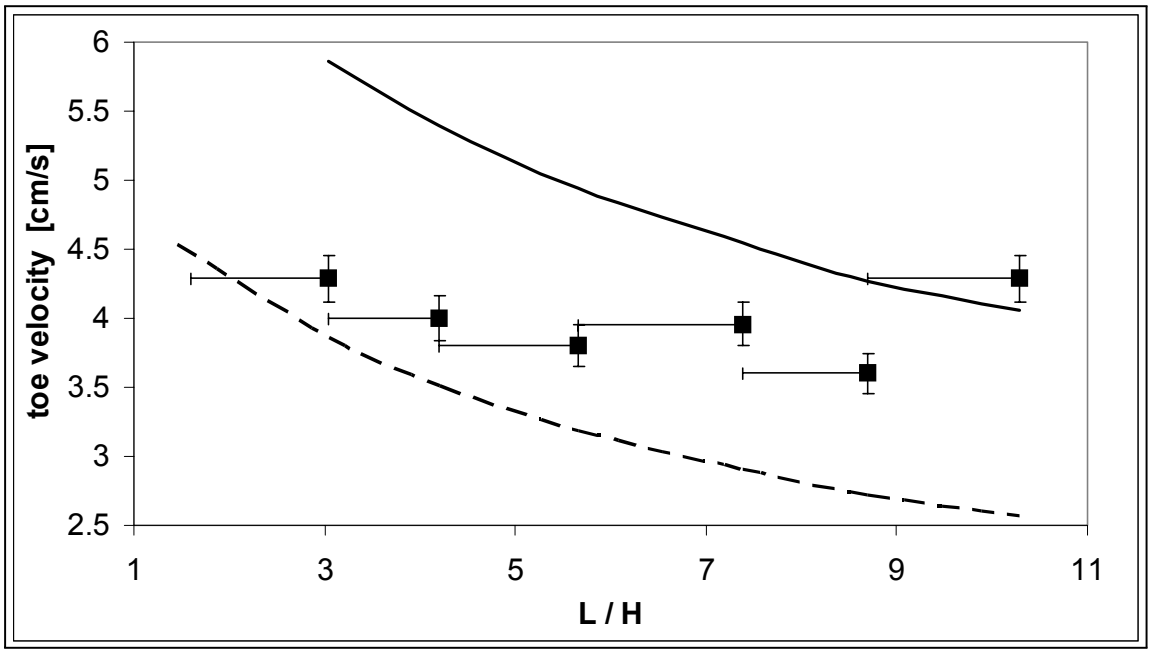

Figure 4-6: Toe velocity time series for Deardon (2003)'s run with $a = 0.0428\,\mathrm{cm}^{-1}$ and $g' = 9.2\,\mathrm{cm\,s}^{-2}$. Vertical bars represent uncertainty in the toe velocity observations. Horizontal bars represent the displacement over which the average velocity was calculated. Solid line represents predictions based on the energy balance assuming a linear velocity profile (Equation 4.1). Dashed line represents the traditional block flow energy balance predictions (Equation 4.2). Data from Deardon, 2003.

predictions. At $\frac{L}{H} = 10.3$, the toe velocity agrees with the linear velocity profile model within uncertainty.

4.2 Classification of Inertial and Non-inertial Flows based on the Variation in Toe Velocity

As discussed above, previous studies have observed that the toe velocity is independent of time in the absence of obstructions [Simpson, 1997], whereas it decreases with time in the presence of vegetation [Deardon, 2003]. In this section, the variation in toe velocity is examined quantitatively as a function of density difference and stem density, and a criterion is developed to categorize all flow conditions as inertial or non-inertial.

4.2.1 Formulation of a dimensionless velocity variation parameter

The fractional change in toe velocity during the time that the toe propagates from $x_1 = \frac{L_1}{2}$ to $x_2 = \frac{L_2}{2}$ is:

$$\frac{u_{toe}\left(\frac{L_1}{H}\right) - u_{toe}\left(\frac{L_2}{H}\right)}{u_{toe}\left(\frac{L_1}{H}\right)} \tag{4.4}$$

The substitution of the solution derived from the momentum balance (Equation 4.3) into this definition yields:

$$\frac{u_{toe}\left(\frac{L_1}{H}\right) - u_{toe}\left(\frac{L_2}{H}\right)}{u_{toe}\left(\frac{L_1}{H}\right)} = 1 - \sqrt{\frac{2 + C_D a L_1}{2 + C_D a L_2}} \tag{4.5}$$

Note that Equation 4.5 may be derived from the block flow energy balance solution (Equation 4.2) as well. However, the linear velocity profile energy balance solution (Equation 4.1) results in a slightly different expression: $\frac{u_{toe}\left(\frac{L_1}{H}\right) - u_{toe}\left(\frac{L_2}{H}\right)}{u_{toe}\left(\frac{L_1}{H}\right)} = 1 - \sqrt{\frac{8+3C_D a L_1}{8+3C_D a L_2}}$. The expression derived from the momentum balance solution is employed here for the analysis instead of that derived from the linear velocity profile energy balance solution, because the former describes the toe velocity evolution most accurately for ten out of the fifteen vegetated ($a > 0$) runs studied by Deardon (2003). Furthermore, this parameter is used to develop a criterion to identify the transition from inertial to drag-dominated flows. As such, the use of Equation 4.5, which satisfies both the block flow (inertial) model and the momentum model, is most appropriate.

Let us define a dimensionless parameter Δu characterizing the fractional toe velocity change as the difference in the velocities interpolated at $\frac{L_1}{H} = 3$ and $\frac{L_2}{H} = 10.5$ normalized by the velocity interpolated at $\frac{L_1}{H} = 3$:

$$\Delta u = \frac{u_{toe}\left(\frac{L}{H} = 3\right) - u_{toe}\left(\frac{L}{H} = 10.5\right)}{u_{toe}\left(\frac{L}{H} = 3\right)} \tag{4.6}$$

Then, according to Equation 4.5, Δu is a function of C_D, a, and H:

$$\Delta u = 1 - \sqrt{\frac{2 + 3C_D a H}{2 + 10.5 C_D a H}} \tag{4.7}$$

To calculate Δu from the experimental data, u_{toe} at $\frac{L}{H} = 3$ and $\frac{L}{H} = 10.5$ must first be extracted. Toe velocities are calculated from the images for each run as the displacement of the toe between two consecutive images that have an identifiable toe position divided by

the difference in time between the two images. This procedure is repeated for each run. $u_{toe}\left(\frac{L}{H}=3\right)$ and $u_{toe}\left(\frac{L}{H}=10.5\right)$ are interpolated from a linear regression performed on the toe velocity measurements and the averages of the $\frac{L}{H}$ of each pair of images between which the toe velocities were computed. Note that some experimental scenarios were repeated; for example, runs $42-44$ have a corresponding stem density and reduced gravity of $a = 0.064$ cm^{-1} and $g' = 18.3$ $\mathrm{cm\,s}^{-2}$. The toe velocity data from runs with identical a and m_{salt} such as these are computed for individual runs separately. Subsequently, when calculating Δu, the velocity data are combined and treated as if they were obtained from a single run by non-dimensionalizing the relevant parameters to account for the minor differences in H. Note that the data could not be adjusted to account for differences in g' that result from variations in the temperature between runs. However, Figure 3-5 identifies m_{salt} as the dominant factor in the differences in the density of the salt water between experimental runs. This suggests that differences in g' between runs with identical m_{salt} are negligible, and justifies the treatment of runs with the same a and m_{salt} as duplicate runs. Finally, the uncertainty in Δu is estimated as:

$$W_{\Delta u} \approx \sigma_u \left[\frac{1}{u_{toe}\left(\frac{L}{H}=3\right)} + \frac{1}{u_{toe}\left(\frac{L}{H}=10.5\right)}\right] \left|\frac{u_{toe}\left(\frac{L}{H}=10.5\right)}{u_{toe}\left(\frac{L}{H}=3\right)}\right| \tag{4.8}$$

where σ_u is the uncertainty in the observed toe velocities as estimated from the linear regression as defined by Equation 8.15 in Taylor, 1997.

4.2.2 High vegetative drag conditions

The theory predicts that where $C_D a L_1$ and $C_D a L_2$ are negligible ($C_D a L_1$, $C_D a L_2 \ll 2$), Δu approaches zero (Equation 4.5). Conversely, where $C_D a L_1$, $C_D a L_2 \gg 2$, and C_D is approximately the same between the two points, Δu approaches a constant $\Delta u = 1 - \sqrt{\frac{L_1}{L_2}}$ which is independent of a and g'.

Thus, drag is expected to become comparable to inertia when

$$a \approx \frac{2}{C_D L} \tag{4.9}$$

As discussed above, both the block flow energy balance model and the momentum balance model yield this relationship. This agreement between the two models emphasizes the validity

of Equation 4.9 as a criterion for the transition between inertia-dominated and drag-dominated regimes. Following the definition of Δu and taking $\frac{L}{H} \approx 3$, this condition is theoretically satisfied when $a \sim \frac{2}{C_D L_1} = \frac{2}{3 C_D H}$. C_D is generally on the order of 1, and the average water depth was $H \approx 13.5\,\mathrm{cm}$. Then, Equation 4.9 is satisfied when $a \simeq 0.05\,\mathrm{cm}^{-1}$. Thus, for runs with stem density $a > 0.05\,\mathrm{cm}^{-1}$, Equation 4.7 predicts that Δu approaches $\Delta u = 1 - \sqrt{\frac{L_1}{L_2}} = 0.47$.

Experimental observations are consistent with the theory. Δu for runs with $a = 0.0642\,\mathrm{cm}^{-1}$ and $a = 0.1155\,\mathrm{cm}^{-1}$ are illustrated in Figure 4-7. Linear regressions on these high stem density runs, presented as perforated lines in the figure, yield $\Delta u = 0.46 - 0.010 g'$ and $\Delta u = 0.48 - 0.00072 g'$, respectively, for $a = 0.0642\,\mathrm{cm}^{-1}$ and $a = 0.1155\,\mathrm{cm}^{-1}$ runs, with a correlation coefficient of $r = -0.25$ and $r = -0.10$. The 95% confidence interval for the slope of the linear regressions is -0.010 ± 0.07 and -0.00072 ± 0.008, respectively, which implies that the slope of both regressions is not significantly different from zero. This demonstrated lack of g'-dependence is consistent with Equation 4.7. Moreover, with the exception of two data points, the observed Δu equal the predicted value of $\Delta u = 0.47$ within uncertainty. The good agreement of the data with the theory demonstrates that these high stem density runs were drag-dominated.

4.2.3 Drag-dependence of the evolution of the toe velocity

Δu for each scenario is plotted in Figure 4-8 as a function of $C_D aL$, defined for all experimental scenarios from the present study and Deardon, 2003 at $\frac{L}{H} = 8$ where C_D is estimated by applying to Equation 2.36 the toe velocity interpolated at $\frac{L}{H} = 8$ using the results of the linear regressions on the observed velocities.

If a linear drag is assumed and the inertial term in Equation 2.31 is neglected, the momentum balance yields a toe velocity solution in terms of C':

$$u_{toe} = \frac{g' H}{C' aL} \tag{4.10}$$

Under these conditions, the predicted Δu is $\Delta u = 1 - \frac{L_1}{L_2} = 0.71$. This corresponds to the horizontal dash-dot line in Figure 4-8.

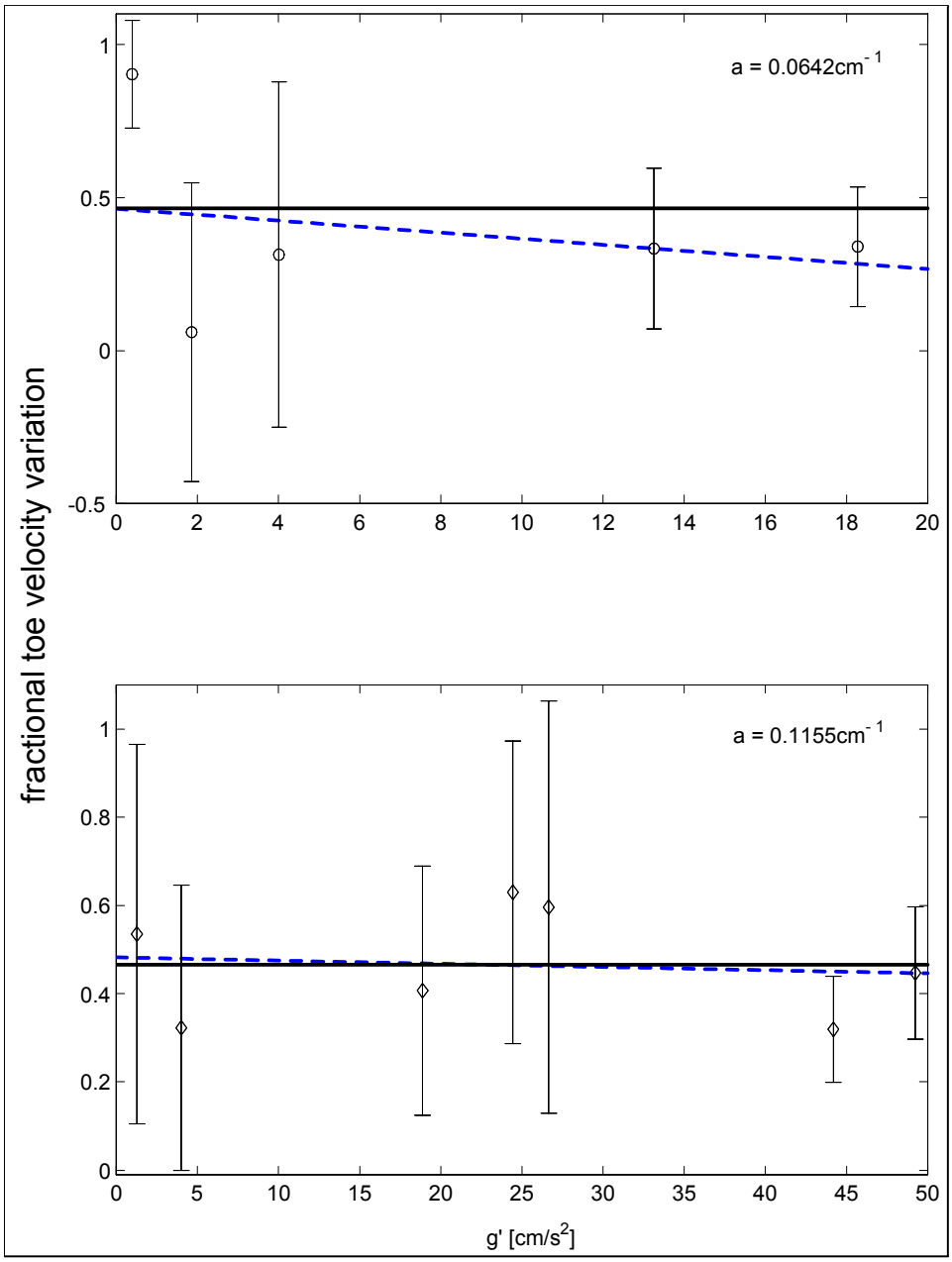

Figure 4-7: Fractional toe velocity difference (Δu) as a function of g' [$\mathrm{cm\,s^{-2}}$] for high stem density runs. Data for $a = 0.0642\,\mathrm{cm^{-1}}$ and $a = 0.1155\,\mathrm{cm^{-1}}$ are presented in the top and bottom plots, respectively. Toe velocity data from duplicate runs were combined before Δu were computed. Vertical bars represent the uncertainty associated with the linear regression from which Δu were computed ($\pm W_{\Delta u}$ as calculated in Equation 4.8). Run 17 is excluded from the bottom plot because it has an insufficient number of toe velocity data points. The perforated lines are linear regressions. The solid lines are $\Delta u = 0.47$.

The dashed curve represents the momentum balance prediction of Δu from Equation 4.7 based on the assumption that C_D is constant between $\frac{L}{H} = 3$ and $\frac{L}{H} = 10.5$. In comparing the data to this curve, it should be noted that where the toe velocity is decreasing, C_D at $\frac{L}{H} = 3$ would have been smaller than that at $\frac{L}{H} = 10.5$. As such, the assumption of constant C_D implicitly underestimates the true theoretical Δu. As an example, let us examine the scenario $a = 0.1155\,\mathrm{cm}^{-1}$ and $m_{salt} = 500\,\mathrm{g}$. The experimentally observed Δu and $C_D aL\left(\frac{L}{H} = 8\right)$ for this scenario is $\Delta u = 0.41$ and $C_D aL\left(\frac{L}{H} = 8\right) = 16.8$, respectively. Based on experimental observations, C_D at $\frac{L}{H} = 3$ and $\frac{L}{H} = 10.5$ were 1.25 and 1.35, respectively and, accordingly, the predicted Δu is $\Delta u = 0.43$. This is approximately 5% higher than the the prediction based on a constant C_D assumption derived by applying $C_D a = \frac{16.8}{8H}$ to Equation 4.7. However, the assumption of a constant C_D yields a difference in the predicted Δu of approximately 50% for the scenario $a = 0.0642\,\mathrm{cm}^{-1}$ and $m_{salt} = 10.00\,\mathrm{g}$. Thus, within uncertainty the data are consistent with the predictions.

The momentum balance prediction agrees reasonably well with the data. The theory captures the rapid increase in Δu under low drag conditions, which indicates that the presence of vegetation can dramatically affect the behavior of convective currents even at low densities. The deviation of Δu from the predicted values at low $C_D aL$ suggests that turbulence may be a significant dissipative mechanism at these $a \approx 0$.

Note the anomalous data point at $\Delta u = -0.05$, which corresponds to Deardon (2003)'s $a = 0.0428\,\mathrm{cm}^{-1}$, $g' = 9.2\,\mathrm{cm\,s}^{-2}$ run (Figure 4-6). As discussed in Section 4.1, an increase in velocity was observed for this run which is attributed to the flow having transitioned from the non-linear interface profile regime to the linear profile regime as it propagated. As a result, a linear regression on the toe velocity data and $\frac{L}{H}$ yields a line of best fit with a positive gradient and, accordingly, $\Delta u < 0$.

Hereafter, runs with $\Delta u < 25\%$ are defined as inertial runs; all other runs are classified as non-inertial (Table 4.2). Based on this criterion, all but one scenarios that have a corresponding $C_D aL\left(\frac{L}{H} = 8\right) < 5$ are classified as inertial.

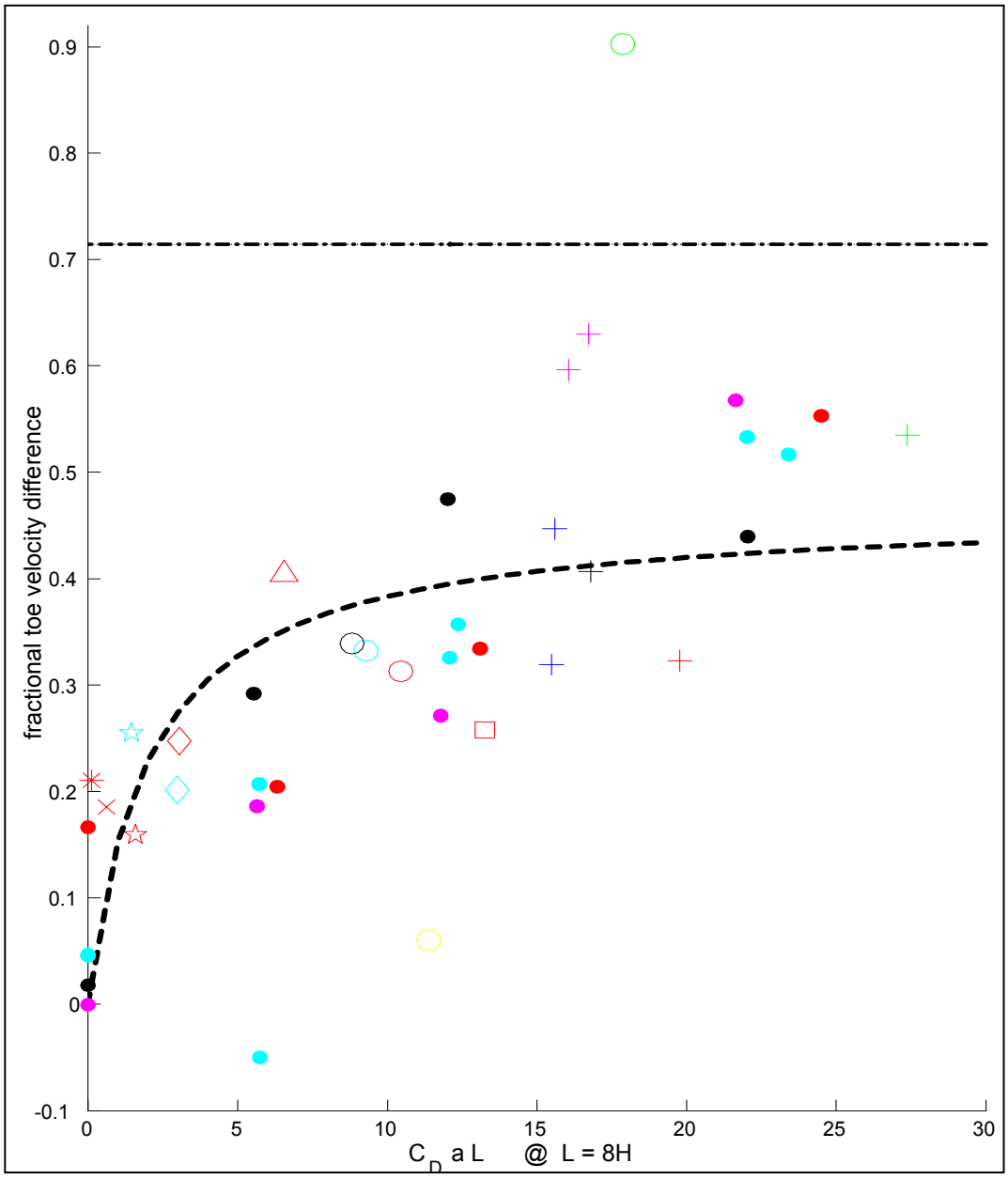

Figure 4-8: Fractional toe velocity difference (Δu) as a function of $C_D aL$ at $L = 8H$ ($= 8C_D aH$). Duplicate runs are combined. Dots indicate Deardon (2003)'s data. Key for present data summarized in Table 4.2. Horizontal dash-dot line represents $\Delta u = 1 - \frac{L_1}{L_2} = 0.71$. Perforated curve represents Equation 4.7, where $C_D aH = \frac{C_D aL}{8}$ given $L = 8H$ and C_D is assumed constant.

4.3 Classification of Linear and Non-linear Interface Regimes based on the Interface Gradient

In the previous section, a criterion was developed to classify flow conditions as either inertial or non-inertial. A run may also be categorized based on the shape of the interface. Here, a criterion is developed to classify all runs into these three categories based on the gradient of the interface: linear, non-linear, or transitional profile.

4.3.1 Theoretical analysis

The gradient of the interface may be predicted from the momentum balance model, which does not assume *a priori* an interface profile. The gradient of the interface at $x = 0$ is:

$$\frac{dz}{dx}|_{x=0} = \frac{dz}{du}\frac{du}{dx}|_{x=0} \tag{4.11}$$

Differentiation of Equation 2.21 yields:

$$\frac{du}{dz} = \frac{1}{2u}\frac{du^2}{dz} \tag{4.12}$$

$$= \frac{1}{2u}\frac{d}{dz}\left[\frac{2g^{'}}{2 + C_D aL}\left(\frac{H}{2} - z\right)\right] \tag{4.13}$$

$$= -\frac{g^{'}}{(2 + C_D aL)\, u} \tag{4.14}$$

As discussed in Section 2.2, the velocity at $x = 0$, $z = \frac{H}{2}$ is zero; the gradient of the velocity profile at this point is:

$$\frac{du}{dz}|_{x=0} = -\frac{g^{'}}{0} \tag{4.15}$$

Assuming $g' \neq 0$ (*i.e.*, that there is a finite horizontal density gradient), the slope of the interface is zero:

$$\frac{dz}{dx}|_{x=0} = -\frac{0}{g'}\frac{du}{dx}|_{x=0} = 0 \tag{4.16}$$

and the interface is horizontal at $x = 0$. Note that this calculation assumes that C_D is not a function of z, which implies that the velocity is also independent of z. This is the case in the idealized block flow regime, where velocity is vertically uniform in the undercurrent (Figure

2-1).

In contrast, if we assume $C_D \propto u^{-1}$, then Equation 4.12 becomes:

$$\frac{du}{dz} = \frac{1}{2}\frac{d}{dz}\left[-\frac{C^{'}aL}{2} + \sqrt{\left(\frac{C^{'}aL}{2}\right)^2 + 4g^{'}\left(\frac{H}{2} - z\right)}\right] \tag{4.17}$$

where $C^{'} = C_D u$. Evaluating this expression at $x = 0$, $z = \frac{H}{2}$ yields:

$$\frac{du}{dz}|_{z=\frac{H}{2}} = \frac{-2g^{'}}{C^{'}aL} \tag{4.18}$$

and the slope of the interface is:

$$\frac{dz}{dx}|_{x=0} = -\frac{C^{'}aL}{2g^{'}}\frac{du}{dx}|_{x=0} \tag{4.19}$$

Hence, in the linear drag regime, the slope of the interface is expected to be non-zero at $x = 0$, since $\frac{du}{dx}|_{x=0} \neq 0$ as long as the exchange flow is propagating.

In summary, the momentum balance predicts that the interface will have a non-zero slope at $x = 0$ in the linear drag regime, whereas flows that approach the idealized block flow profile have a horizontal interface. These differences allow for a quantitative method of distinguishing these flows.

4.3.2 Progression of the interface profile

Figure 4-9 displays the progression of the interface and highlights the differences in the interface shape that result from differences in the stem density and density differences. As stated previously, only the bottom half of the interface is presented because of the difficulty in distinguishing the interface where transparent fluid is propagating into dyed fluid. The interface subject to turbulent mixing (Figure 4-9 (a)) are particularly difficult to analyze. In addition, in Figure 4-9 (a) and (b), Benjamin (1968)'s solution for energy-conserving gravity currents are fitted to the leading edge of the experimental data.

Figure 4-9 (a) depicts a regime with sparse vegetation, and demonstrates that the interface at any given time is mostly horizontal at $z \approx 0.5H$. In contrast, near the leading edge of the

undercurrent, the interface bends sharply to the bed ($z = 0$) over approximately one water depth in the longitudinal direction, which creates the curved head. The head of the interface exhibits good agreement with Benjamin (1968)'s solution after $L \gtrsim 8$. Also, the horizontal profile immediately upstream of the head was maintained as the toe propagated. These observations are consistent with the weak time-dependence of the velocity profile predicted by the present theory and with observations reported for traditional, unobstructed lock-exchange flows (see Simpson, 1997 for a description), and characterize the inertia-dominated regime.

In Figure 4-9 (b), the general shape of the interface remains similar to the inertia-dominated regime, but the interface is now at a slight angle to the bed. Also, the height of the head – the depth over which the interface rapidly curves towards the bed – decreases slightly as the undercurrent propagates. This suggests that at large L, the head may become negligible in size and the interface may approach a linear profile. The differences between the regimes represented in Figures 4-9 (a) and (b) are highlighted by the poor agreement of the experimental data illustrated in (b) with Benjamin (1968)'s solution.

A similar decrease in the size of the head is observed in Figure 4-9 (c). However, contrary to the images (a) and (b), most of the interface displays a constant non-zero slope, and the head, while still identifiable, is much less prominent. Consequently, for the same interface length, the gradient at around $x \approx 0$ is greater in magnitude than in (a) and (b). The progression of the interface in this image clearly represents a linear profile regime. Note that one implication of a spatially uniform, non-zero slope is that the slope gradually decreases as the toe propagates and the interface elongates.

Finally, observe that the interface in each plot in Figure 4-9 rotates approximately about mid-depth, which is consistent with the present theory.

4.3.3 Progression of the interface slope

The slope of the interface in each image was estimated by performing a linear regression on the data points that fall within the range $1.25H - x_{toe} < x < x_{toe} - 1.25H$ for runs with a stem density of $a = 0.0642$ cm^{-1}, $a = 0.0855\,\text{cm}^{-1}$, or $a = 0.1155\,\text{cm}^{-1}$, and the range $0 < x < x_{toe} - 1.25H$ for the less densely vegetated runs. The respective ranges were selected to capture as much of the interface as possible to reduce the influence of anomalous data points

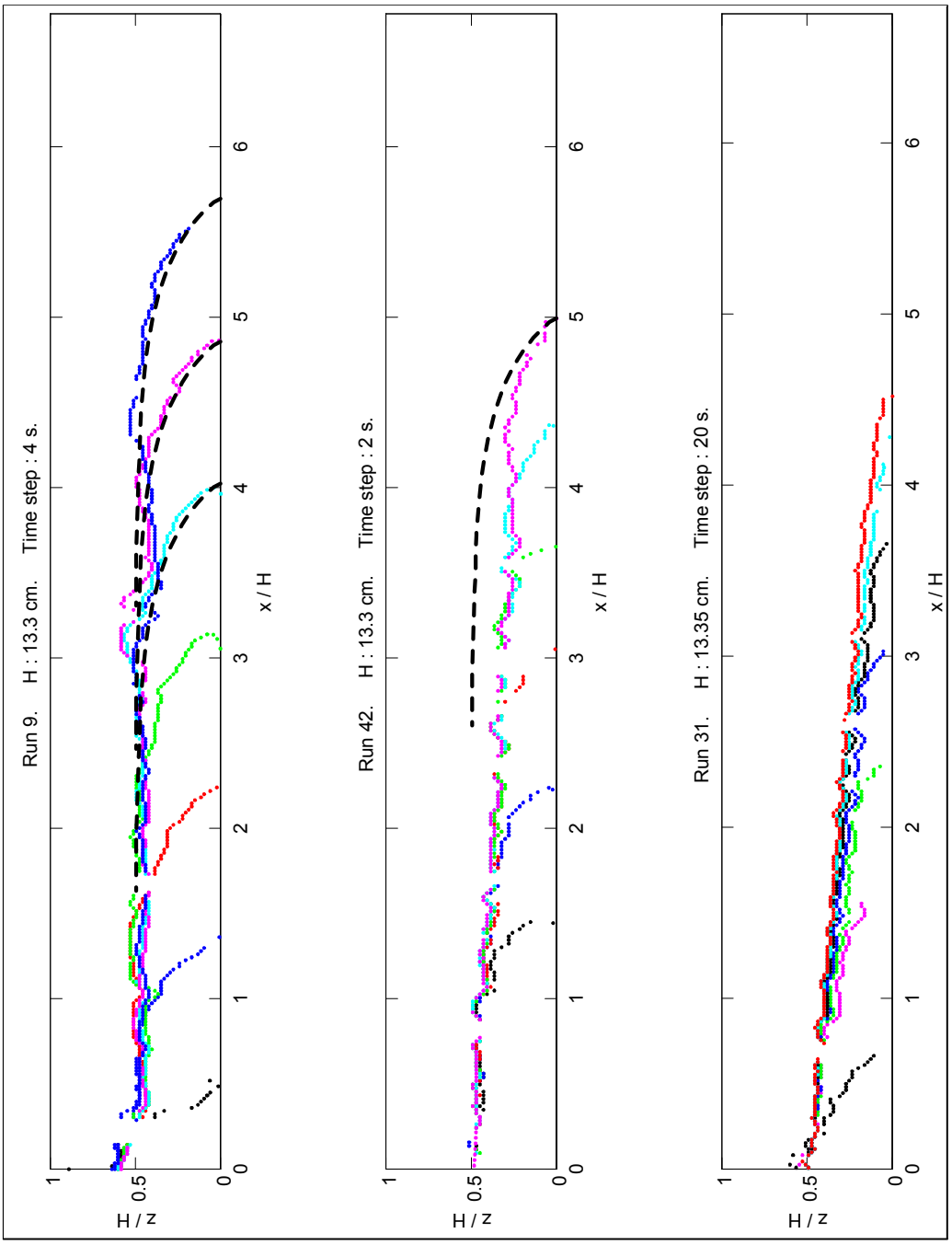

Figure 4-9: Progression of the interface with time. The profiles are separated by the period indicated at the top of each plot. The horizontal axes span $0 \leqslant x \leqslant \frac{L_{\text{tank}}}{2}$. (a) Run 9: $a = 0.01069\,\text{cm}^{-1}$ and $g' = 3.9\,\text{cm}\,\text{s}^{-2}$; (b) Run 42: $a = 0.0642\,\text{cm}^{-1}$ and $g' = 18.3\,\text{cm}\,\text{s}^{-2}$; (c) Run 31: $a = 0.0642\,\text{cm}^{-1}$ and $g' = 0.5\,\text{cm}\,\text{s}^{-2}$. Dashed curves represent Benjamin (1968)'s solution for energy-conserving gravity currents.

without capturing the head of the current at the free surface and the bed. The linear regression was restricted to the lower half of the interface, $x > 0$, for the less densely vegetated runs because of turbulence, which blurs the interface and makes it difficult to identify in the images. Furthermore, inertial runs tend to exhibit a jump at $x \approx 0$; the interface is horizontal on either sides of this jump at different depths (Figures C-8-C-10 and C-24). To prevent the turbulence and the jump from interfering with the estimate of the gradient, the linear regression was only applied to $x > 0$. Note that the linear regression on x_{toe} and time for run 35 were employed to calculate $\frac{L}{H}$ for replicate runs 33 and 34, for which toe data were not available. Only images where the extracted data points have a longitudinal spread greater than H and where some of those points fall within $x < H$ are analyzed, to insure that the data points represent the interface near $x = 0$ and to minimize the effects of anomalous points. Furthermore, only images where the toe is a minimum of H away from both $x = 0$ and the end of the tank are analyzed to minimize the influence of the initial disturbance and the end walls of the tank on the analysis. The uncertainty in the gradient of the regression is calculated according to the definition in Chapter 8 of Taylor, 1997.

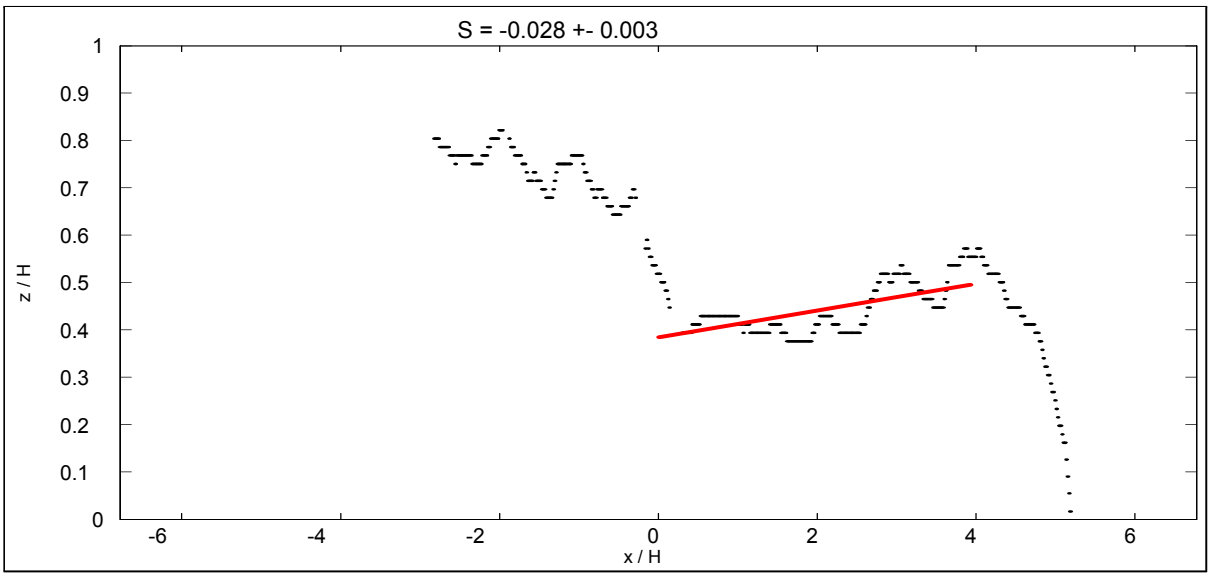

Figure 4-10: Example of a positive interface gradient. Run 11. Dots represent interface data points. Line indicates linear regression.

In the present study, positive gradients were extracted from runs 8, 9, 11, and 28, which

correspond to the lowest stem density conditions and, consequently, were identified as inertial runs according to the classification developed in Section 4.2. The cause of the positive gradients can be identified in the interface profiles for these runs (Figures C-8-C-10, and C-23) which show that the tallest part of the head interferes with the linear regression by providing data points at high z. Because these inertial runs have a mostly horizontal slope, as highlighted in Figure 4-9 and observable in Appendix C, the data points at the head are sufficient to yield a positive line of best-fit gradient (Figure 4-10). Because such positive gradient estimates are an artefact of the algorithm and do not accurately reflect the gradient of the interface around $x \approx 0$, positive $\frac{dz}{dx}$ measurements are plotted as $\frac{dz}{dx} = 0$ in Figure 4-11.

Figure 4-11 presents the progression of the interface slope at $x \approx 0$ for all runs. The negative of the gradient of the linear regression is plotted as the slope for that image, *i.e.*, a positive value on the plot represents a negative gradient. The idealized solution for the perfectly linear interface, $\frac{dz}{dx} = -\frac{H}{L}$, and the block flow, $\frac{dz}{dx} = 0$, provide an upper and lower limit for the gradient. Observe the significant spread of the gradient data for $L/H \lesssim 5.5$ and the high uncertainties associated with the individual data points in this range, which may be interpreted as a physical manifestation of the initial unsteadiness of the system.

Dimensionless slope parameter

For ease of analysis, a characteristic dimensionless parameter S is defined for each run as the average ratio of the gradient at $x \approx 0$ at $\frac{L}{H} = 8 \pm 1$ and the theoretical gradient for a perfectly linear interface at the same $\frac{L}{H}$:

$$S = \frac{\overline{\frac{dz}{dx}|_{x\approx 0, \frac{L}{H}\sim 8\pm 1}}}{-\frac{H}{L}} \tag{4.20}$$

For each run, all data points with an associated interface length in the range $7 < \frac{L}{H} < 9$ were extracted from Figure 4-11. (For runs 4, 8, and 23, which did not have data points in this range, the data point closest to this range at $\frac{L}{H} \geqslant 9$ were selected.) Each of the selected data points was normalized by the theoretical gradient for the perfectly linear interface corresponding to its $\frac{L}{H}$, as defined by Equation 4.20, and their average value is defined as the parameter S. A criterion is developed later that characterizes the shape of the interface based on S. Ultimately, the dependence of S on Re and stem drag are examined.

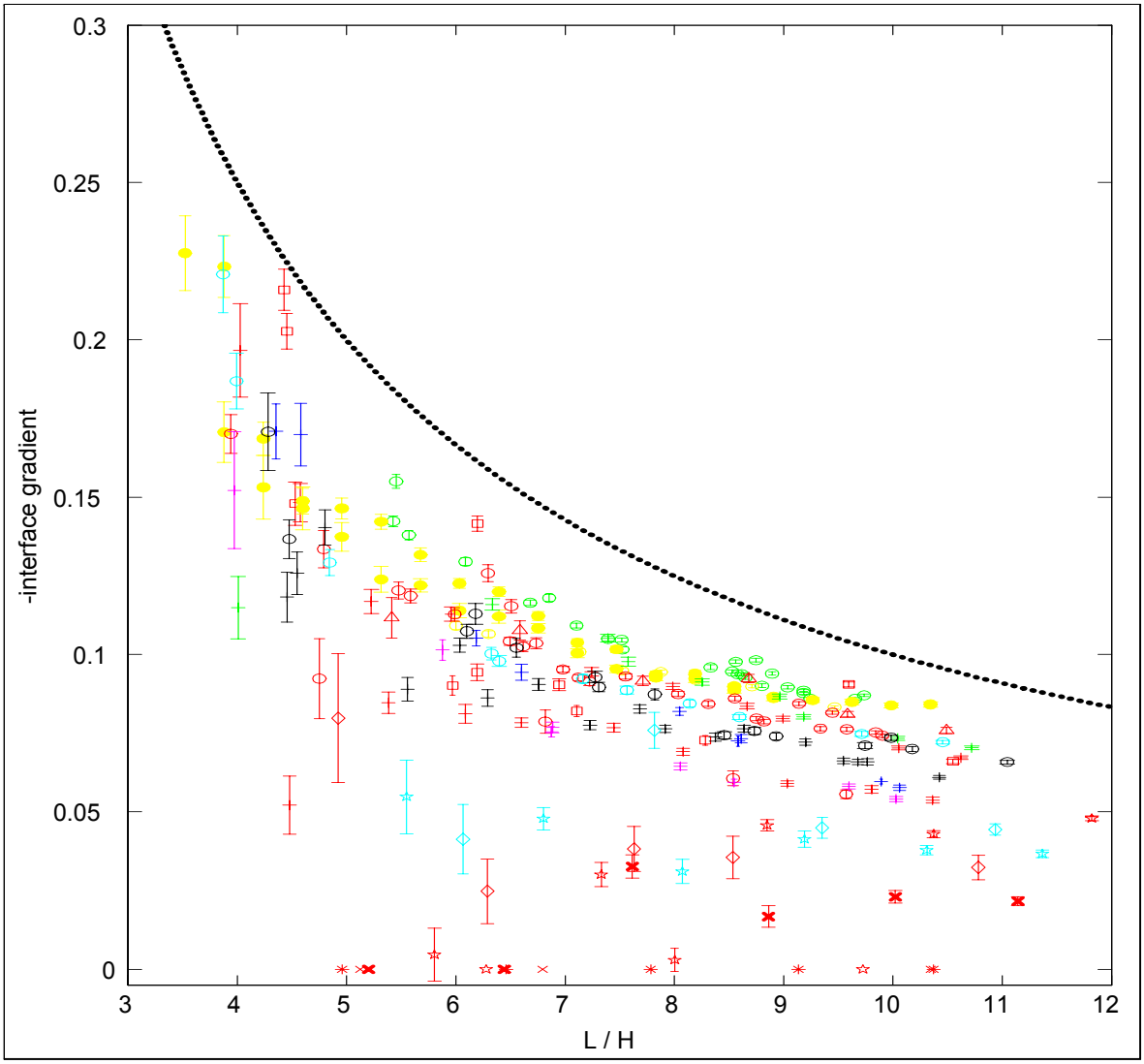

Figure 4-11: Progression of the gradient of the interface at $x \approx 0$. $\frac{L}{H}$-dependence of the negative of the gradient of the linear regression on the interface, $-\frac{dz}{dx}$. The sign of the gradient is reversed in this plot: a negative gradient, as defined by the present Cartesian system, is plotted as a positive data point. The black perforated line represents the theoretical progression of a perfectly linear interface: $-\frac{dz}{dx} = \frac{H}{L}$. The shape of the data points represents the stem density: $a = 0.1155$ cm^{-1} (+); $0.0855\,\text{cm}^{-1}$ ($\square$); $0.0642\,\text{cm}^{-1}$ ($\circ$); $0.0428\,\text{cm}^{-1}$ (Δ); $0.0214\,\text{cm}^{-1}$ ($\diamondsuit$); $0.01069\,\text{cm}^{-1}$ (pentagram); $0.00428\,\text{cm}^{-1}$ ($\times$); and $0.000855\,\text{cm}^{-1}$ (*), and their color the mass of salt added: $m_{salt} = 10.00$g (green); 50.00 g (yellow); 100.00 g (red); 190.00 g and 300.00 g (cyan); 500 g (black); 700.00 g (magenta); and ≥ 1000 g (blue). This information is summarized in Table 4.2. The vertical error bars represent the uncertainty in the gradient of the linear regression as defined by Taylor (1997). Note that positive interface gradients $\left(-\frac{dz}{dx} < 0\right)$ are plotted as $-\frac{dz}{dx} = 0$ without error bars.

Characteristic stem drag and Re

Two additional parameters were defined for each run: $C_D a L_8$ and Re_{toe8}, which characterize the stem drag and Re, respectively. To minimize the effect of anomalous x_{toe} measurements as well as the poor resolution of the toe velocity values obtained by measuring the rate of displacement between pairs of images attributable to the sparsity of measurements, the parameters were estimated by fitting a pre-selected mathematical expression to the toe position data from each run, differentiating with respect to time to obtain the corresponding expression for toe velocity, and finally interpolating the toe velocity at the appropriate $\frac{L}{H}$.

For runs that were classified as inertial (Table 4.2), Re_{toe8} is calculated from the velocity of the toe, estimated as the gradient of the linear regression on x_{toe} data extracted from the images. Note that Re_{toe8} for runs 33 and 34, for which toe positions are not available, are estimated from the toe velocity for their replicate, run 35, and treated as inertial runs.

For non-inertial runs, the process is more complicated. Neglecting the inertial term in the momentum balance and assuming linear drag yields the following relationship for x_{toe}:

$$\left(\frac{x_{toe}}{H}\right)^2 = \frac{g'}{C'aH}t \tag{4.21}$$

Because this function forces the toe position at $t = 0$ to be zero, the definition of $t = 0$ is critical.

It was observed during the experiments that a period on the order of a fraction of a second to a few seconds passed after the removal of the vertical partition before the density current began propagating. Since the mathematical formulation does not account for this initial behavior, $t = 0$ is redefined so that the data are consistent with the model. To define t_0, the effective zero time for non-inertial behavior, a linear regression is performed on $\left(\frac{x_{toe}}{H}\right)^2$ and t for each run:

$$\left(\frac{x_{toe}}{H}\right)^2 = A + Bt \tag{4.22}$$

where A and B are the fitted constants. From this regression, the correction time, t_0, is:

$$t_0 = -\frac{A}{B} \tag{4.23}$$

It should be noted that this regression assumes that $x_{toe} \propto \sqrt{t - t_0}$; the transformation of t to $t - t_0$ tends to shift the measurements to improve their agreement with this t-dependence.

Next, a power function is fitted to the x_{toe} data:

$$\log\left(\frac{x_{toe}}{H}\right) = C + D\log\left(t - t_0\right) \tag{4.24}$$

which is equivalent to:

$$\frac{x_{toe}}{H} = 10^C\left(t - t_0\right)^D \tag{4.25}$$

and a function for toe velocity is estimated by differentiating this fitted function with respect to time:

$$\begin{aligned} u_{toe} &= H\frac{d}{dt}\frac{x_{toe}}{H} && (4.26)\\ &= 10^C HD\left(t - t_0\right)^{D-1} && (4.27)\\ &= 10^C HD\left(\frac{1}{2\times 10^C}\frac{L}{H}\right)^{\frac{D-1}{D}} && (4.28) \end{aligned}$$

where C and D are the fitted constants. The expression is evaluated at each $\frac{L}{H}$ corresponding to a relevant data point – *i.e.*, $7 < \frac{L}{H} < 9$ for all runs except runs 4, 8, and 23, as discussed previously. Then, the result is averaged to determine the characteristic $\mathrm{Re}_{toe8} = \overline{u_{toe_8}}\frac{d}{\nu}$ for that run. $\mathrm{C}_D aL_8$ values are then determined by applying the toe velocity estimates to White (1974)'s equation to obtain the corresponding C_D, then multiplying those estimates with the corresponding a and L. The resulting values for $\mathrm{C}_D aL$ are then averaged to obtain a single value for each run, $\mathrm{C}_D aL_8$.

Sensitivity of the interpolated toe velocity to the effective zero-time The definition of the correction term t_0 in the aforestated calculation of Re_{toe8} and $\mathrm{C}_D aL_8$ tends to redefine the data to fit the momentum balance and the linear drag relationship. The sensitivity of the interpolated toe velocity, hence Re_{toe8} and $\mathrm{C}_D aL_8$, to t_0 may be described by the fractional difference in the interpolated toe velocity that results when t_0 is halved,

$$u_{toe_0} = 10^{C_0} HD_0\left(\frac{1}{2\times 10^{C_0}}\frac{L}{H}\right)^{\frac{D_0-1}{D_0}} \tag{4.29}$$

Then, the fractional difference is:

$$\frac{u_{toe} - u_{toe_0}}{u_{toe}} = 1 - \frac{u_{toe_0}}{u_{toe}} \tag{4.30}$$

$$= 1 - 10^{(C_0 - C)} \frac{D_0}{D} \left(\frac{L}{H}\right)^{\left(\frac{1}{D} - \frac{1}{D_0}\right)} \frac{\left(2 \times 10^{C}\right)^{\left(1 - \frac{1}{D}\right)}}{\left(2 \times 10^{C_0}\right)^{\left(1 - \frac{1}{D_0}\right)}} \tag{4.31}$$

The fractional differences were evaluated at $\frac{L}{H} = 8$ for each run designated as non-inertial. The difference ranged from -27% to 5%, with an average of -6%. Of the twenty eight non-inertial runs, only six have an associated fractional difference greater than 10% in magnitude, $\left|\frac{u_{toe} - u_{toe_0}}{u_{toe}}\right| > 0.1$. These results suggest that the interpolated toe velocities do not exhibit strong sensitivity to the definition of t_0. Moreover, the actual values of t_0 varies from $-0.2 \pm 2\,\mathrm{s}$ to $7.5 \pm 1\,\mathrm{s}$, which are comparable to the inverse frame rate for image acquisition, which ranged from $2\,\mathrm{s}$ per frame to $10\,\mathrm{s}$ per frame (Table 4.1). Thus, the use of the characteristic Re_{toe8} and $\mathrm{C}_D a L_8$ to represent the present experimental data is justified.

Figure 4-12 illustrates that Equation 4.21, which is associated with the assumptions of linear drag and negligible inertia, agrees well with runs in the linear interface regime (Figure 4-12 (c)). However, for runs that are not fully in the linear interface regime Equation 4.21 overpredicts the toe velocity, and thus the toe position. The overprediction is due to the neglect of the inertia term which is still significant in the transitional regime.

It is interesting to note that Hatcher *et al.* (2000) developed similarity solutions for turbulent gravity currents through an array of obstacles by assuming $\frac{\partial u}{\partial t} + u\frac{\partial u}{\partial x}$ to be negligible compared to the array drag and the buoyancy forcing. Their solutions also describe the toe velocity as $u(z = 0) \sim t^{-1/2}$. However, this t-dependence is predicted only in the case where the volume of the gravity current is constant with time, which is not applicable to our experiments or model formulation.

Figures 4-13 and 4-14 plot the normalized interface gradient S (Equation 4.20) against $\mathrm{C}_D a L_8$ and Re_{toe8}, respectively. Recall that negative S data points are plotted as $S = 0$ in the figures. As anticipated, S approaches 1 as $\mathrm{C}_D a L_8$ increases (Figure 4-13), demonstrating that the interface approaches a linear interface as the stem drag increases. The interface also exhibits a Re-dependence (Figure 4-14). As anticipated, for a given stem density a, S

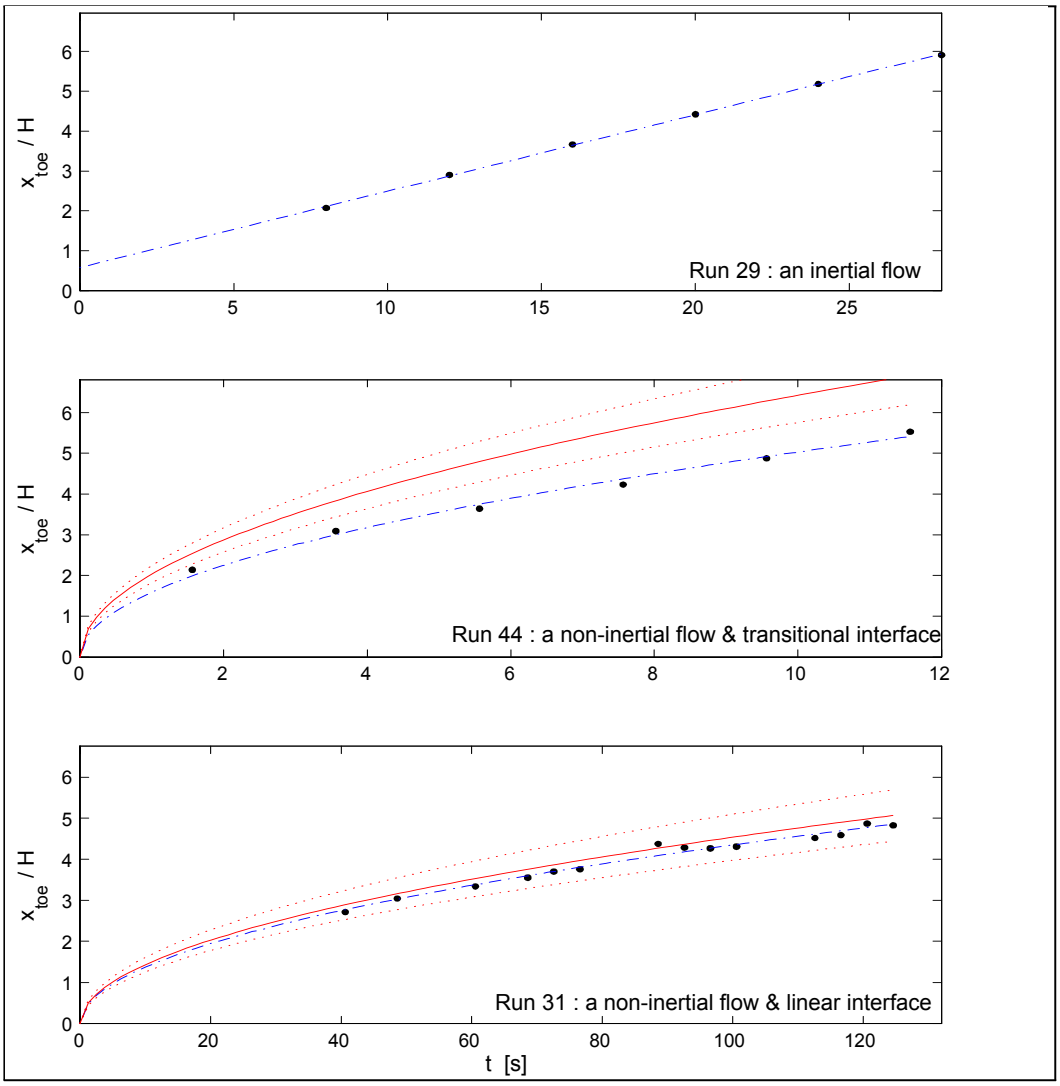

Figure 4-12: Evolution of the toe with time in the three regimes: (a) inertial flow (run 29); (b) non-inertial flow and transient interface (run 44); and (c) non-inertial and linear interface regimes (run 31), according to the classification criteria developed in this chapter. Non-dimensionalized toe position is plotted against time. The dash-dot line is the best-fit line in the least squares sense for (a): $\frac{xtoe}{H} = A + Bt$ where A and B are the fitted constants. For (b) and (c), the x-axis is the corrected time, $t - t_0$, and the dash-dot lines represent $\frac{x_{toe}}{H} = \sqrt{B(t-t_0)}$, where $t_0 = -\frac{A}{B}$, as calculated from the linear regression Equation 4.22, where A and B are fitted constants. $t_0 = 0.44 \pm 0.4\,\mathrm{s}$ and $t_0 = 7.4 \pm 5\,\mathrm{s}$ for runs 44 (b) and 31 (c), respectively. The solid lines are $\frac{x_{toe}}{H} = \sqrt{\frac{g'(t-t_0)}{C'aH}}$ and the perforated lines reflect ± 1 standard deviation in C' estimates calculated for each run from the momentum balance in Section 4.5: $C' = 5.2 \pm 1\,\mathrm{cm\,s^{-1}}$ and $2.8 \pm 0.7\,\mathrm{cm\,s^{-1}}$ for (b) and (c), respectively.

progressively decreases as Re_{toe8} increases. This trend reflects the deviation from the idealized perfectly linear interface shape as inertia becomes increasingly significant. For the ease of discussion, runs with $S > 0.70$ and $S < 0.30$ are classified as having a linear and a non-linear interface, respectively. Runs with $0.30 \leqslant S \leqslant 0.70$ are classified as being in the transitional regime. Observe that runs with $a < 0.02\,\mathrm{cm}^{-1}$ ($\mathrm{C}_D a L_8 < 2$ in Figure 4-13) appear to not have sufficient drag to reach the linear interface regime, regardless of Re_{toe8}. In contrast, runs with $a > 0.04\,\mathrm{cm}^{-1}$ exhibited Re_{toe8}-dependence such that a linear interface profile was observed for at least one run for each a tested in the laboratory. Note that in each a for which a linear interface is observed, the highest Re_{toe8} at which $S > 0.70$ is in the range $45 < \mathrm{Re}_{toe8} < 100$. It is possible that the critical Re_{toe8} at which $S = 0.7$ is a-sensitive, but there is insufficient data to assess this. There is also insufficient data to comment on whether a linear interface can be achieved in $a = 0.0214\,\mathrm{cm}^{-1}$ conditions. To highlight these trends, the eight runs with $a < 0.04\,\mathrm{cm}^{-1}$, $\mathrm{C}_D a L_8 < 5$ are depicted with dots in Figure 4-14.

4.3.4 Images for a progression of stem densities and density gradients

Figures 4-15 and 4-16 depict the interface profile for a progression of stem densities with $\mathrm{m}_{salt} = 100.00\,\mathrm{g}$ and a progression of density differences with $a = 0.0642\,\mathrm{cm}^{-1}$, respectively. As discussed previously, only the lower half of the interface $\left(i.e., 0 \leqslant z \leqslant \frac{H}{2}\right)$ will be examined.

The a-dependence in the interface profile is clearly observable in Figure 4-15. At low stem densities (Figure 4-15 (a) - (c)), the interface is predominantly horizontal, with uniform depth of undercurrent behind the head, *i.e.*, $\frac{dz}{dx} = 0$. These stem densities are also characterized by turbulence. Also, an elevated nose at the toe of the undercurrent can be seen in images (b) and (c). These characteristics are consistent with well-documented observations from previous works on unobstructed gravity currents. Images (d) and (e) of Figure 4-15 depict a transitional stage between the block flow regime and the linear interface regime. The head is still visible, but the rest of the interface has a spatially uniform non-zero slope. At even higher stem densities (images (f) and (g)), the head is smaller, and thus, most of the interface appears linear.

This sequence of images highlights the complexity of the system. The interface changes

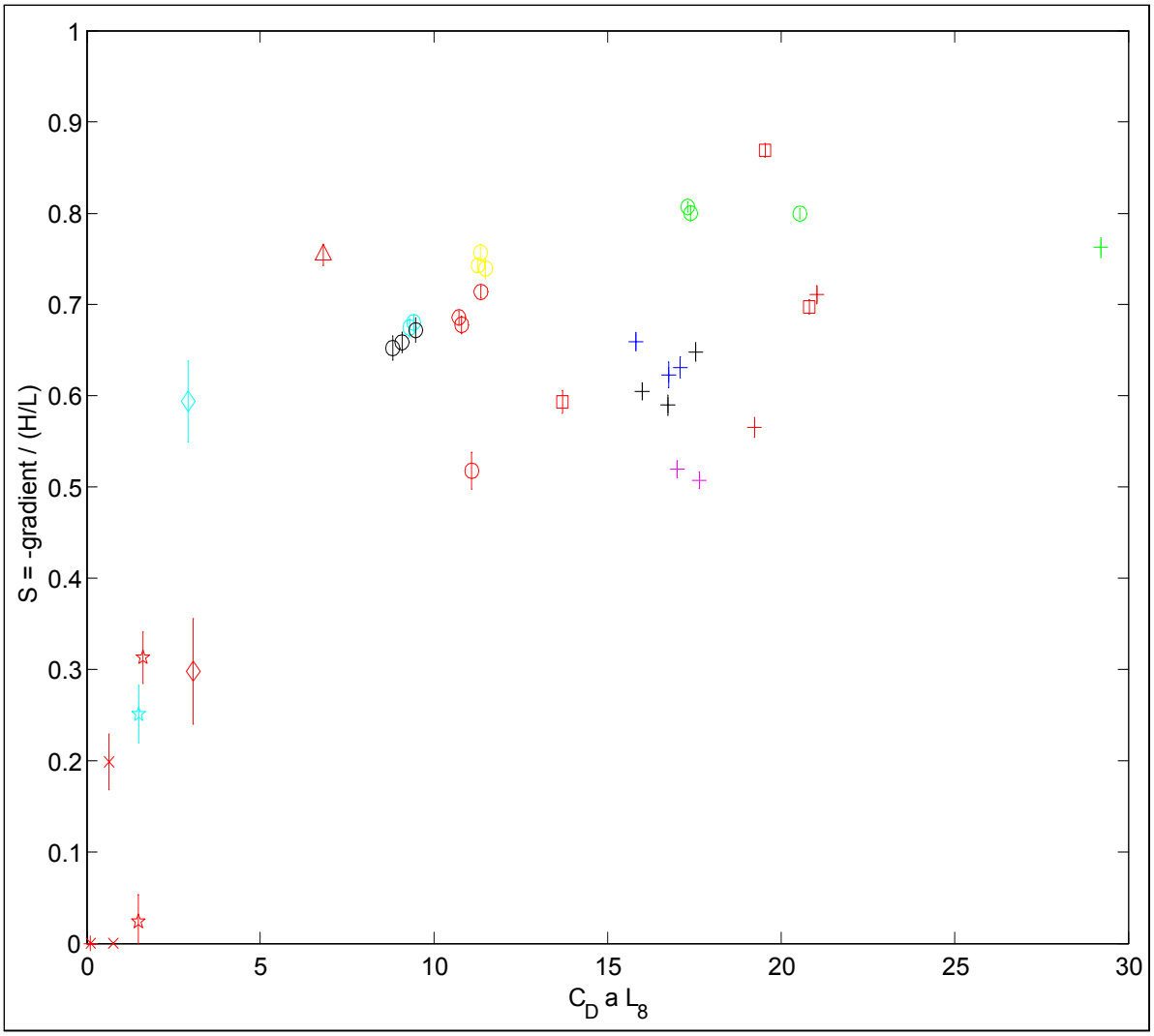

Figure 4-13: Normalized interface slope S and $C_D a L_8$ for each run. All runs presented: each run is identified by their $C_D a L_8$. The shape of the data points represents the stem density: $a = 0.1155\,\mathrm{cm}^{-1}$ (+); $0.0855\,\mathrm{cm}^{-1}$ (□); $0.0642\,\mathrm{cm}^{-1}$ (○); $0.0428\,\mathrm{cm}^{-1}$ (Δ); $0.0214\,\mathrm{cm}^{-1}$ (◇); $0.01069\,\mathrm{cm}^{-1}$ (pentagram); $0.00428\,\mathrm{cm}^{-1}$ (×); and $0.000855\,\mathrm{cm}^{-1}$ (*). The color of the data point represents the mass of salt added: $m_{salt} = 10.00\,\mathrm{g}$ (green); 50.00 g (yellow); 100.00 g (red); 190.00 g and 300.00 g (cyan); 500 g (black); 700.00 g (magenta); and $\geqslant 1000\,\mathrm{g}$ (blue). Solid line represents the slope of the perfectly linear interface: $S = 1$. The vertical bars represent twice the uncertainty in the gradient of the linear regression on the interface. Note: Measured S for runs 8 and 11 are negative ($S = -0.26 \pm 0.02$ and -0.19 ± 0.04, respectively). These data points are set to zero and the error bars are removed.

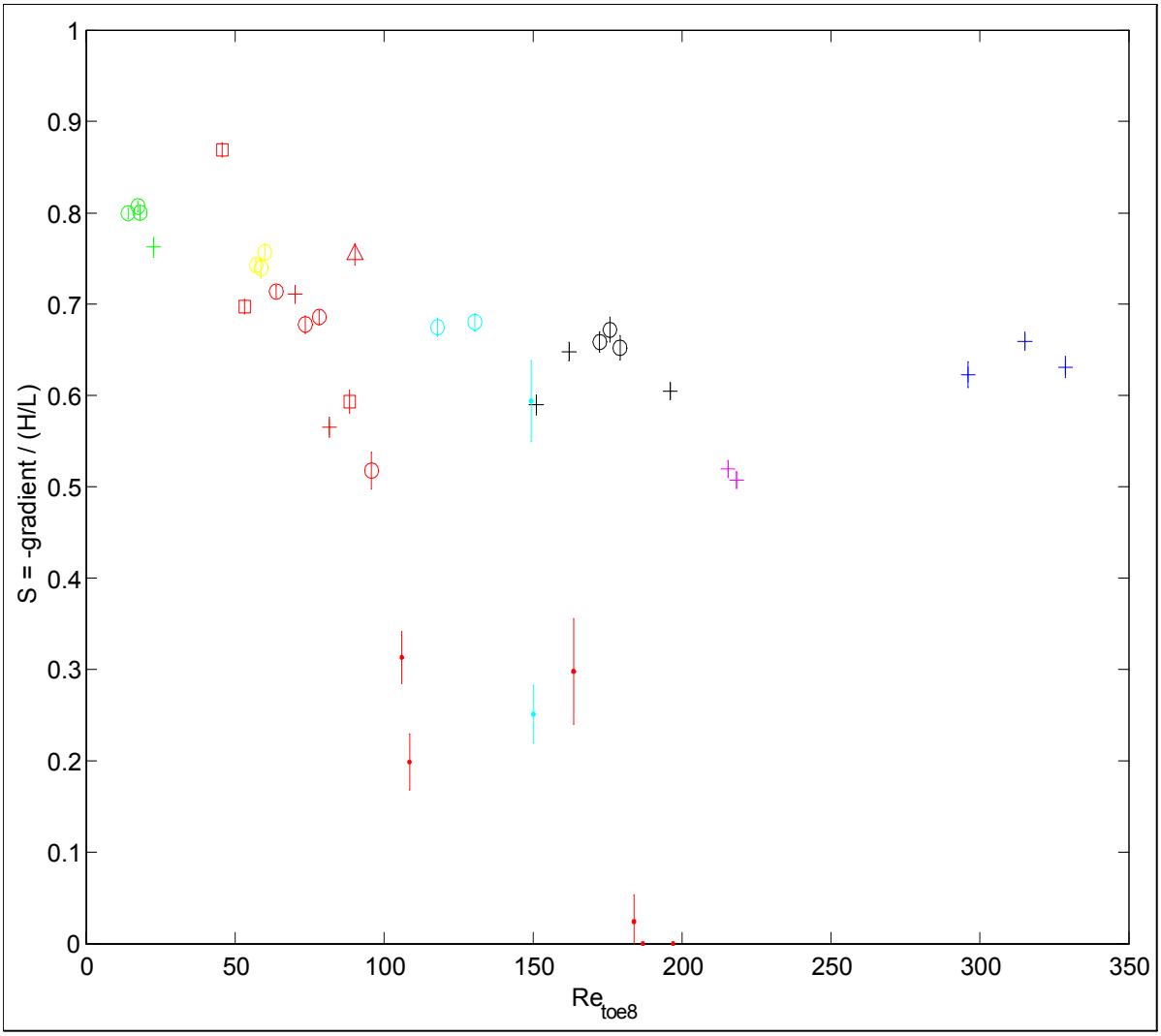

Figure 4-14: Normalized interface slope S as a function of Re_{toe8} for each run. The shape of the data points represents the stem density: $a = 0.1155\,\mathrm{cm}^{-1}$ (+); $0.0855\,\mathrm{cm}^{-1}$ (□); $0.0642\,\mathrm{cm}^{-1}$ (○); $0.0428\,\mathrm{cm}^{-1}$ (Δ); $0.0214\,\mathrm{cm}^{-1}$ (◇); $0.01069\,\mathrm{cm}^{-1}$ (pentagram); $0.00428\,\mathrm{cm}^{-1}$ (×); and $0.000855\,\mathrm{cm}^{-1}$ (*), with the exception of the eight runs for which $\mathrm{C}_D a L_8 < 5$, which are denoted by dots. The color of the data point represents the mass of salt added: $\mathrm{m}_{salt} = 10.00\,\mathrm{g}$ (green); $50.00\,\mathrm{g}$ (yellow); $100.00\,\mathrm{g}$ (red); $190.00\,\mathrm{g}$ and $300.00\,\mathrm{g}$ (cyan); $500\,\mathrm{g}$ (black); $700.00\,\mathrm{g}$ (magenta); and $\geqslant 1000\,\mathrm{g}$ (blue). Note: Measured S for runs 8 and 11 are negative ($S = -0.26 \pm 0.02$ and -0.19 ± 0.04, respectively). These data points are set to zero and the error bars are removed.

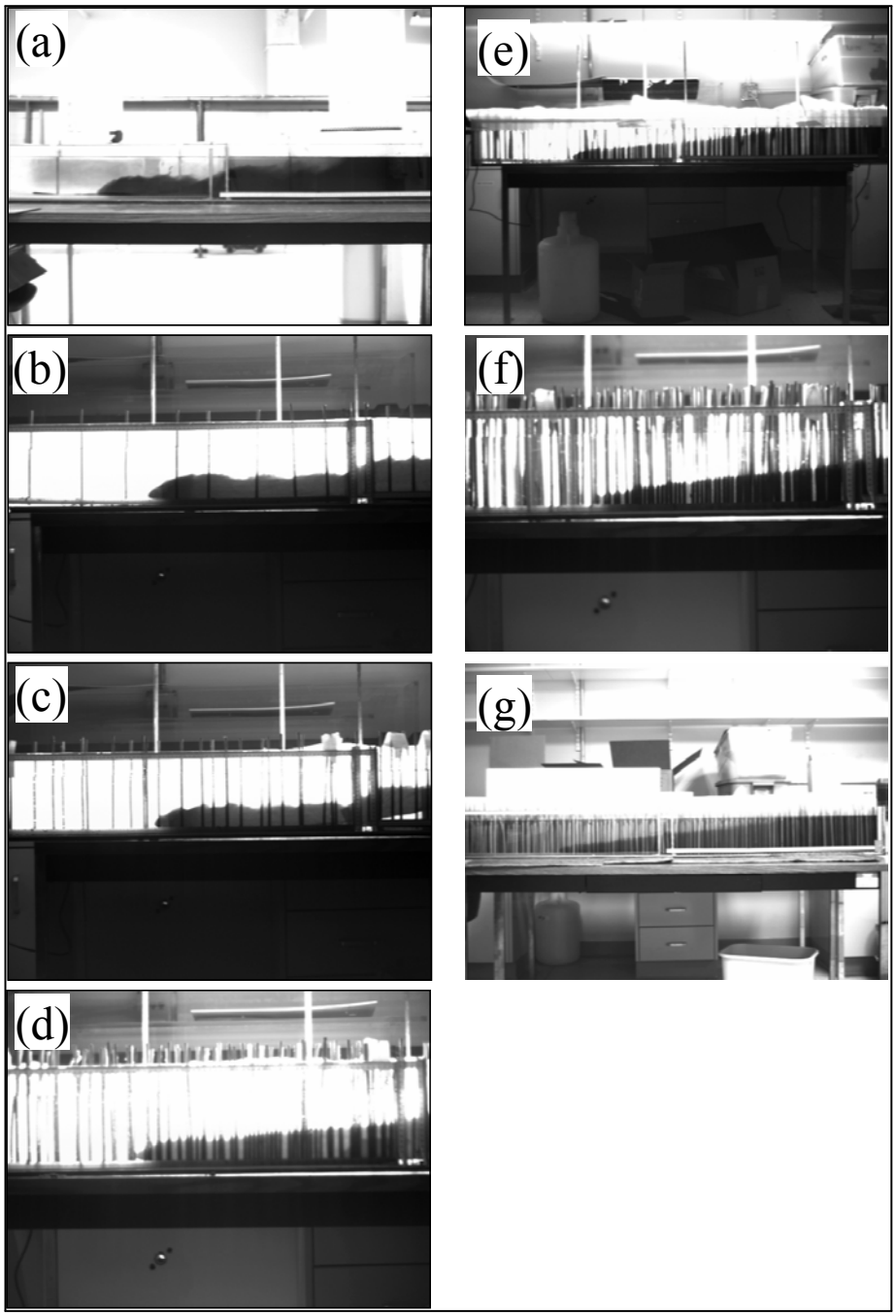

Figure 4-15: Variations in the interface profile for a progression of stem densities with $m_{salt} = 100.00\,g$. (a) Run 11: $a = 0.000855\,cm^{-1}$; (b) Run 28: $a = 0.00428\,cm^{-1}$; (c) Run 29: $a = 0.01069\,cm^{-1}$; (d) Run 21: $a = 0.0428\,cm^{-1}$; (e) Run 38: $a = 0.0642\,cm^{-1}$; (f) Run 23: $a = 0.0855\,cm^{-1}$; (g) Run 7: $a = 0.1155\,cm^{-1}$. Images (b), (c), (d), and (f) only captured the bottom half of the interface, whereas the other images captured the entire length of the interface.

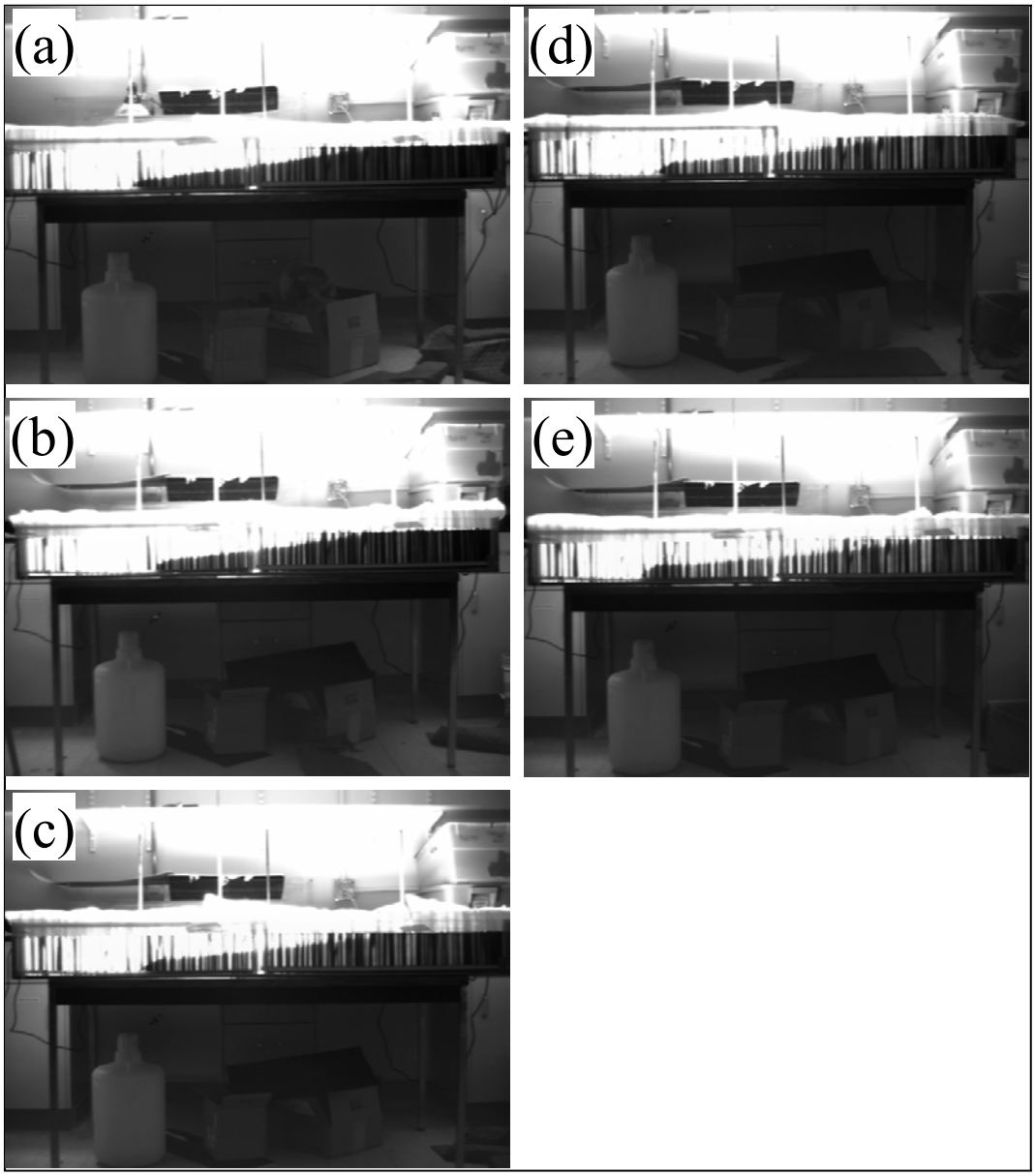

Figure 4-16: Variations in the interface profile for a progression of density differences with $a = 0.0642\,\mathrm{cm}^{-1}$: (a) Run 32: $g' = 0.5 \pm 0.5\,\mathrm{cm\,s}^{-2}$; (b) Run 35: $g' = 1.9 \pm 0.5\,\mathrm{cm\,s}^{-2}$; (c) Run 38: $g' = 4.0 \pm 0.5\,\mathrm{cm\,s}^{-2}$; (d) Run 40: $g' = 13.3 \pm 0.5\,\mathrm{cm\,s}^{-2}$; (e) Run 44: $g' = 18.3 \pm 0.5\,\mathrm{cm\,s}^{-2}$.

its shape continuously as stem density varies, making the definition of regimes based on the interface profile difficult. The transition from a non-linear (block) interface to a linear interface appears to occur around $a = 0.04 - 0.07\,\mathrm{cm}^{-1}$ at this density difference, which agrees well with Deardon (2003)'s observations.

A similar but reverse progression in the size of the head is visible in Figure 4-16, which presents runs with constant a and a progression of density differences: the head appears larger at higher g'. However, no turbulence is visible at this stem density in the range of density differences tested. Moreover, the interface, with the exception of the head, appears to have a spatially uniform non-zero slope in all of the cases, which is consistent with the calculated S values (Figure 4-14), confirming the appropriateness of the definition of S and its use as a characteristic parameter for the interface profile.

Note that, contrary to our theoretical models, the interface does not appear to be strictly symmetric about $x = 0$. The height of the head at the bed appears to be consistently greater than that of the head at the free surface where the interface bends towards the free surface. Unfortunately, the poor vertical resolution in the present set of images prevents quantitative analysis of the differences. The apparent asymmetry may be attributed to the fact that the bed is a no-slip boundary unlike the free surface, a condition that was not incorporated into the present model. In addition, as mentioned previously, the difference between the dark undercurrent propagating into transparent water and the transparent surface return flow propagating into dark fluid may create a false sense of asymmetry. Entrainment of ambient water into the undercurrent does not interfere with the appearance of the interface in the images because the entrained fluid is not visible through the dyed fluid. In contrast, ambient dyed fluid that is entrained into the transparent surface return flow remains visible as dyed patches of fluid and, as a result, the interface may appear to shift toward $x = 0$ near the free surface, $z > \frac{H}{2}$. These factors are likely to have contributed to the apparent asymmetry of the interface profile in the images.

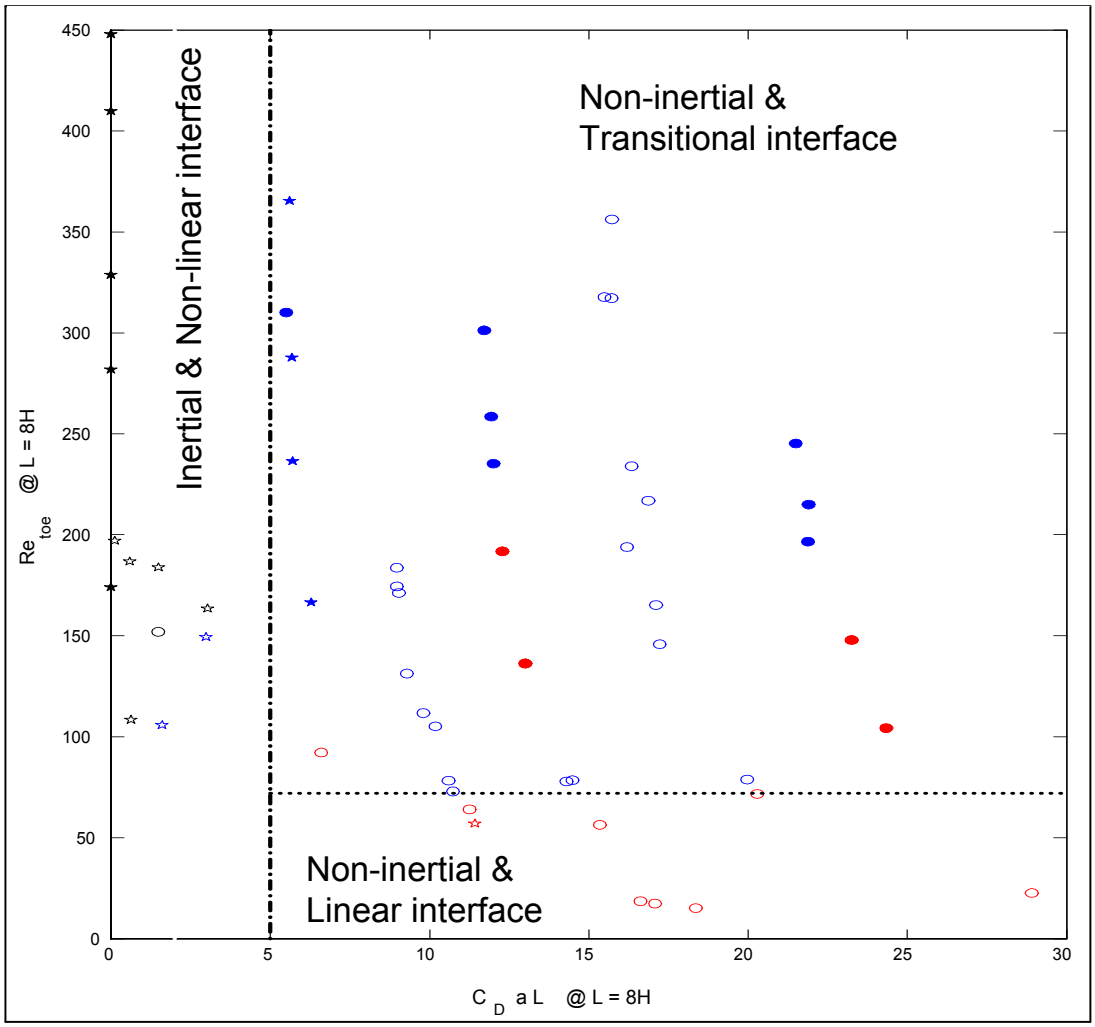

Figure 4-17: Graphic representation of the three regimes as a function of toe Re and $C_D aL$ evaluated at $L = 8H$. Solid markers represent data from Deardon, 2003. Red, blue, and black markers indicate linear, transitional, and non-linear interface profile designations, respectively. Because the slope was not recorded in Deardon, 2003, the classification of the four runs as having linear interface profiles are based on Deardon (2003)'s direct observation during the experiments. Also, blue markers for Deardon (2003)'s data indicate runs for which no observation on the interface profile were made. The pentagrams and circles indicate inertial and non-inertial runs, respectively. For inertial runs in the present study, $\mathrm{Re}_{toe}|_{L=8H}$ were determined from the gradient of the linear regression on toe position data. For non-inertial runs in the present study, $\mathrm{Re}_{toe}|_{L=8H}$ are based on interpolated toe velocities based on Equation 4.25. Re_{toe} for the data points extracted from Deardon, 2003 are interpolated at $L = 8H$ from the linear regression performed on the toe velocity measurements for each run. C_D is estimated by Equation 2.36. The horizontal perforated line $\mathrm{Re}_{toe}|_{L=8H} = 72$ and the vertical dash-dot line $C_D aL|_{L=8H} = 5$ defines the empirical boundaries below which all runs are linear and all non-linear interface runs are confined, respectively.

4.4 Synthesis of the Criteria

Figure 4-17 confirms that experimental runs are consistent with the theory: under high stem drag conditions, the interface approaches a linear profile; under low stem drag conditions, the flow exhibits the traditional inertia-dominated behavior. As discussed previously, the theory predicts that the stem drag becomes comparable to inertia when $C_D aL|_{L=8H} \approx 2$, and experimental observations agree with this criteria within uncertainty. However, the critical $\mathrm{Re}_{toe}|_{L=8H} = 72$ which marks the transition between the linear and transitional interface profile regimes in Figure 4-17 is purely empirical; the transition was defined as the $\mathrm{Re}_{toe}|_{L=8H}$ below which the runs from the present study are all linear. Similarly, $C_D aL|_{L=8H} \approx 5$, which, based on Figure 4-13, marks the transition between an inertia-dominated and a drag-dominated regime, is also empirical.

Deardon (2003)'s data exhibit reasonably good agreement with the present study. All inertial runs from the present study and all non-linear runs from both Deardon, 2003 and the present study are confined to $C_D aL|_{L=8H} < 5$, as anticipated. However, Deardon (2003)'s data appear to transition from the linear interface to the transitional interface regime at a higher $\mathrm{Re}_{toe}|_{L=8H}$ of about $\mathrm{Re}_{toe}|_{L=8H} \approx 150$ (Figure 4-17). The difference may be attributed in part to the difference in the criterion by which a run is defined to be in the linear interface profile regime. The classification of the four runs from Deardon, 2003 as exhibiting a linear interface is based on visual observation by Deardon (2003) during experimentation. In contrast, the classification for the runs from the present study is based on a quantitative parameter, as developed in Section 4.3. It is possible that the interface in the four runs from Deardon, 2003 that were classified as linear would be classified as transitional by the criterion applied to the present study. If this were the case, Deardon (2003)'s data would be consistent with the critical $\mathrm{Re}_{toe}|_{L=8H}$ extracted from the present data. Alternatively, the difference in the apparent transition point between the linear and transitional interface regimes may be a reflection of the sensitivity of the critical Re to a. Recall from Section 4.3 that the normalized interface gradient, S, (Figure 4-14) appears to exhibit a weak a-dependence. Such a functionality may account for the apparent differences between the trends in the present study and Deardon (2003)'s data.

4.5 Prediction of Toe Velocity in the Linear Interface Regime Assuming Linear Drag

4.5.1 Computation of the linear drag constant, C'

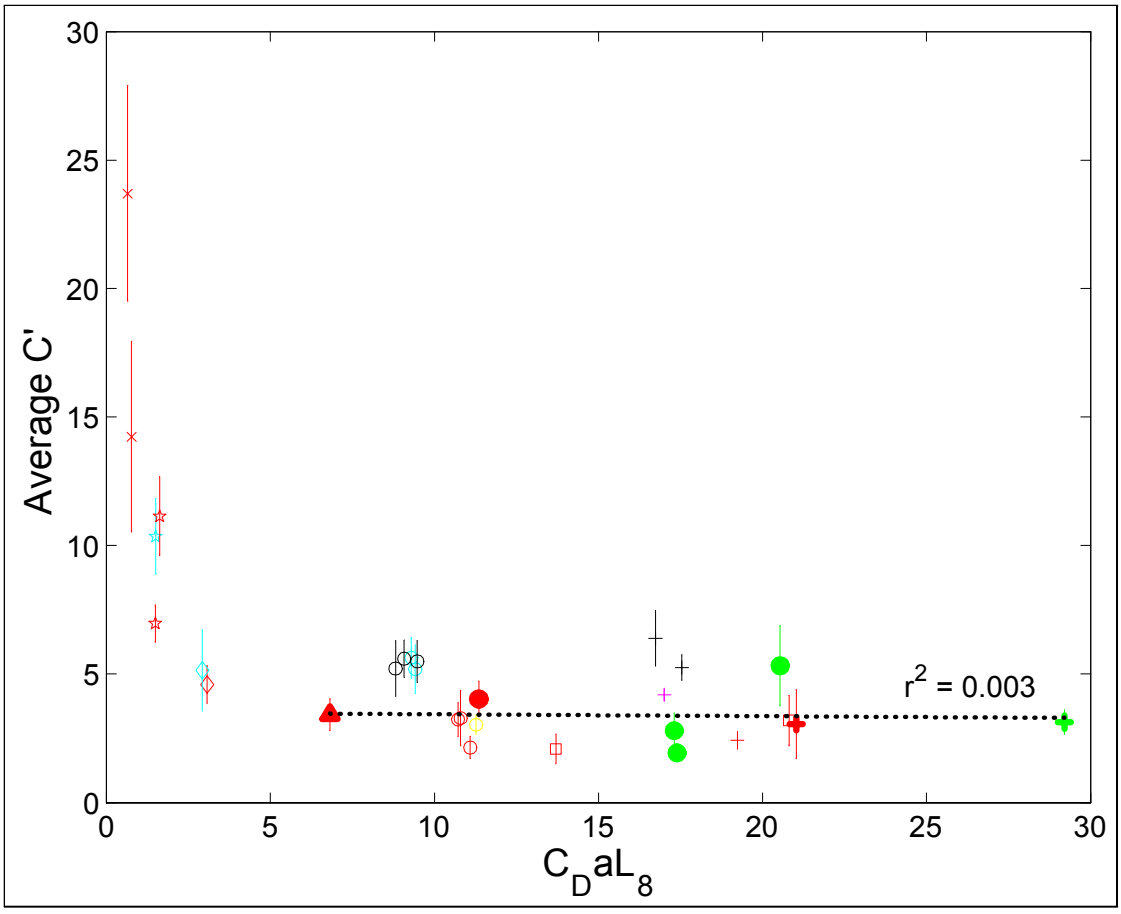

Figure 4-18: Average C' and $C_D a L_8$. Solid markers indicate non-inertial runs with a linear interface profile: 7, 12, 21, 30, 31, 32, and 36. Run 23 excluded. Vertical bars depict ± 1 standard deviation of the valid C' estimates for that run.

An average C' was extracted from each run according to the procedure detailed in Section 3.4. Only values from runs with two or more C' estimates are presented in Figure 4-18 to minimize the influence of anomalies and to allow for a non-zero standard deviation as a quantitative measure of uncertainty. As such, runs 2, 17, 23, and 33 are excluded from Figure 4-18 because only one C' estimate could be extracted. In addition, runs 1, 3, 11, 19, and 34

did not yield a valid C' estimate and are also absent from the figure.

The constant C' appears to be relatively uniform for $C_D a L_8 > 5$ in Figure 4-18, as expected. However, the estimated C' increases as $C_D a L_8$ approaches zero in the range $C_D a L_8 < 5$ and the system deviates from the non-inertial, linear interface regime. The trend in C' as illustrated in Figure 4-18 is consistent with that in S, as illustrated in Figure 4-13 which shows that at $C_D a L_8 \approx 0$, the interface is horizontal, indicating an inertial, non-linear regime, and that as $C_D a L_8$ increases the interface begins to deviate towards a linear interface.

Conversely, to predict the velocity of exchange flows using Equation 2.32, C' must be known. The average C' across the seven runs identified as both non-inertial and linear (runs 7, 12, 21, 30, 31, 32, 36) is $C' = 3.4 \pm 1.1\,\mathrm{cm\,s^{-1}}$ (± 1 standard deviation). This value agrees well at $\mathrm{Re} \approx 100$ with published values for C_D displayed in Figure 4-19 and described in Section 2.4. While the estimate deviates from Equation 2.36 at lower Re, the direction of the deviation is consistent with that of Equation 2.37, which was discussed in Chapter 2. The magnitudes of C_D predicted by the present C' estimate and Equation 2.37 relative to those predicted by Equation 2.36 suggest that cylinder drag is enhanced in arrays at low $\mathrm{Re} < 100$. In contrast, extrapolating these relationships to $\mathrm{Re} > 100$ suggests that C_D in arrays is suppressed at high Re, which is consistent with previous observations [Nepf, 1999].

Also, an order of magnitude estimate of $C_D = 3.8 \pm 0.8$ was extracted from experimental observation in Re range $230 < \mathrm{Re} < 600$ in Hatcher *et al.*, 2000 based on the study's similarity solutions. While the authors' model assumes that C_D is independent of Re, a lack of functionality not verified in the study, the observed C_D is consistent with the present data.

We lack the experimental observations to confirm that this value extracted for C' is universal. Here, the conditions for Deardon (2003)'s experimental runs for which a linear interface was observed are applied to the model with the linear drag constant defined as $C' = 3.4 \pm 1.1\,\mathrm{cm\,s^{-1}}$ to verify that the predictions are consistent with the observed toe velocities documented in Deardon, 2003. The predictions display good agreement with the experimental observations (Figure 4-20). With the exception of a few measurements, the predictions are within uncertainty of the observed toe velocities. In addition, the predictions presented in Figure 4-20 highlight the significance of the uncertainty associated with the C' estimate. The precision of the predictions is significantly restricted by the uncertainty associated with the estimated

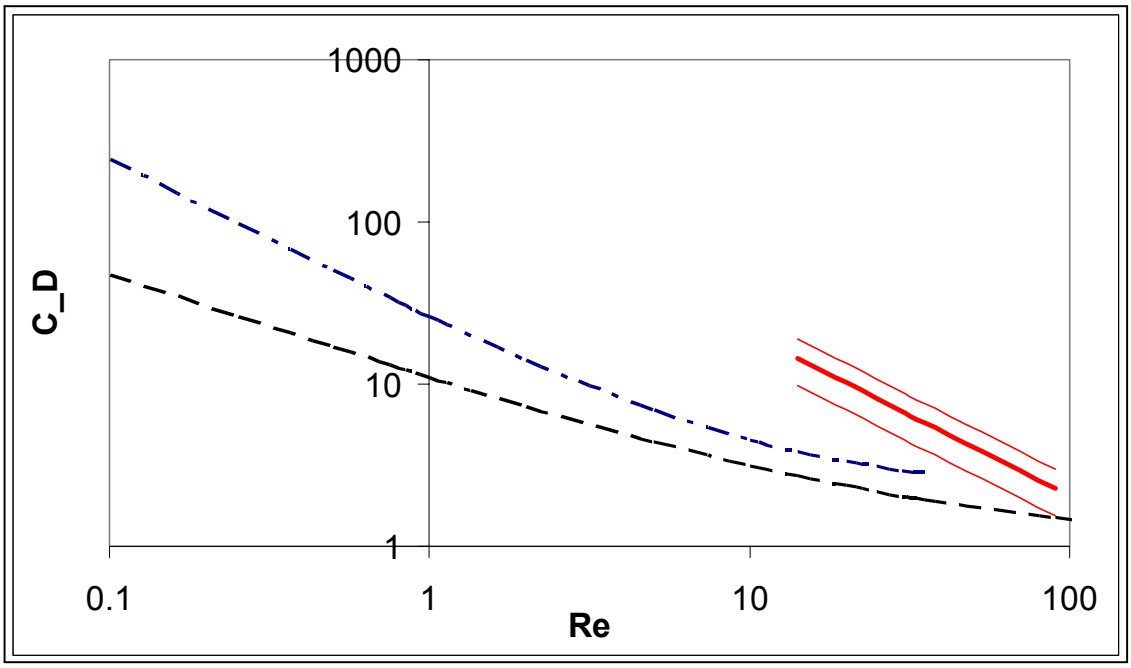

Figure 4-19: Re-dependence of C_D. Solid thick line represents $C_D = \frac{C'}{u} = \frac{3.4\,\mathrm{cm\,s^{-1}}}{u[\mathrm{cm\,s^{-1}}]}$, and the two thin solid lines reflect the uncertainty on the C' estimate: $C_D = \frac{3.4 \pm 1.1\,\mathrm{cm\,s^{-1}}}{u[\mathrm{cm\,s^{-1}}]}$. The Re range over which the curve is plotted reflects Re_{toe8} of the seven runs from which the constant was estimated. Dash-dot curve represents Equation 2.37, an expression for C_D in a random cylinder array with a solid volume fraction of 5% [Koch & Ladd, 1997], which is equivalent to $a = 0.1\,\mathrm{cm}^{-1}$ for stems used in this study. Perforated curve represents Equation 2.36, C_D for an isolated cylinder [White, 1974].

C'. Nonetheless, the agreement between the predictions and the observations suggest that our estimate of C' is reasonable.

4.5.2 Asymmetry of the linear drag momentum balance model

Recall that both the momentum balance and the linear velocity profile energy balance models yield the same solution for toe velocity when the linear drag assumption is applied (Equation 2.30). This expression yields a real solution only when $\left(\frac{C'aL}{4}\right)^2 + g'\left(\frac{H}{2} - z\right) \geqslant 0$. Where $\frac{H}{2} - z \geqslant 0$, this relation will always hold. Where $\frac{H}{2} - z < 0$, however, the flow conditions must satisfy:

$$\left(\frac{C'aL}{4}\right)^2 \geqslant g'\left|\frac{H}{2} - z\right| \tag{4.32}$$

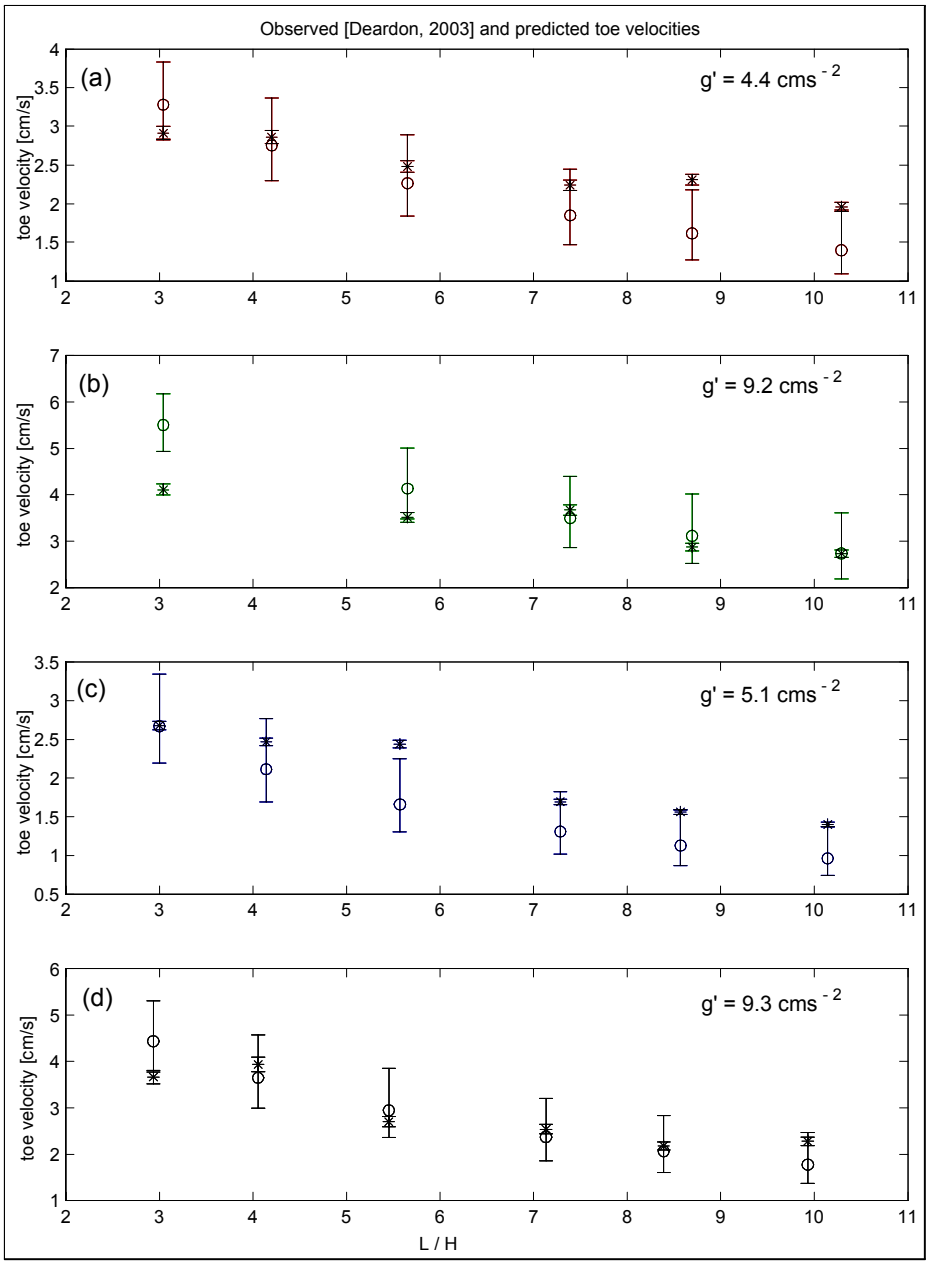

Figure 4-20: Observed (*) and predicted (∘) toe velocities for Deardon (2003)'s linear interface runs. Images (a) and (b): $a = 0.0855\,\mathrm{cm}^{-1}$; images (c) and (d): $a = 0.1497\,\mathrm{cm}^{-1}$. g' for each plot are indicated on the plot. Vertical bars represent experimental uncertainty for observed data and the uncertainty in $C' = 3.4 \pm 1.1\,\mathrm{cm\,s}^{-1}$ for the predictions (*i.e.*, the lower limit indicates predictions based on $C' = 4.4\,\mathrm{cm\,s}^{-1}$).

Thus, for a valid solution to span the entire depth, $\left(\frac{C'aL}{4}\right)^2 \geqslant g'\frac{H}{2}$. The parameters a and g' describe the experimental scenario and are constant during each run; C' is a constant. Thus, only L varies with time in this equilibrium expression. The criterion states that the interface behavior can be fully described by Equation 2.32 only if:

$$\frac{L}{H} \geqslant \frac{2\sqrt{2}}{C'a}\sqrt{\frac{g'}{H}} \tag{4.33}$$

It is interesting to note the implication of Equation 2.32 – that the velocity profile of the surface current is not a simple mirror image of that for the undercurrent. For example, the flow speed at $z = H$ differs from that at $z = 0$, as shown in Figure 4-21.

4.5.3 Linear drag model predictions

To examine more closely the shape of the interface predicted by the linear drag momentum balance model, conditions for run 31 and $C' = 3.38\,\mathrm{cm\,s^{-1}}$, as estimated above, are applied, and the predicted interface profile is compared with experimental observations (Figure 4-21). The model captures the general profile of the interface reasonably well, with the exception of the head of the undercurrent. Note that the uncertainty in g' appears to have minimal effect on predicted profiles. However, with the smaller g', it takes approximately twice as long for the undercurrent to propagate the same distance. Specifically, the predictions in Figure 4-21 required a simulation time of 78 s and 156 s, respectively, for $g' = 0.98\,\mathrm{cm\,s^{-2}}$ and $0.49\,\mathrm{cm\,s^{-2}}$. Thus, the uncertainty in g' affects the velocity predictions, with higher g' resulting in higher velocity predictions.

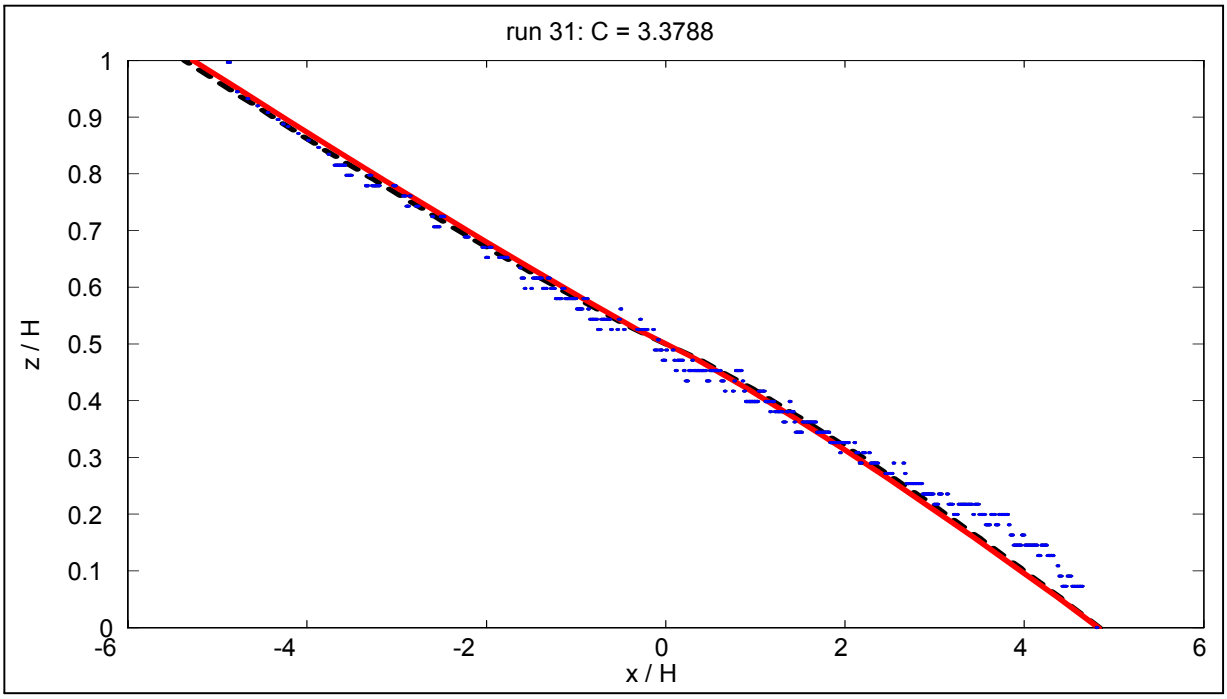

Figure 4-21: Observed and predicted interface position for run 31 at $L \approx 9.6H$. Dots indicate experimental observation at $L \approx 9.6H$. The solid and perforated lines represent predictions based on Equation 2.32, with $C' = 3.38\,\mathrm{cm\,s^{-1}}$. The former applied g' as calculated, and the latter applied the upper limit of g' within experimental uncertainty.

			Data Points	
Run Number	Linear / Nonlinear / Transitional	Inertial / Noninertial	Pattern	Color
1	T		+	blue
2	T		+	blue
3	T		+	black
4	T		square	red
5	T		circle	red
6	**N**	I	diamond	red
7	**L**		+	red
8	**N**	I	x	red
9	**N**	I	pentagram	red
11	**N**	I	*	red
12	**L**		+	green
13	T		square	red
14	T		+	black
16	T		+	magenta
17	T		+	blue
18	T		+	black
19	T		+	magenta
20	T		+	red
21	**L**		^	red
23	**L**		square	red
26	**N**		pentagram	cyan
27	T	I	diamond	cyan
28	**N**	I	x	red
29	T	I	pentagram	red
30	**L**		circle	green
31	**L**		circle	green
32	**L**		circle	green
33	**L**		circle	yellow
34	**L**		circle	yellow
35	**L**	I	circle	yellow
36	**L**		circle	red
37	T		circle	red
38	T		circle	red
39	T		circle	cyan
40	T		circle	cyan
42	T		circle	black
43	T		circle	black
44	T		circle	black

L, N, and T denote linear, nonlinear, and transitional regimes as indicated by the slope at $x = 0$. I indicates inertial runs, based on the variation in the toe velocity across that run. Toe velocity data were not available for runs 33 and 34. All other runs are noninertial. The pattern and color column indicate the marker symbols and their color in each figure. The marker shape and color indicate the stem density and m_{salt}, respectively.

Table 4.2: Classification of the experimental runs

Chapter 5

Interaction of Wind Forcing and Density Gradients

Our analyses thus far have neglected stresses and treated currents as if they were driven purely by density gradients. Accordingly, the present model (Equation 2.16) is a balance only of inertia, vegetative drag, and the pressure gradient (Chapter 2). In real systems, however, wind-induced stress may significantly enhance or inhibit convective circulation, depending on its magnitude and direction. In this chapter, a new model is developed from the Navier-Stokes equation, in which wind stress and bed friction are incorporated as boundary conditions. This enhanced model describes the interaction of wind and convective forcing, which, in many real systems, dictate the behavior of convective circulation.

5.1 Formulation

The assumptions of quasi-steady conditions, negligible vertical velocity, and two-dimensionality used to obtain Equation 2.16 in Section 2.2 are applied here as well. Coriolis effects are neglected, taking into consideration the short timescales associated with both forcing mechanisms. However, in this derivation, the stress term in the Navier-Stokes equation is retained:

$$\frac{u}{g}\frac{\partial u}{\partial x} = -\frac{1}{g\rho}\frac{\partial P}{\partial x} - \frac{C_D a u^2}{2g} + \frac{\nu}{g}\frac{\partial^2 u}{\partial z^2} \tag{5.1}$$

where ν is the kinematic viscosity $[L^2T^{-1}]$.

For simplicity, the system is assumed to be in the linear drag regime (*i.e.*, stem drag is assumed to be inversely proportional to velocity, such that $C_D = \frac{C'}{u}$). This formulation is consistent with Koch & Ladd (1997)'s numerical simulations for cylinder drag in a random array of 5% solid volume fraction for Re < 35 [Figure 26, Koch & Ladd, 1997]. Equation 2.36, which describes the drag for an isolated cylinder, also approaches a similar relationship at low Re:

$$C_D \rightarrow \frac{10\left(\frac{\nu}{d}\right)^{2/3}}{u^{2/3}} \tag{5.2}$$

Then, Equation 5.1 can be rewritten as:

$$\frac{\partial^2 u}{\partial z^2} - \frac{\left(\frac{\partial u}{\partial x} + \frac{C'a}{2}\right)}{\nu} u = \frac{1}{\rho\nu}\frac{\partial P}{\partial x} \tag{5.3}$$

This expression can be solved as a homogeneous ordinary differential equation by treating $\frac{\partial u}{\partial x}$ as a constant:

$$u_h = c_1 e^{\sqrt{\frac{\left(\frac{\partial u}{\partial x} + \frac{C'a}{2}\right)}{\nu}} z} + c_2 e^{-\sqrt{\frac{\left(\frac{\partial u}{\partial x} + \frac{C'a}{2}\right)}{\nu}} z} \tag{5.4}$$

A particular solution for Equation 5.3 is:

$$u_p = -\frac{1}{\rho}\frac{\partial P}{\partial x}\frac{1}{\left(\frac{\partial u}{\partial x} + \frac{C'a}{2}\right)} \tag{5.5}$$

Then, the solution for velocity is the linear sum of u_p and u_h:

$$u = c_1 e^{\sqrt{\frac{\left(\frac{\partial u}{\partial x} + \frac{C'a}{2}\right)}{\nu}} z} + c_2 e^{-\sqrt{\frac{\left(\frac{\partial u}{\partial x} + \frac{C'a}{2}\right)}{\nu}} z} - \frac{1}{\rho}\frac{\partial P}{\partial x}\frac{1}{\left(\frac{\partial u}{\partial x} + \frac{C'a}{2}\right)} \tag{5.6}$$

For convenience, let us define a constant $B \equiv \frac{1}{\nu}\left(\frac{\partial u}{\partial x} + \frac{C'a}{2}\right)$ such that:

$$u = c_1 e^{\sqrt{B}z} + c_2 e^{-\sqrt{B}z} - \frac{1}{B\nu}\frac{1}{\rho}\frac{\partial P}{\partial x} \tag{5.7}$$

Then, the application of the hydrostatic assumption $\frac{\partial P}{\partial x} = \frac{\partial}{\partial x}\rho g\left(H - z\right) = g\left[\left(H - z\right)\frac{\partial \rho}{\partial x} + \rho\frac{\partial H}{\partial x}\right]$

yields:

$$u = c_1 e^{\sqrt{B}z} + c_2 e^{-\sqrt{B}z} - \frac{g}{B\nu}\left[\frac{(H-z)}{\rho}\frac{\partial \rho}{\partial x} + \frac{\partial H}{\partial x}\right] \tag{5.8}$$

Boundary conditions are applied at the bed and at the free surface. First, velocity is defined to be zero at the bed:

$$u\,(z=0) = c_1 + c_2 - \frac{g}{B\nu}\left[\frac{H}{\rho}\frac{\partial \rho}{\partial x} + \frac{\partial H}{\partial x}\right] = 0 \tag{5.9}$$

Then,

$$c_2 = \frac{g}{B\nu}\left[\frac{H}{\rho}\frac{\partial \rho}{\partial x} + \frac{\partial H}{\partial x}\right] - c_1 \tag{5.10}$$

Next, the stress at the free surface is defined as the wind stress τ_w. That is,

$$\tau_w = \nu\rho\frac{\partial u}{\partial z}|_{z=H} \tag{5.11}$$

where τ_w is related to the wind velocity as:

$$\tau_w = \rho_{air} C_{10} w_{10}\,|w_{10}| \tag{5.12}$$

and $\rho_{air} = 1.2 \times 10^{-3}\,\mathrm{g\,cm^{-3}}$ is the air density, $\mathrm{C}_{10} \approx 10^{-3}$ is a drag coefficient, and w_{10} is the wind speed. Differentiating Equation 5.8 with respect to z and evaluating the result at $z = H$ yields:

$$\frac{\partial u}{\partial z}|_{z=H} = c_1\sqrt{B}e^{H\sqrt{B}} - c_2\sqrt{B}e^{-H\sqrt{B}} + \frac{g}{B\nu}\left(\frac{1}{\rho}\frac{\partial \rho}{\partial x}\right) \tag{5.13}$$

Substituting this expression into Equation 5.11 yields:

$$\tau_w = \nu\rho\left[c_1\sqrt{B}e^{H\sqrt{B}} - c_2\sqrt{B}e^{-H\sqrt{B}} + \frac{g}{B\nu}\left(\frac{1}{\rho}\frac{\partial \rho}{\partial x}\right)\right] \tag{5.14}$$

which can be rewritten as:

$$\tau_w = \nu\rho\left[c_1\sqrt{B}e^{H\sqrt{B}} - \left[\frac{g}{B\nu}\left(\frac{H}{\rho}\frac{\partial \rho}{\partial x} + \frac{\partial H}{\partial x}\right) - c_1\right]\sqrt{B}e^{-H\sqrt{B}} + \frac{g}{B\nu}\left(\frac{1}{\rho}\frac{\partial \rho}{\partial x}\right)\right] \tag{5.15}$$

Solving Equation 5.15 for c_1 yields:

$$c_1 = \frac{\frac{\tau_w}{\rho} - \frac{g}{B\rho}\frac{\partial \rho}{\partial x} + \frac{g}{\sqrt{B}}\left(\frac{H}{\rho}\frac{\partial \rho}{\partial x} + \frac{\partial H}{\partial x}\right)e^{-H\sqrt{B}}}{\nu\sqrt{B}\left(2\cosh H\sqrt{B}\right)} \tag{5.16}$$

Since total discharge must be zero in a closed steady-state system, conservation of mass:

$$\int_0^H u\, dz = 0 \tag{5.17}$$

is the third condition that must be satisfied. Evaluating this expression and solving for c_1 yields:

$$c_1 = \frac{\frac{g}{B\nu}\left(\frac{H}{\rho}\frac{\partial \rho}{\partial x} + \frac{\partial H}{\partial x}\right)\left(e^{-H\sqrt{B}} - 1\right) + \frac{g}{\sqrt{B}\nu}H\left[\frac{\partial H}{\partial x} + \frac{H}{2\rho}\frac{\partial \rho}{\partial x}\right]}{2\left[\cosh H\sqrt{B} - 1\right]} \tag{5.18}$$

Equating Equations 5.16 and 5.18 yields:

$$\frac{\partial H}{\partial x} = \frac{-\frac{\tau_w}{\rho g} + \frac{1}{B}\frac{1}{\rho}\frac{\partial \rho}{\partial x} + H\frac{1}{\rho}\frac{\partial \rho}{\partial x}\left[\frac{\cosh H\sqrt{B}}{\cosh H\sqrt{B}-1}\left(\frac{H}{2} + \frac{e^{-H\sqrt{B}}-1}{\sqrt{B}}\right) - \frac{e^{-H\sqrt{B}}}{\sqrt{B}}\right]}{\frac{e^{-H\sqrt{B}}}{\sqrt{B}} + \frac{\cosh H\sqrt{B}}{1-\cosh H\sqrt{B}}\left(H + \frac{e^{-H\sqrt{B}}-1}{\sqrt{B}}\right)} \tag{5.19}$$

which describes the slope of the free surface as a function of specified parameters. As in Chapter 2, the density gradient is scaled as $\frac{\partial \rho}{\partial x} \sim \frac{(\rho_2 - \rho_1)}{L} < 0$. Substituting Equations 5.10, 5.16, and 5.19 into Equation 5.8 yields a momentum balance model that accounts for wind stress.

5.1.1 Comparison of the predicted profiles

To compare this model with the momentum balance model derived in Section 2.2, the experimental conditions for run 32, a linear profile, non-inertial run (Table 4.1), were applied to Equations 2.21 and 5.8. Observe that in the absence of wind stress, the velocity profiles predicted by the two models are similar but not identical in shape, as shown in Figure 5-1. The differences between the two profiles illustrate the effect of neglecting stresses. Because the no-slip boundary condition is not applied in deriving Equation 2.21, u monotonically decreases with increasing z. In contrast, the depth of maximum velocity in the undercurrent is approximately $z \sim \frac{H}{10}$ when modeled by Equation 5.8.

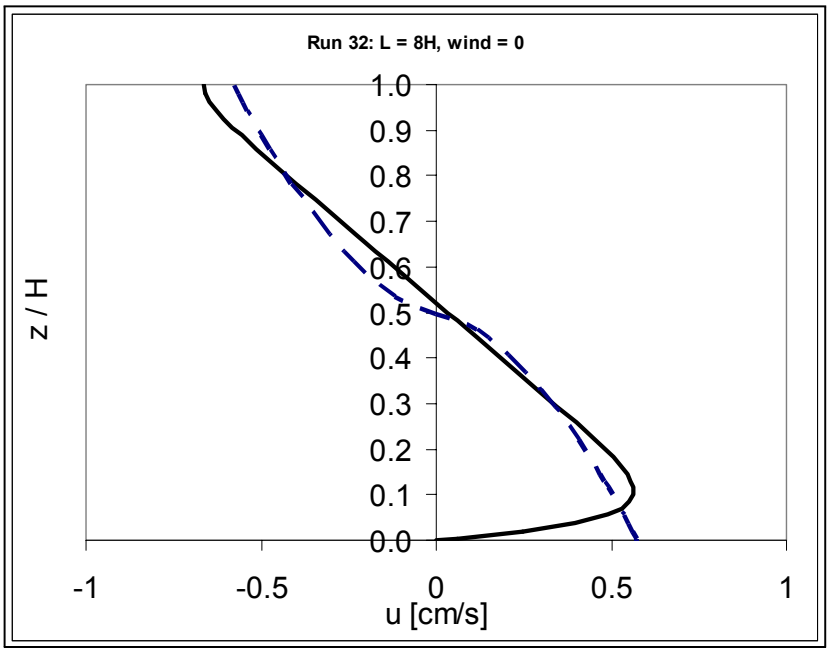

Figure 5-1: Effect of bed friction on the velocity profile as illustrated by the two momentum balance models. Perforated and solid lines represent the predicted velocity profiles for run 32 at $L = 8H$ based on Equations 2.21 and 5.8, respectively, with $C' = 1\,\mathrm{cm\,s^{-1}}$ and $\tau_w = 0$. C_D was determined by applying velocity predictions to Equation 2.36. The velocities were recalculated based on the new C_D estimates, and the process was reiterated until the predictions converged.

5.2 Comparison of Wind and Convective Forcing

The relative importance of wind forcing and density difference may be defined in terms of the critical wind stress required to counteract the convective forcing so that the velocity at the free surface becomes zero. This condition – $u(z = H) = 0$ – is satisfied when:

$$c_1 e^{H\sqrt{B}} + c_2 e^{-H\sqrt{B}} - \frac{g}{B\nu}\frac{\partial H}{\partial x} = 0 \tag{5.20}$$

which simplifies to:

$$\frac{\partial H}{\partial x} = \frac{2c_1 \frac{B\nu}{g} \sinh H\sqrt{B} + \frac{H}{\rho}\frac{\partial \rho}{\partial x} e^{-H\sqrt{B}}}{\left(1 - e^{-H\sqrt{B}}\right)} \tag{5.21}$$

where c_1 is defined by Equations 5.16 and 5.18 and $\frac{\partial H}{\partial x}$ is described by Equation 5.19. Both parameters are functions of wind stress.

Replacing c_1 yields:

$$\frac{\partial H}{\partial x}\left[\left(1-e^{-H\sqrt{B}}-H\sqrt{B}\right)\frac{\sinh H\sqrt{B}}{\left(\cosh H\sqrt{B}-1\right)}+\left(1-e^{-H\sqrt{B}}\right)\right] = \frac{H}{\rho}\frac{\partial \rho}{\partial x}\left[\left(e^{-H\sqrt{B}}-1+\frac{H\sqrt{B}}{2}\right)\frac{\sinh H\sqrt{B}}{\left(\cosh H\sqrt{B}-1\right)}+e^{-H\sqrt{B}}\right] \tag{5.22}$$

Substituting the expression for $\frac{\partial H}{\partial x}$ yields an expression for the ratio of wind and convective forcing:

$$-\frac{\tau_w B}{g\frac{\partial \rho}{\partial x}} = -1+H\sqrt{B}\left[\begin{array}{c} e^{-H\sqrt{B}}+\frac{\left[e^{-H\sqrt{B}}-\frac{\cosh H\sqrt{B}}{\left(1-\cosh H\sqrt{B}\right)}\left(1-e^{-H\sqrt{B}}-H\sqrt{B}\right)\right]}{\left[\left(1-e^{-H\sqrt{B}}-H\sqrt{B}\right)\frac{\sinh H\sqrt{B}}{\left(\cosh H\sqrt{B}-1\right)}+1-e^{-H\sqrt{B}}\right]} \\ \times\left[\frac{\sinh H\sqrt{B}}{\left(1-\cosh H\sqrt{B}\right)}\left(1-e^{-H\sqrt{B}}-\frac{H\sqrt{B}}{2}\right)+e^{-H\sqrt{B}}\right] \\ -\frac{\cosh H\sqrt{B}}{\left(1-\cosh H\sqrt{B}\right)}\left(1-e^{-H\sqrt{B}}-\frac{H\sqrt{B}}{2}\right) \end{array}\right] \tag{5.23}$$

Let us define the left hand side of Equation 5.23 as a dimensionless parameter W:

$$W \equiv -\frac{\tau_w B}{g\frac{\partial \rho}{\partial x}} \tag{5.24}$$

The expression on the right hand side of Equation 5.23 describes the critical value for W, $W_{critical}$, for a given set of conditions H, C', and a, when the velocity at the free surface is exactly zero:

$$W_{critical} = H\sqrt{B}\left[\begin{array}{c} e^{-H\sqrt{B}}+\frac{\left[e^{-H\sqrt{B}}-\frac{\cosh H\sqrt{B}}{\left(1-\cosh H\sqrt{B}\right)}\left(1-e^{-H\sqrt{B}}-H\sqrt{B}\right)\right]}{\left[\left(1-e^{-H\sqrt{B}}-H\sqrt{B}\right)\frac{\sinh H\sqrt{B}}{\left(\cosh H\sqrt{B}-1\right)}+1-e^{-H\sqrt{B}}\right]} \\ \times\left[\frac{\sinh H\sqrt{B}}{\left(1-\cosh H\sqrt{B}\right)}\left(1-e^{-H\sqrt{B}}-\frac{H\sqrt{B}}{2}\right)+e^{-H\sqrt{B}}\right] \\ -\frac{\cosh H\sqrt{B}}{\left(1-\cosh H\sqrt{B}\right)}\left(1-e^{-H\sqrt{B}}-\frac{H\sqrt{B}}{2}\right) \end{array}\right]-1 \tag{5.25}$$

Accordingly, the wind stress is sufficiently strong to reverse the direction of the current at the

free surface when the following criterion is satisfied:

$$W > W_{critical} \tag{5.26}$$

The sign of W reflects the direction of the wind, given our definition of the Cartesian coordinates $\left(\frac{\partial \rho}{\partial x} \leqslant 0\right)$. Because the right hand side of Equation 5.26 is positive when $H\sqrt{B}$ corresponds to typical conditions found in nature, the wind must be blowing against the surface current, *i.e.*, $\tau_w > 0$, for Equation 5.26 to be satisfied.

5.2.1 Characteristic velocity profiles

Figures 5-2 and 5-3 display characteristic velocity profiles for positive and negative wind velocities, respectively.

In the absence of wind, the density gradient creates a two-layered system with an undercurrent and surface current propagating in the positive and negative direction, respectively, as shown in Figure 5-2 (a). As mentioned above, one difference between predictions by Equation 2.21 and these profiles is the no-slip condition enforced at the bed. The resulting asymmetry in the profile implies that for conservation of mass to be satisfied, the depth at which the velocity is zero is not fixed at mid-depth, as was assumed in deriving Equation 2.21.

Wind forcing against convective currents

As the wind velocity increases in magnitude against the direction of propagation of the surface convective current ($\tau_w > 0$), the current velocity at the free surface decreases until it becomes zero at $W = W_{critical}$ (Figure 5-2 (b)). At higher wind velocities, a three-layered system, which consists of a shallow current at the surface which propagates in the direction of the wind, a layer below it which propagates in the opposite direction, and the undercurrent which propagates in the positive direction, develops (Figure 5-2 (c)).

Eventually, the wind velocity exceeds a critical value after which the undercurrent reverses direction and the system returns to a two-layered system, but with the surface and bottom layers flowing in the opposite direction to that when the system is driven by convective forcing alone. The velocity profile associated with this regime (Figure 5-2 (c): $\nu = 10\,\mathrm{cm^2\,s^{-1}}$) has the

same qualitative shape as purely wind-driven currents.

Figure 5-2 also highlights the sensitivity of the model to ν. By definition of the parameter B, doubling ν is has the equivalent effect on B as halving the a or C'; both operations result in the halving of B. $W_{critical}$ is affected according to its dependence on B, as expressed in Equation 5.25. In the example shown in Figure 5-2, a larger ν corresponds to a lower $W_{critical}$ and a higher critical wind velocity. Furthermore, Figure 5-2 (c) shows that a larger ν is associated with a lower $\frac{W}{W_{critical}}$ at which the system transitions from a three-layered flow to a reversed two-layered flow. The predicted velocity profiles for $\nu = 0.01\,\mathrm{cm^2\,s^{-1}}$ and $0.1\,\mathrm{cm^2\,s^{-1}}$ are clearly three-layered. At $\nu = 1\,\mathrm{cm^2\,s^{-1}}$ the profile is very close to the transition, and at higher ν, the flow returns to a two-layered system.

Wind forcing promoting convective currents

When $\tau_w \leqslant 0$ and the wind blows in the direction of the convective surface current, the wind forcing is expected to strengthen the convective circulation. The model correctly captures this trend: as $|W|$ becomes larger, the current velocity at the surface increases such that at $W = -100W_{critical}$, the velocity is approximately 2 orders of magnitude greater than when $W = 0$, as illustrated in Figure 5-3 (c). To compensate for this increased surface flow in the negative direction, the free surface slope and the velocity of the undercurrent must become more negative and positive, respectively; this anticipated behavior is also reproduced by the model.

As expected, when the wind enhances the convective surface current, the surface current speed is larger for a given $|W|$ than if the wind were blowing in the positive direction with the same magnitude, as can be seen by comparison of Figures 5-2 (c) and 5-3 (b).

5.3 Summary

This momentum balance model accurately captures the anticipated qualitative response of convective currents to wind forcing, which is also consistent with field observations [Roget *et al.*, 1993]. This model enables us to better predict the occurrence of convective circulation in the presence of wind forcing, and enhances our ability to describe basin-scale circulations influenced

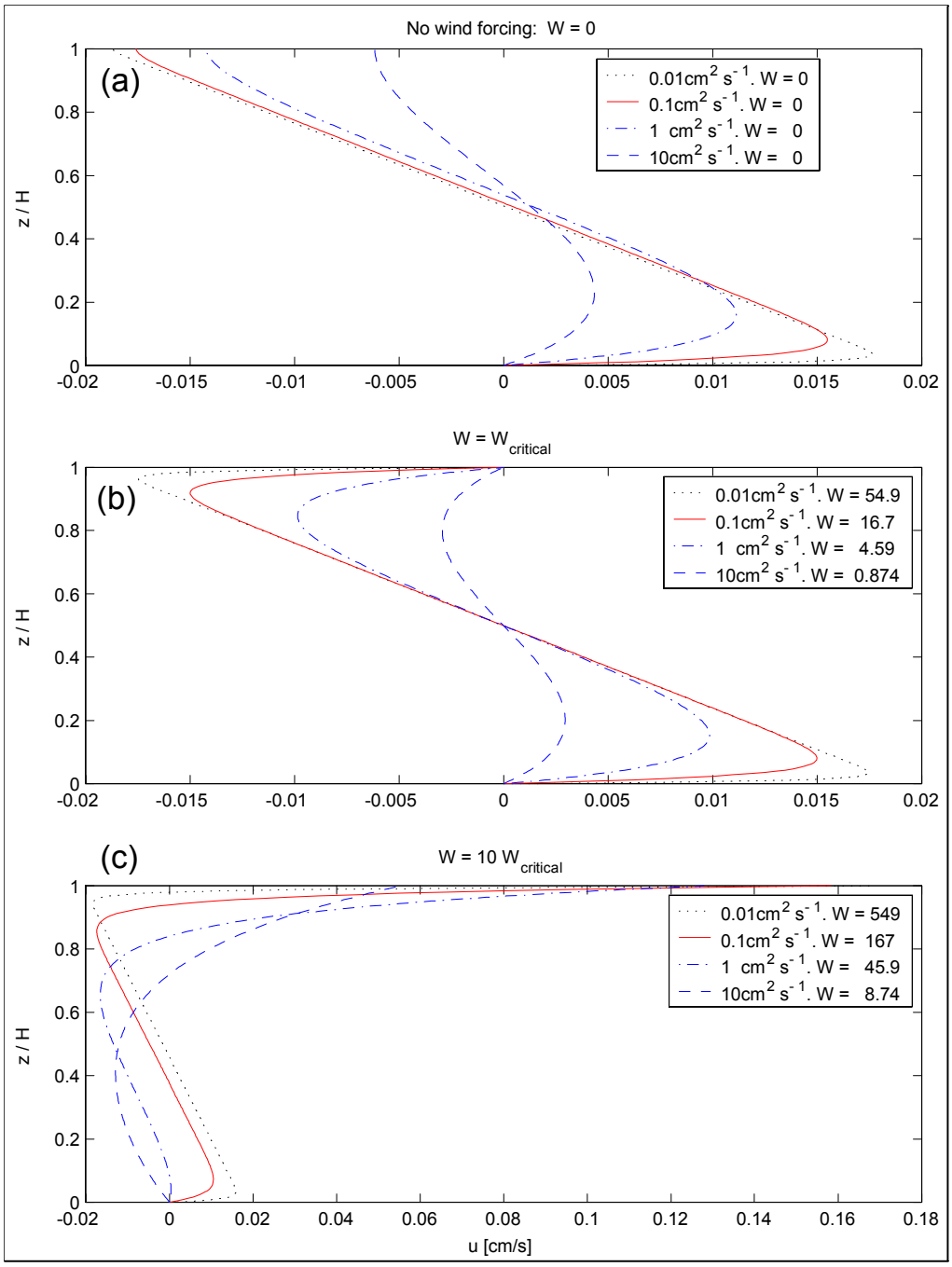

Figure 5-2: Characteristic velocity profiles under three wind conditions that oppose convective currents (a) $W = 0$; (b) $W = W_{critical}$; and (c) $W = 10W_{critical}$ for $\nu = 0.01\,\mathrm{cm^2\,s^{-1}}$ (perforated), $0.1\,\mathrm{cm^2\,s^{-1}}$ (solid), $1\,\mathrm{cm^2\,s^{-1}}$ (dash-dot), and $10\,\mathrm{cm^2\,s^{-1}}$ (dashed). The first and second number for each data set in the key indicates the corresponding ν and W, respectively. The flow conditions are: $H = 50\,\mathrm{cm}$; $C' = 1\,\mathrm{cm\,s^{-1}}$; $a = 0.1\,\mathrm{cm^{-1}}$; $L = 10000\,\mathrm{cm}$; $T_1 = 18\,^\circ\mathrm{C}$; and $T_2 = 20\,^\circ\mathrm{C}$.

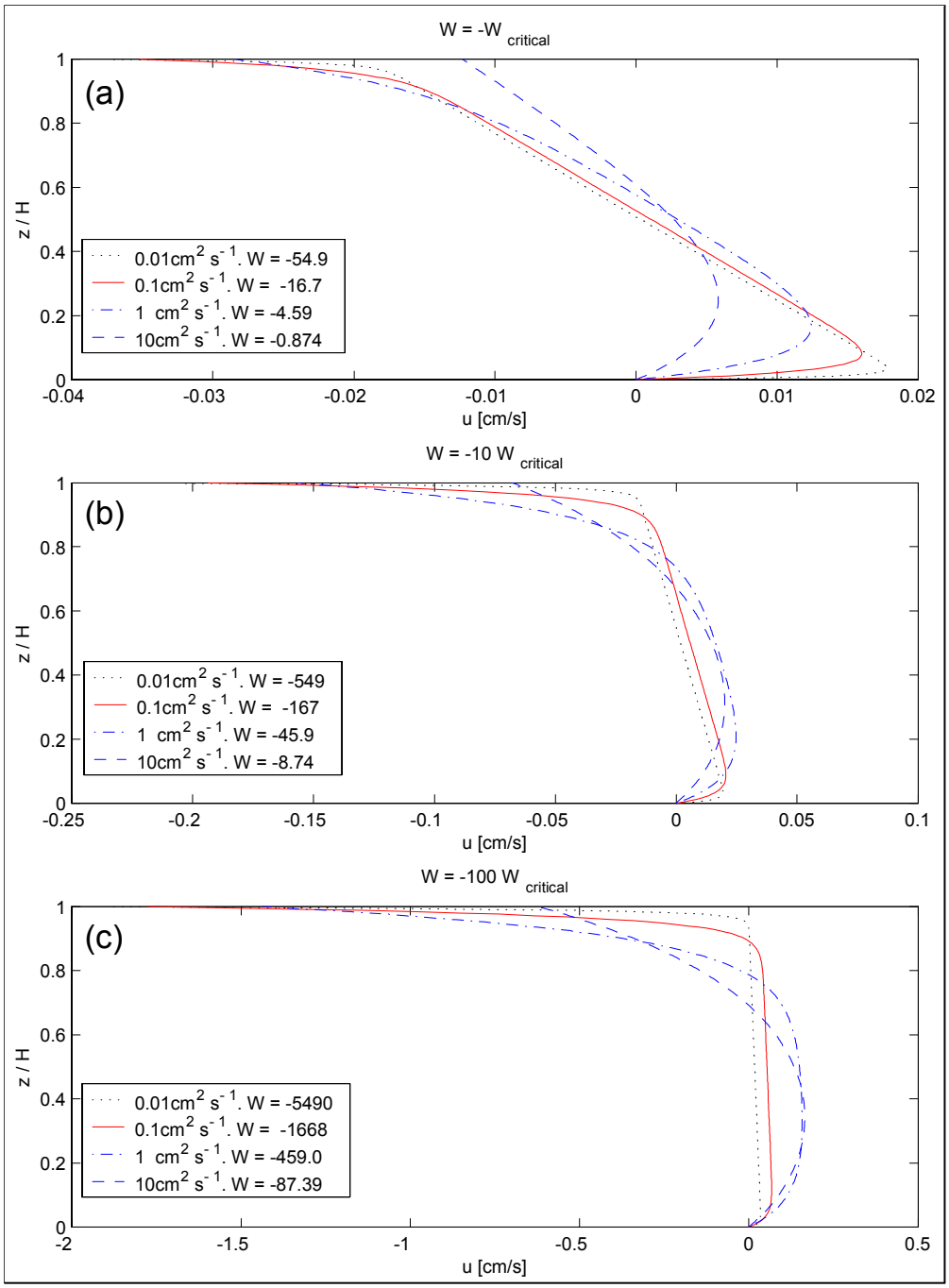

Figure 5-3: Characteristic velocity profiles for three wind conditions that promote convective currents: (a) $W = -W_{critical}$; (b) $W = -10W_{critical}$; and (c) $W = -100W_{critical}$ for $\nu = 0.01\,\mathrm{cm^2\,s^{-1}}$ (perforated), $0.1\,\mathrm{cm^2\,s^{-1}}$ (solid), $1\,\mathrm{cm^2\,s^{-1}}$ (dash-dot), and $10\,\mathrm{cm^2\,s^{-1}}$ (dashed). The first and second number for each data set in the key indicates the corresponding ν and W, respectively. The flow conditions are: $H = 50\,\mathrm{cm}$; $C' = 1\,\mathrm{cm\,s^{-1}}$; $a = 0.1\,\mathrm{cm^{-1}}$; $L = 10000\,\mathrm{cm}$; $T_1 = 18\,^\circ\mathrm{C}$; and $T_2 = 20\,^\circ\mathrm{C}$.

by a number of forcing mechanisms. For example, let us consider the system investigated by Andradóttir (2000). The following site parameters are applied: $H = 170\,\mathrm{cm}$, $L = 6000\,\mathrm{cm}$, $T_1 = 7\,^\circ\mathrm{C}$; $T_2 = 8.5\,^\circ\mathrm{C}$, as reported in Andradóttir, 2000. While the vegetation in the wetlands is identified as water lilies and coontail in Andradóttir, 2000, their stem densities are not documented. Therefore, as a first order approximation, a stem density $a = 0.012\,\mathrm{cm}^{-1}$ is chosen based on documented observations of *Spartina alterniflora* (salt-marsh cordgrass) [Valiela *et al.*, 1978], a common salt marsh grass with an approximately cylindrical morphology. The linear drag constant estimated in Section 4.5, $C' = 3.38\,\mathrm{cm\,s^{-1}}$, is employed here. The similarity in the exchange flow velocities measured in the field ($0-5\,\mathrm{cm\,s^{-1}}$ [Andradóttir, 2000]) and those measured in the laboratory in the present study justifies this extrapolation. Then, the critical wind velocity necessary to set the velocity at the free surface to zero is $w_{10} = 0.46\,\mathrm{m\,s^{-1}}$, $0.80\,\mathrm{m\,s^{-1}}$, and $1.3\,\mathrm{m\,s^{-1}}$ for $\nu = 0.1\,\mathrm{cm^2\,s^{-1}}$, $1\,\mathrm{cm^2\,s^{-1}}$, and $10\,\mathrm{cm^2\,s^{-1}}$, respectively. These velocities are approximately one order of magnitude smaller than wind velocities measured in the field by Andradóttir (2000) $\left(\text{order of } 1-10\,\mathrm{m\,s^{-1}}\right)$. These results indicate that when present, wind forcing may dominate convective forcing.

Chapter 6

Conclusions and Future Research

6.1 Conclusions

Mathematical descriptions of the velocity profile of exchange flows propagating through rigid cylindrical stems were derived from the conservation of energy and momentum. Predictions based on these expressions were compared with previously made experimental observations of frontal velocity. The theory accurately predicted the velocities in high stem density scenarios, but overestimated velocities in low stem density scenarios. The results indicate that the momentum balance solution most accurately describes the toe velocity of vegetated exchange flows ($a > 0$). For non-vegetated flows ($a = 0$), the well-documented block flow energy balance solution is the most accurate, as anticipated.

Experimental results show that the interface profile and exchange flow behavior may be predicted from the conditions of the flow and the vegetation. If $\mathrm{C}_D aL < 5$ when $\frac{L}{H} \approx 8$, the exchange flow was inertial, regardless of the magnitude of g'. For runs with greater $\mathrm{C}_D aL$, the vegetative drag had significant effect on the toe velocity and the flow was non-inertial. Furthermore, linear interfaces were observed in experiments where $Re|_{z=0} < 72$ and $\mathrm{C}_D aL > 5$ at $\frac{L}{H} \approx 8$. These results may be interpolated to predict of the interface shape and toe velocity from easily measurable and controlled flow conditions and stem density.

A linear drag regime, in which $\mathrm{C}_D \propto u^{-1}$, was proposed in response to Deardon (2003)'s observations of a linear interface profile under high stem density, low g' scenarios. Present experimental observations suggest that the constant of proportionality is $C' = 3.4 \pm 1.1\,\mathrm{cm\,s^{-1}}$.

Predictions based on the linear drag assumption agree well with experimental observation of non-inertial and linear interface flows.

Finally, a mathematical model that accounted for wind forcing and bed friction was developed to examine the potential importance of wind forcing in typical systems. When wind stress acts in the direction of propagation of the surface current (driven by convective forcing), it merely strengthens the existing convective circulation. When wind stress opposes the surface current, three regimes emerge. When wind stress is small, the wind only suppresses the velocity of the water at the free surface, and the structure of the velocity profile is essentially unchanged by the wind: a two-layered system with the undercurrent and the surface return flow propagating in opposite directions. At wind forcing increases, the current at the free surface reverses direction and flows in the direction of the wind, generating a three-layered system. Under even stronger wind forcing, the system returns to a two-layered system but with the undercurrent and surface current propagating in opposite directions as the purely convective scenario. Application of a typical wetland condition to the model shows that under typical conditions, the system may be dictated by wind forcing.

6.2 Future Research

The duration of the present experimental runs were restricted by the length of the laboratory flume, which was only 13.5 water-depths long. As such, it would be instructive to repeat some of the experiments in a longer tank that will allow the density current to propagate over long distances. Since the density gradient decreases continuously as the current propagates, the differences observed between runs with different g' should also be observable as a function of time in a single run. That is, if an exchange flow is allowed to propagate through sufficiently dense vegetation for a long distance, its interface should eventually transition from a non-linear profile to a linear profile. It would be interesting to identify and compare the critical Re and L (hence the density gradient) at which the transition occurs with the experimental observations in the present study. Additionally, as the system transitions from being inertia-dominated to drag-dominated, its rate of propagation is also expected to shift from the block flow energy balance solution to the linear velocity profile solution. Experimental confirmation

of this transition in the exchange flow regime would further support the present mathematical formulation.

The precision of the present models depends on the accuracy of the parameters C_D and C'. Our poor understanding of the Re-dependence of C_D as a function of stem density a introduces significant uncertainty in the velocity predictions. Further experimental or numerical work is necessary to determine C_D for Re and a ranges relevant to aquatic canopies. Moreover, extensive data of C_D and Re will identify the conditions under which C_D is inversely proportional to Re, if such a relationship does indeed exist, and the corresponding C' may be estimated.

Preferably, a more extensive experimental study will be conducted, in which unsteady temperature differences, and not salinity differences, generate the density gradient. As discussed in Chapter 1, lock-exchange flows are unsteady, with the density gradient monotonously decreasing. Convective forcing, in contrast, is periodic, and generates convective currents through differential heating and cooling. It is clear that a mathematical description of the density gradient becomes significantly more complicated. The system no longer consists of two distinct fluids that remain unmixed such that each fluid retains their original density; instead, a continuous range of temperatures and densities are likely to be observed. Depending on the scale of the experiment facility and the forcing, the density currents may be unsteady or quasi-steady. Finally, for differential heating or cooling to occur, the basin must exhibit some form of spatial heterogeneity, as stated in Chapter 1. While the mathematical formulation will become complex, density currents driven by convective forcing will more accurately reproduce environmental conditions.

Bibliography

Adams, E.E. & Wells, S.A. 1984. Field measurements on side arms of Lake Anna, VA. *Journal of Hydraulic Engineering* **110**: 773-793.

Andradóttir, H.Ó. 2000. Littoral wetlands and lake inflow dynamics. Ph.D. thesis. Massachusetts Institute of Technology, Cambridge.

Benjamin, T.B. 1968. Gravity currents and related phenomena. *Journal of Fluid Mechanics* **31**: 209-248.

Brocard, D.N. & Harleman, D.R.F. 1980. Two-layer model for shallow horizontal convective circulation. *Journal of Fluid Mechanics* **100**: 129-146.

Coates, M. & Ferris, J. 1994. The radiatively driven natural convection beneath a floating plant layer. *Limnology and Oceanography* **39**: 1186-1194.

Coates, M.J. & Patterson, J.C. 1993. Unsteady natural convection in a cavity with non-uniform absorption of radiation. *Journal of Fluid Mechanics* **256**: 133-161.

Dagan, G. & Zeitoun, D.G. 1998. Seawater-freshwater interface in a stratified aquifer of random permeability distribution. *Journal of Contaminant Hydrology* **29**: 185-203.

Davies, M.E. & Singh, S. 1985. The phase II trials: a data set on the effect of obstructions. *Journal of Hazardous Materials* **11**: 301-323.

Deardon, P.S. 2003. Gravity currents in vegetated aquatic systems. S.B. thesis, Massachusetts Institute of Technology, Cambridge.

Farrow, D.E. & Patterson, J.C. 1993. On the response of a reservoir sidearm to diurnal heating and cooling. *Journal of Fluid Mechanics* **246**: 143-161.

Hatcher, L., Hogg, A.J., & Woods, A.W. 2000. The effects of drag on turbulent gravity currents. *Journal of Fluid Mechanics* **416**: 297-314.

Horsch, G.M. & Stefan, H.G. 1988. Convective circulation in littoral water due to surface cooling. *Limnology and Oceanography* **33**: 1068-1083.

Horsch, G.M., Stefan, H.G., & Gavali, S. 1994. Numerical simulation of cooling-induced convective currents on a littoral slope. *International Journal for Numerical Methods in Fluids* **19**: 105-134.

Hurley, J.P., Benoit, J.M., Babiarz, C.L., Shafer, M.M., Andren, A.W., Sullivan, J.R., Hammond, R. & Webb, D.A. 1995. Influences of watershed characteristics on mercury levels in Wisconsin rivers. *Environmental Science & Technology* **29**: 1867-1875.

James, W.F., Barko, J.W., & Eakin, H.L. 1994. Convective water exchanges during differential cooling and heating: implications for dissolved constituent transport. *Hydrobiologia* **294**: 167-176.

Kadlec, R.H. 1990. Overland flow in wetlands: Vegetation resistance. *Journal of Hydraulic Engineering* **116**: 691-707.

Kalff, J. 2002. *Limnology : inland water ecosystems.* Prentice-Hall, Upper Saddle River, NJ.

Keon, N.E. 2002. Controls on arsenic mobility in contaminated wetland and riverbed sediments. Ph.D. thesis, Massachusetts Institute of Technology, Cambridge.

Keulegan, G.H. 1954. Ninth progress report on model laws for density currents. An example of density current flow in permeable media. *National Bureau of Standards Report* **3411**, U.S. Department of Commerce, Washington, D.C.

Keulegan, G.H. 1957. Thirteenth progress report on model laws for density currents. An experimental study of the motion of saline water from locks into fresh water channels. *National Bureau of Standards Report* **5168**, U.S. Department of Commerce, Washington, D.C.

Kline, S.J. & McClintock, F.A. 1953. Describing uncertainties in single sample experiments. *Mechanical Engineering* **75**: 3-8.

Kneller, B.C., Bennett, S.J., & McCaffrey, W.D. 1999. Velocity structure, turbulence, and fluid stresses in experimental gravity currents. *Journal of Geophysical Research* **104**: 5381-5391.

Koch, D.L. & Ladd, A.J.C. 1997. Moderate Reynolds number flows through periodic and random arrays of aligned cylinders. *Journal of Fluid Mechanics* **349**: 31-66.

Landry, B. 2003. Personal correspondence.

Lei, C. & Patterson, J.C. 2003. A direct three-dimensional simulation of radiation-induced natural convection in a shallow wedge. *International Journal of Heat and Mass Transfer* **46**: 1183-1197.

Lei, C. & Patterson, J.C. 2002. Natural convection in a reservoir sidearm subject to solar radiation: experimental observations. *Experiments in Fluids* **32**: 590-599.

Leonard, L.A. & Luther, M.E. 1995 Flow hydrodynamics in tidal marsh canopies. *Limnology and Oceanography* **40**: 1474-1484.

Lowe, R.J., Linden, P.F., & Rottman, J.W. 2002. A laboratory study of the velocity structure in an intrusive gravity current. *Journal of Fluid Mechanics* **456**: 33-48.

MacIntyre, S., Romero, J.R., & Kling, G.W. 2002. Spatial-temporal variability in surface layer deepening and lateral advection in an embayment of Lake Victoria, East Africa. *Limnology and Oceanography* **47**: 656-671.

Middleton, G.V. 1966. Experiments on density and turbidity currents. I. Motion of the head. *Canadian Journal of Earth Sciences* **3**: 523-546.

Mitsch, W.J. & Gosselink, J.G. 2000. *Wetlands*, 3rd ed. John Wiley & Sons, New York.

Monismith, S.G., Imberger, J., & Morison, M.L. 1990. Convective motions in the sidearm of a small reservoir. *Limnology and Oceanography* **35**: 1676-1702.

Nepf, H.M. 1999. Drag, turbulence, and diffusion in flow through emergent vegetation. *Water Resources Research* **35**: 479-489.

Nepf, H.M. & Oldham, C.E. 1997. Exchange dynamics of a shallow contaminated wetland. *Aquatic Sciences* **59**: 193-213.

O'Donnell, J. 1993. Surface fronts in estuaries: A review. *Estuaries* **16**: 12-39.

Oldham, C.E. & Sturman, J.J. 2001. The effect of emergent vegetation on convective flushing in shallow wetlands: Scaling and experiments. *Limnology and Oceanography* **46**: 1486-1493.

Patterson, J. & Imberger, J. 1980. Unsteady natural convection in a rectangular cavity. *Journal of Fluid Mechanics* **100**: 65-86.

Roget, E. & Colomer, J. 1996. Flow characteristics of a gravity current induced by differential cooling in a small lake. *Aquatic Sciences* **58**: 367-377.

Roget, E., Colomer, J., Casamitjana, X. & Llebot, J.E. 1993. Bottom currents induced by baroclinic forcing in Lake Banyoles (Spain). *Aquatic Sciences* **55**: 206-227.

Rottman, J.W., Simpson, J.E., Hunt, J.C.R., & Britter, R.E. 1985. Unsteady gravity current flows over obstacles: some observations and analysis related to the phase II trials. *Journal of Hazardous Materials* **11**: 325-340.

Simpson, J.E. 1997. *Gravity currents in the environment and the laboratory*, 2nd ed. Cambridge University Press, New York.

St. Louis, V.L., Rudd, J.W.M., Kelly, C.A., Beaty, K.G., Bloom, N.S., & Flett, R.J. 1994. Importance of wetlands as sources of methyl mercury to boreal forest ecosystems. *Canadian Journal of Fisheries and Aquatic Sciences* **51**: 1065-1076.

Stefan, H.G., Horsch, G.M., & Barko, J.W. 1989. A model for the estimation of convective exchange in the littoral region of a shallow lake during cooling. *Hydrobiologia* **174**: 225-234.

Sturman, J.J. & Ivey, G.N. 1998. Unsteady convective exchange flows in cavities. *Journal of Fluid Mechanics* **368**: 127-153.

Sturman, J.J., Ivey, G.N. & Taylor, J.R. 1996. Convection in a long box driven by heating and cooling on the horizontal boundaries. *Journal of Fluid Mechanics* **310**: 61-87.

Sturman, J.J., Oldham, C.E., & Ivey, G.N. 1999. Steady convective exchange flows down slopes. *Aquatic Sciences* **61**: 260-278.

Taylor, J.R. 1997. *Introduction to error analysis*, 2nd ed. University Science Books, Sausalito.

Tritton, D.J. 1988. *Physical fluid dynamics*, 2nd ed. Oxford University Press, Oxford.

UNESCO. 1987. International oceanographic tables. *UNESCO Technical Papers in Marine Science* **40**. UNESCO, Paris.

Valiela, I., Teal, J.M., & Deuser, W.G. 1978. The nature of growth forms in the salt marsh grass *Spartina alterniflora*. *The American Naturalist* **112**: 461-470.

Wells, M.G. & Sherman, B. 2001. Stratification produced by surface cooling in lakes with significant shallow regions. *Limnology and Oceanography* **46**: 1747-1759.

White, F.M. 1974. *Viscous fluid flow*. McGraw-Hill, New York.

Yih, C-S. 1980. *Stratified flows*. Academic Press, New York.

Appendix A

Comparison of Viscous Stresses and Stem Drag

As stated in Chapter 5, the Navier-Stokes equation for a lock-exchange flow may be written as:

$$u\frac{\partial u}{\partial x} = -\frac{1}{\rho}\frac{\partial P}{\partial x} - \frac{C_D a u^2}{2} + \nu\frac{\partial^2 u}{\partial z^2} \tag{A.1}$$

In the momentum balance model Equation 2.21 derived in Section 2.2, the stress term was neglected. This chapter confirms the validity of that assumption through a simple scaling analysis.

The viscous term can be scaled as:

$$\nu\frac{\partial^2 u}{\partial z^2} \sim \nu\frac{u}{\left(\frac{H}{2}\right)^2} = \frac{4\nu u}{H^2} \tag{A.2}$$

Thus, for the viscous term to be negligible relative to the drag term the following inequality must apply:

$$\frac{4\nu u}{H^2} \ll \frac{C_D a u^2}{2} \tag{A.3}$$

The value for u is interpolated from the linear regression of the toe velocity observations for each run. This equation can be rewritten in terms of Re by rewriting C_D and u in terms of Re

(Equation 2.36):

$$\left(1 + 10.0\,\mathrm{Re}^{-2/3}\right)\mathrm{Re} \gg \frac{8d}{aH^2} \tag{A.4}$$

The flow velocity must satisfy this condition for viscous stresses to be negligible.

The value for $\frac{8d}{aH^2}$ for runs 11 and 12 are presented in Table A.1, along with the observed toe Re at $\frac{L}{H} = 6.75$, which corresponds to approximately half of the length of the tank, and the corresponding $\left(1 + 10.0\,\mathrm{Re}^{-2/3}\right)\mathrm{Re}$. Runs 11 and 12 correspond to the lowest stem density scenario and the highest stem density and lowest density difference scenario in the present study, respectively. For both runs, $\frac{8d}{aH^2}$ is at least an order of magnitude greater than $\left(1 + 10.0\,\mathrm{Re}^{-2/3}\right)\mathrm{Re}$. These results justify the removal of the viscous stress term from the governing equations in analyzing our experimental data.

Run	$a\ \left[\mathrm{cm}^{-1}\right]$	$\frac{8d}{aH^2}$	Toe Re @ $\frac{L}{H} = 6.75$	$\left(1 + 10.0\,\mathrm{Re}^{-2/3}\right)\mathrm{Re}$
11	0.000855	30.8	199	257
12	0.1155	0.215	30	61

Table A.1: Comparison of observed Re and the minimum Re necessary for viscous stresses to be negligible relative to the drag.

Appendix B

Analysis of the Quasi-Steady Assumption

To examine the appropriateness of the quasi-steady assumption, $\frac{Du}{Dt}$ was determined from experimental data for four runs and compared with the magnitude of the other terms in the momentum balance: $u\frac{\partial u}{\partial x}$, $\frac{1}{\rho}\frac{\partial P}{\partial x}$, $\frac{C_D a u^2}{2}$, and $\nu\frac{\partial^2 u}{\partial z^2}$, which scale as $\frac{u^2}{L}$, $g\frac{1}{\rho}\frac{(\rho_1-\rho_2)}{L}\left(z-\frac{H}{2}\right)$, $\frac{C_D a u^2}{2}$, and $\frac{4\nu u}{H^2}$, respectively. For the purpose of this analysis, these terms were evaluated at $z = 0$ and with the average observed toe velocity was used as a characteristic u. White (1974)'s Re-C_D relationship was employed to evaluate C_D (Equation 2.36) in the vegetative drag term.

The results are presented in Table B.1. With the exception of run 11, $\frac{Du}{Dt}$ is one to two orders of magnitude smaller than $\frac{u^2}{L}$. The method of estimating $\frac{Du}{Dt}$ as the rate of displacement of the toe between consecutive pairs of images may be regarded as a Lagrangian observation of an Eulerian velocity, as the toe positions in one pair of consecutive images have progressed from those in the previous pair. From this perspective, $\frac{Du}{Dt}$ is effectively analogous to $\frac{\partial u}{\partial t}$, and the relative magnitudes of $\frac{Du}{Dt}$ and $\frac{\partial u}{\partial t}$ are consistent with the removal of the $\frac{\partial u}{\partial t}$ term from our models.

Incidentally, the results in Table B.1 reaffirm that the shear term $\frac{4\nu u}{H^2}$ is consistently one or more orders of magnitude smaller than the other terms and is thus negligible as we had assumed in Section 2.2.

	Run			
	2	**11**	**31**	**44**
$\frac{Du}{Dt}$	-0.3	-0.03	-0.004	-0.2
$\frac{u^2}{L}$	6	1	0.01	3
$\frac{C_D a u^2}{2}$	3	0.005	0.008	0.8
$\frac{1}{\rho}\frac{\partial P}{\partial x}$	-50	-4	-0.4	-20
$\nu\frac{\partial^2 u}{\partial z^2}$	10^{-3}	6×10^{-4}	8×10^{-5}	10^{-3}

Table B.1: Comparison of magnitudes of the terms in the momentum balance.

Appendix C

Progression of the Interface in Each Experimental Run

Each of the 38 figures in this section represents a progression of the interface over the course of the experimental run indicated in the caption. The dots are data points that represent the position of the interface in each image. These data were captured using a set of MATLAB® codes developed by Landry (2003) and modified by the present author. The horizontal and vertical axes represent the x- and z-positions of the interface, respectively, normalized by the water depth, H. The run number (Table 3.1), scale [pixels cm^{-1}], and the time [s] between each pair of consecutive images are indicated at the top of each figure.

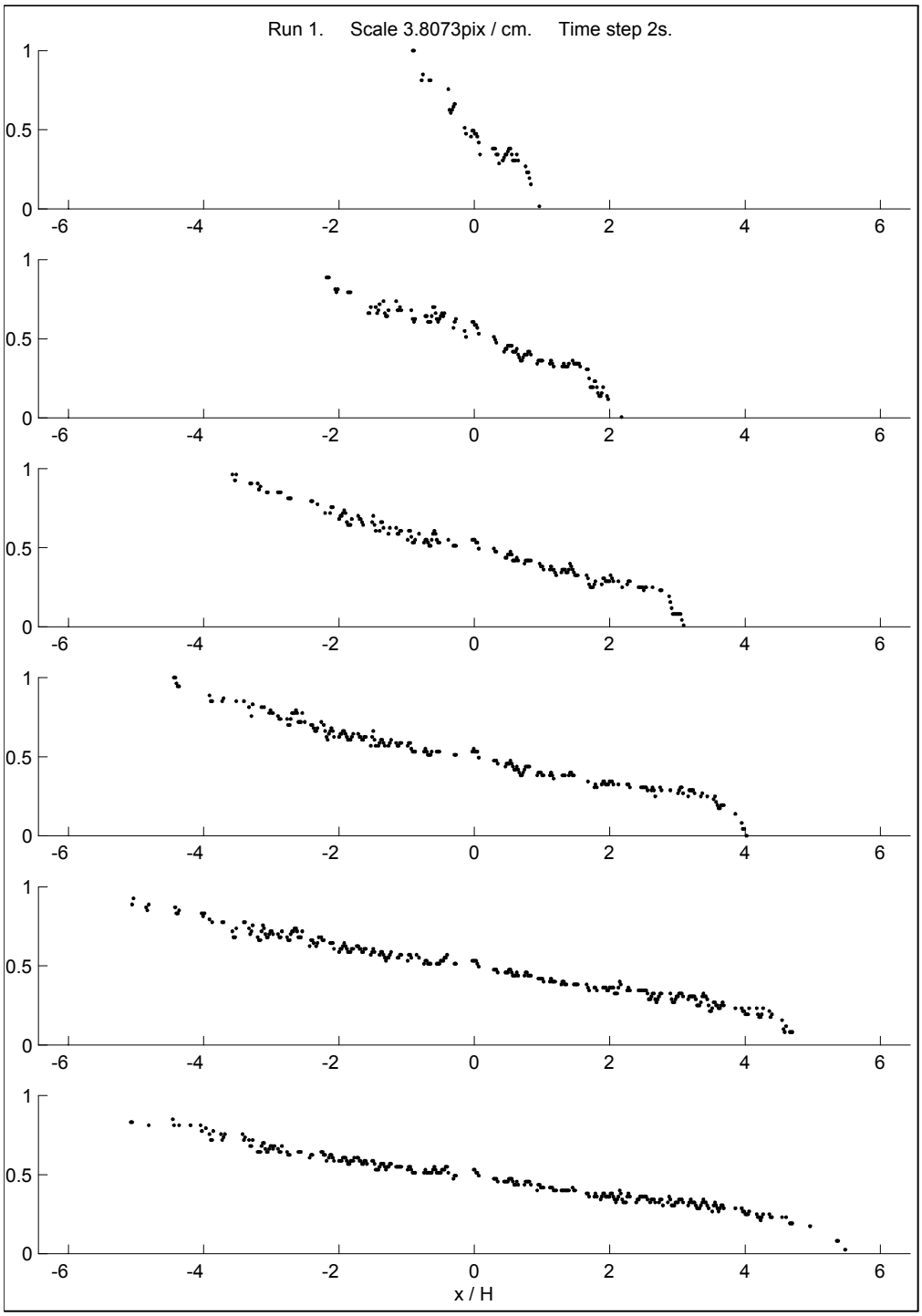

Figure C-1: Run 1.

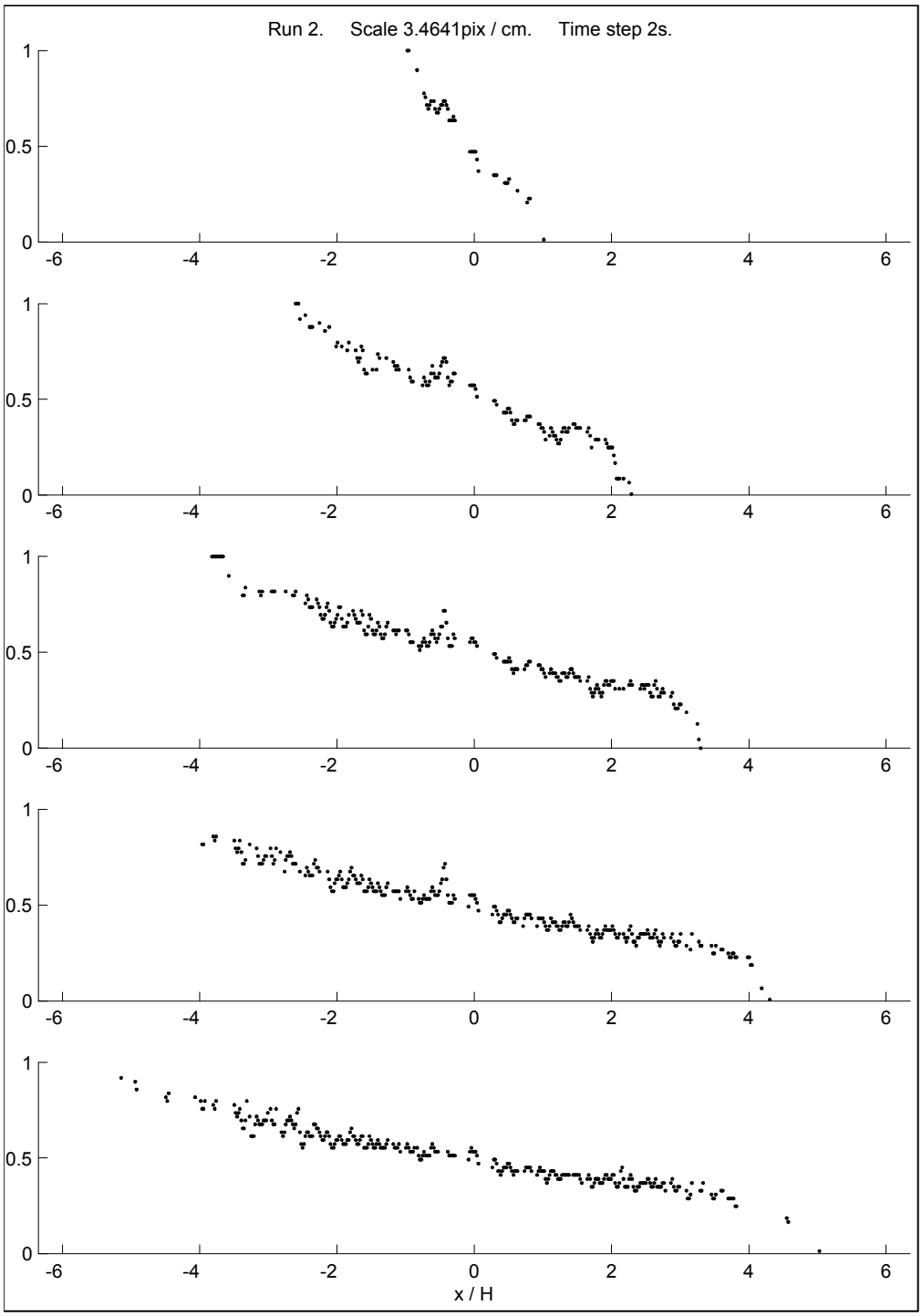

Figure C-2: Run 2.

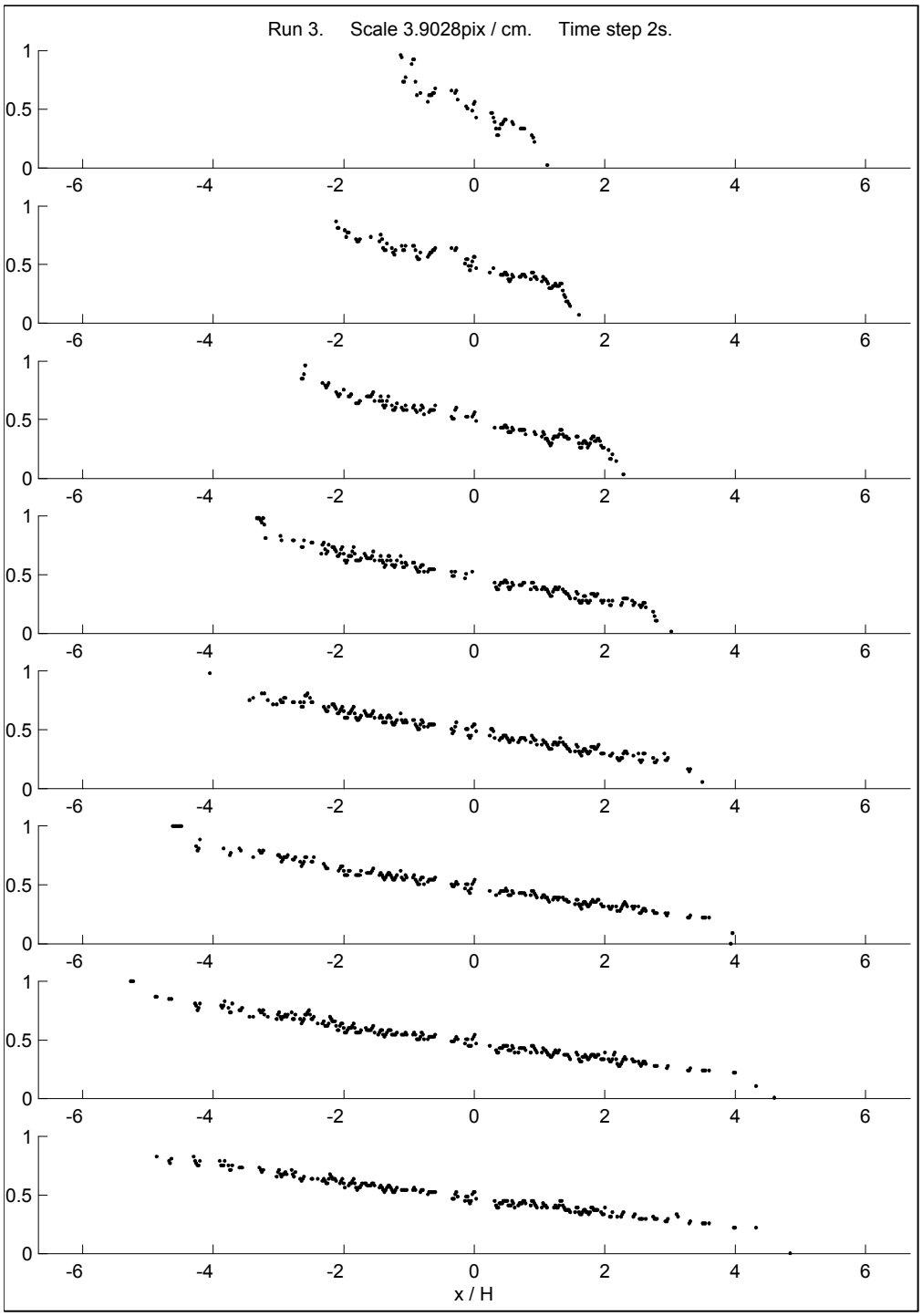

Figure C-3: Run 3.

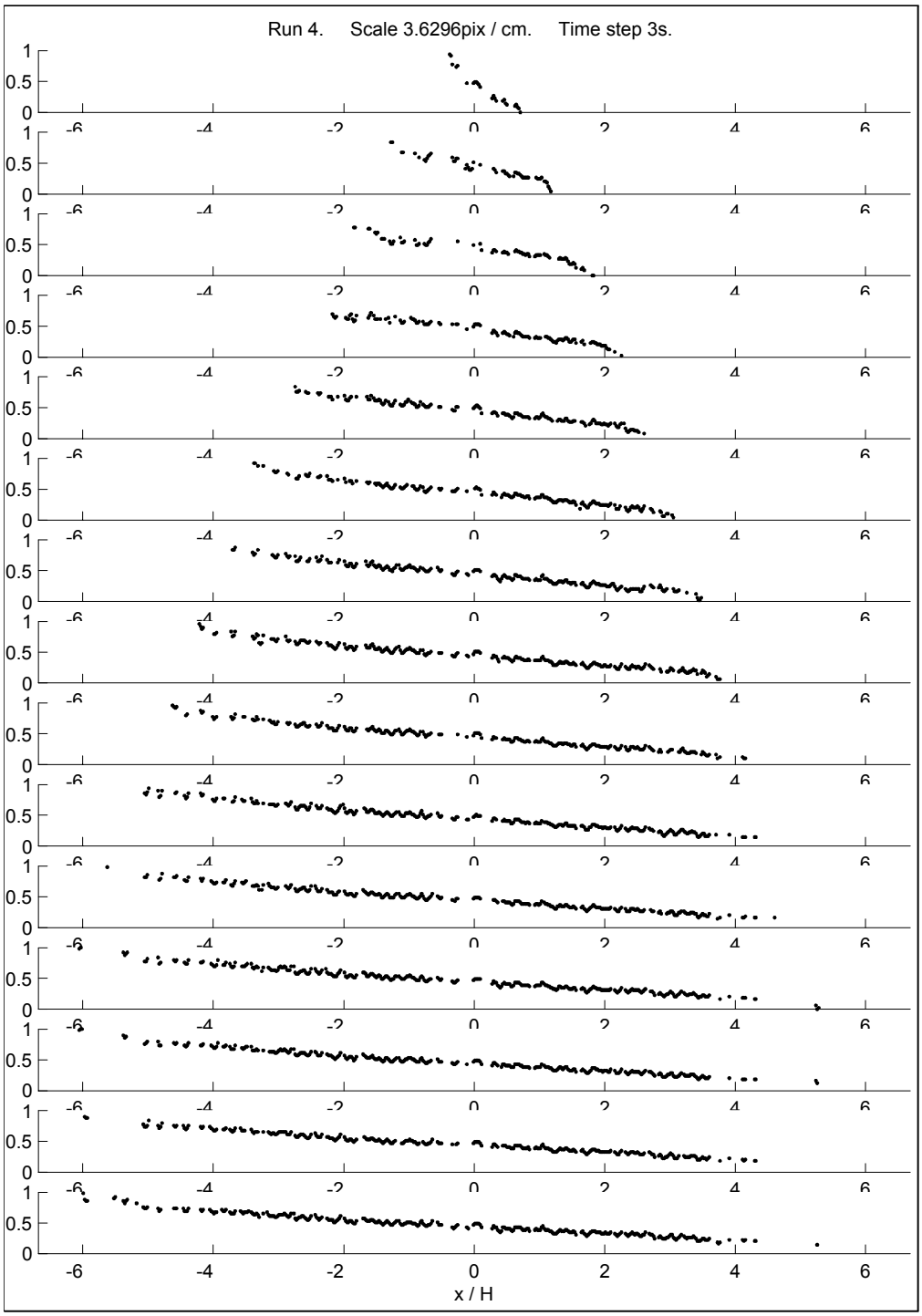

Figure C-4: Run 4.

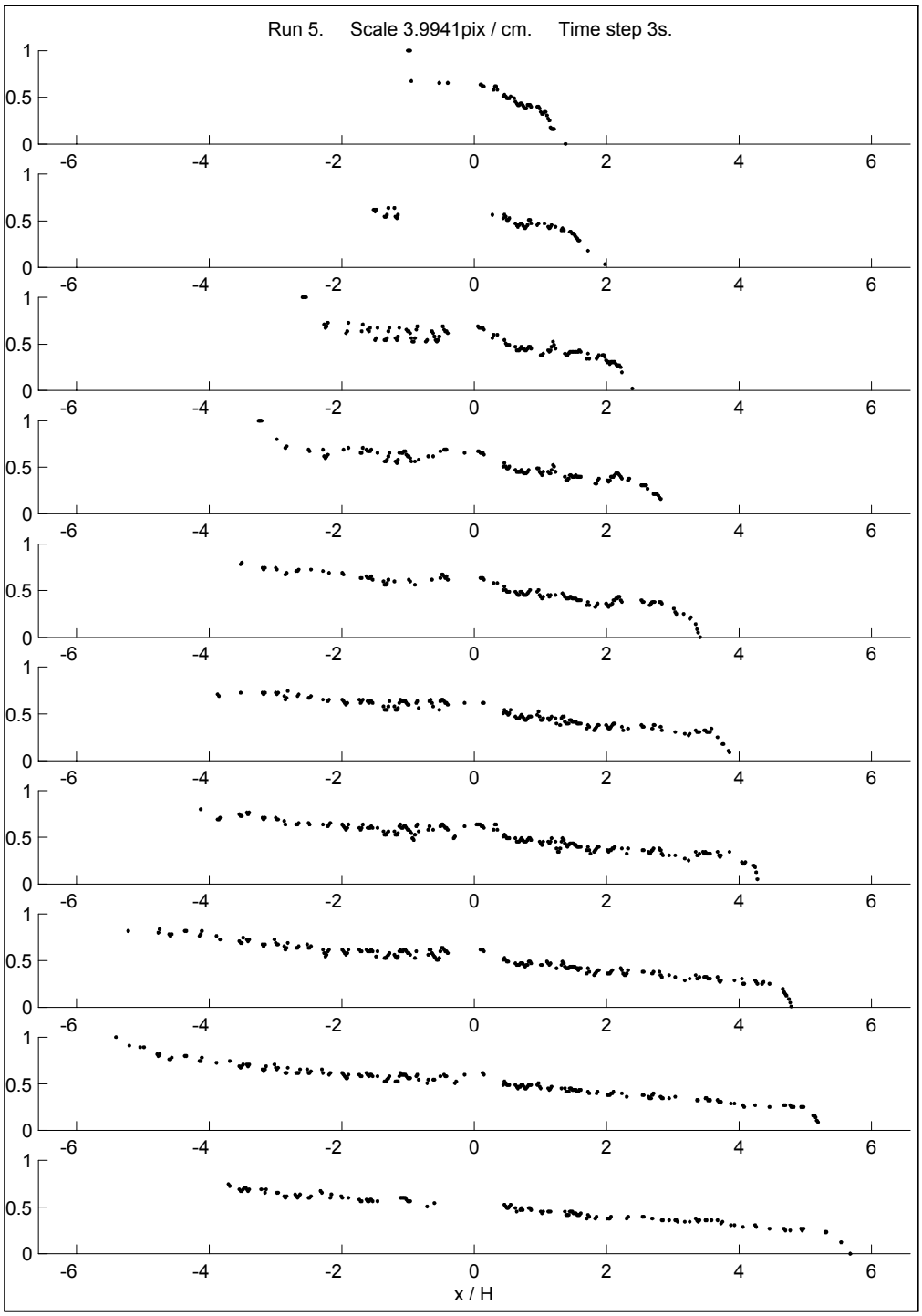

Figure C-5: Run 5.

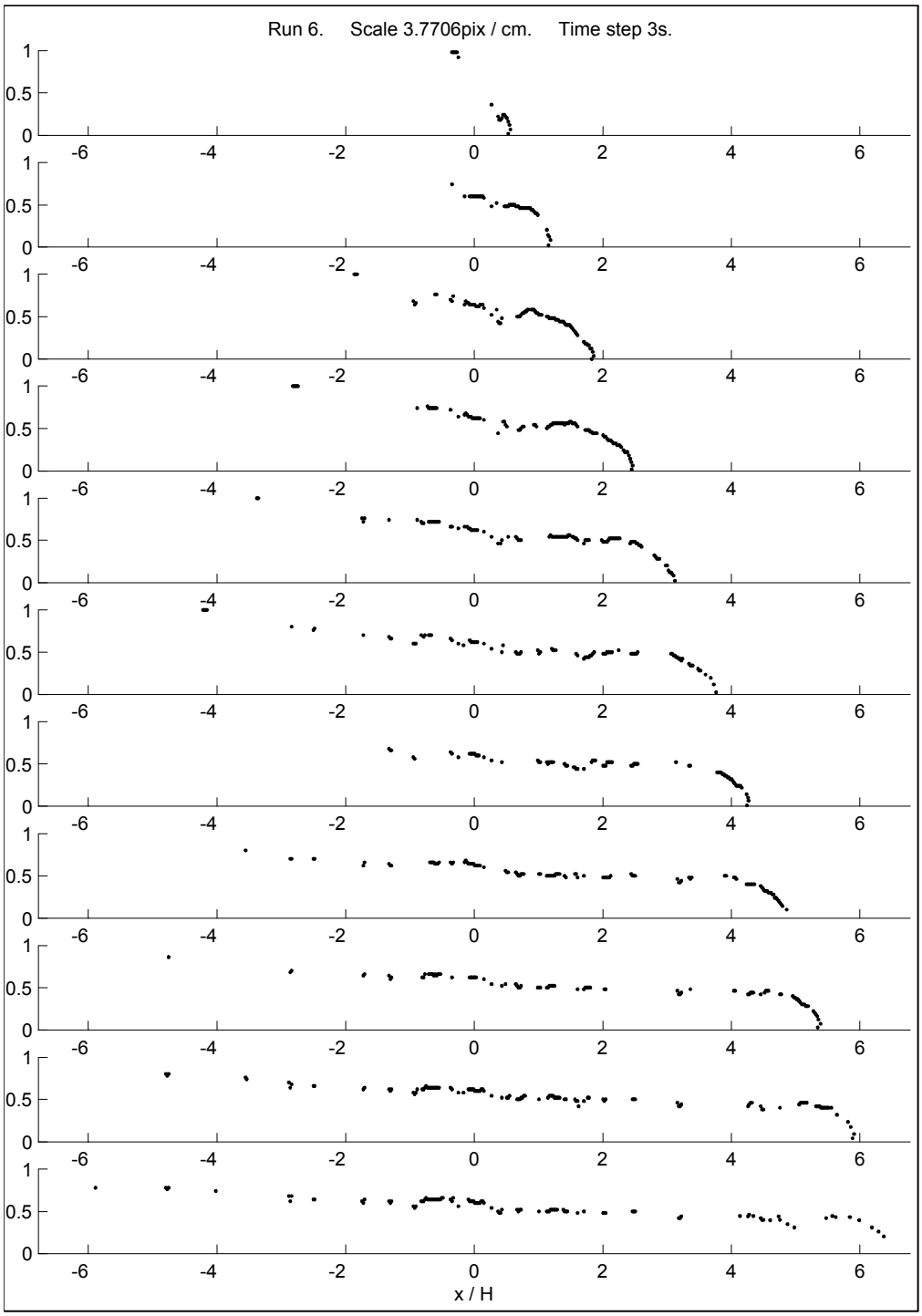

Figure C-6: Run 6.

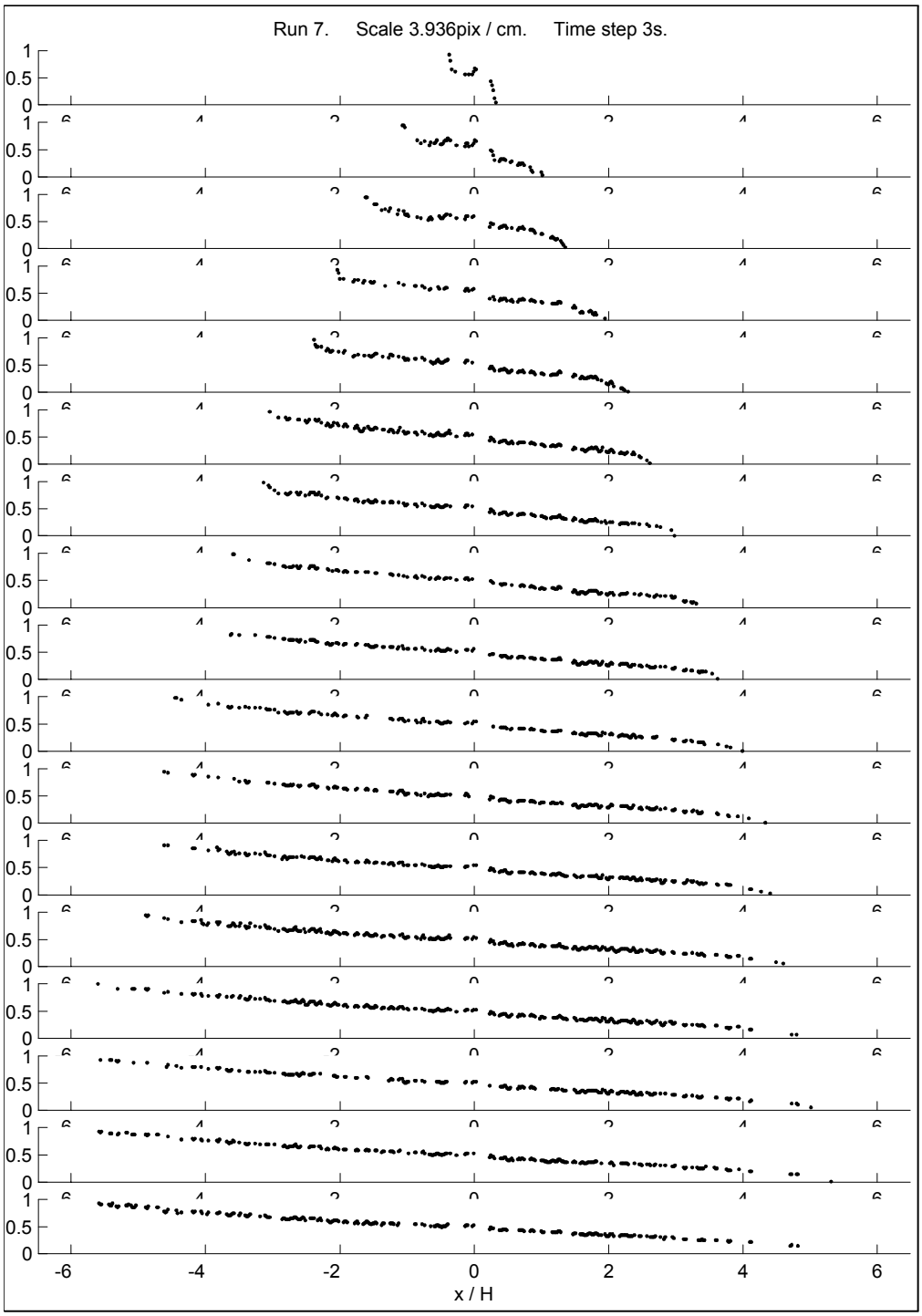

Figure C-7: Run 7.

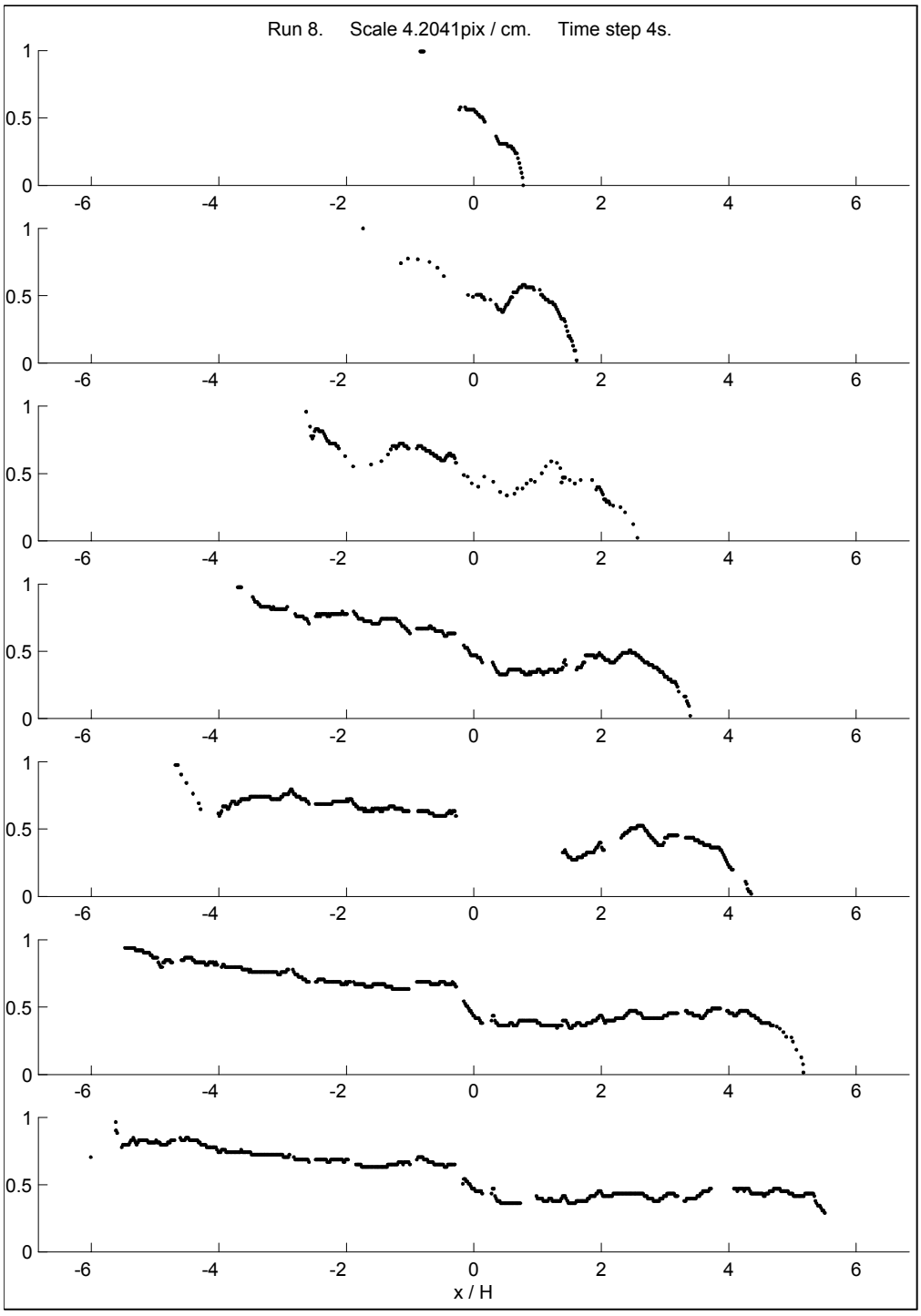

Figure C-8: Run 8.

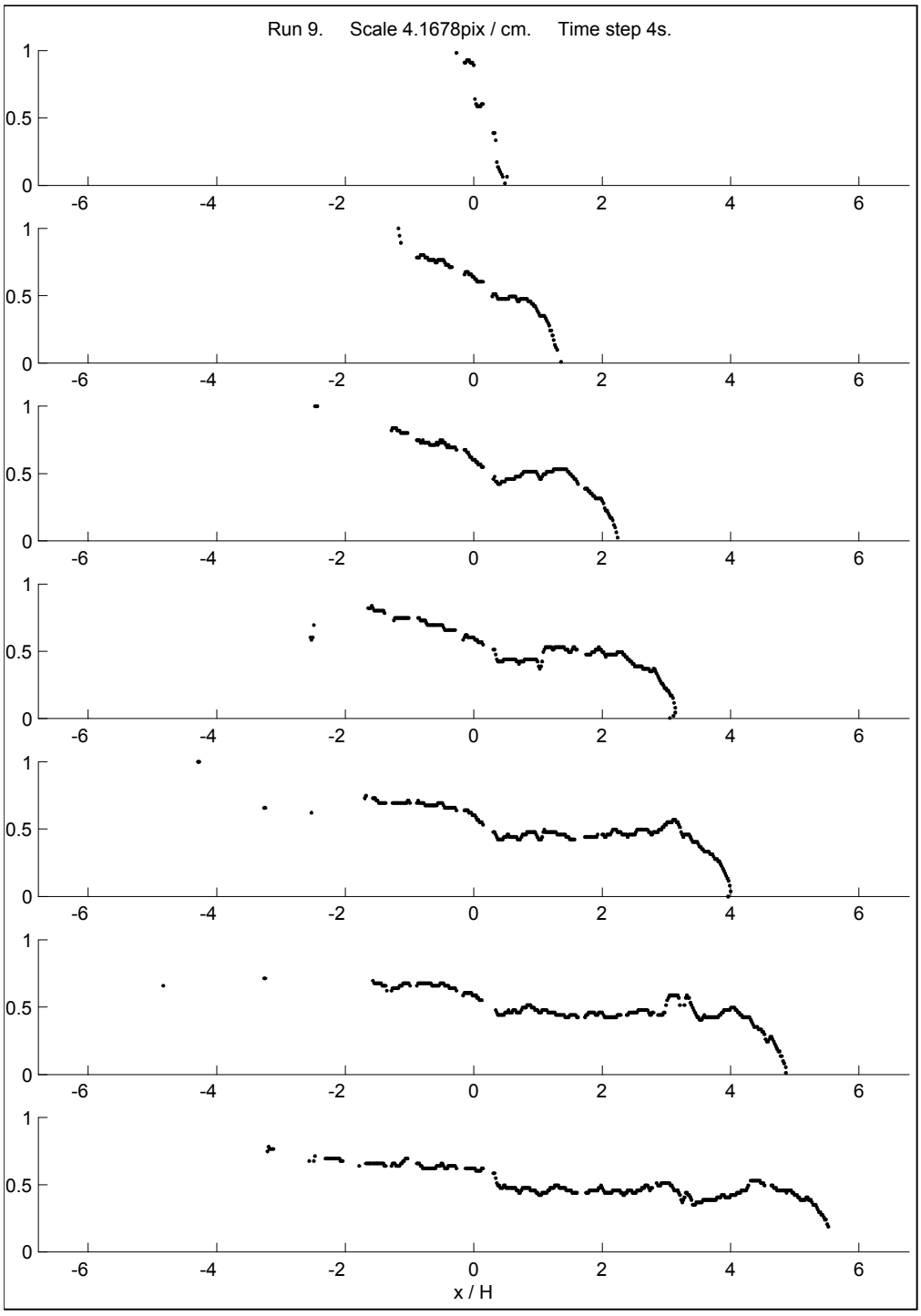

Figure C-9: Run 9.

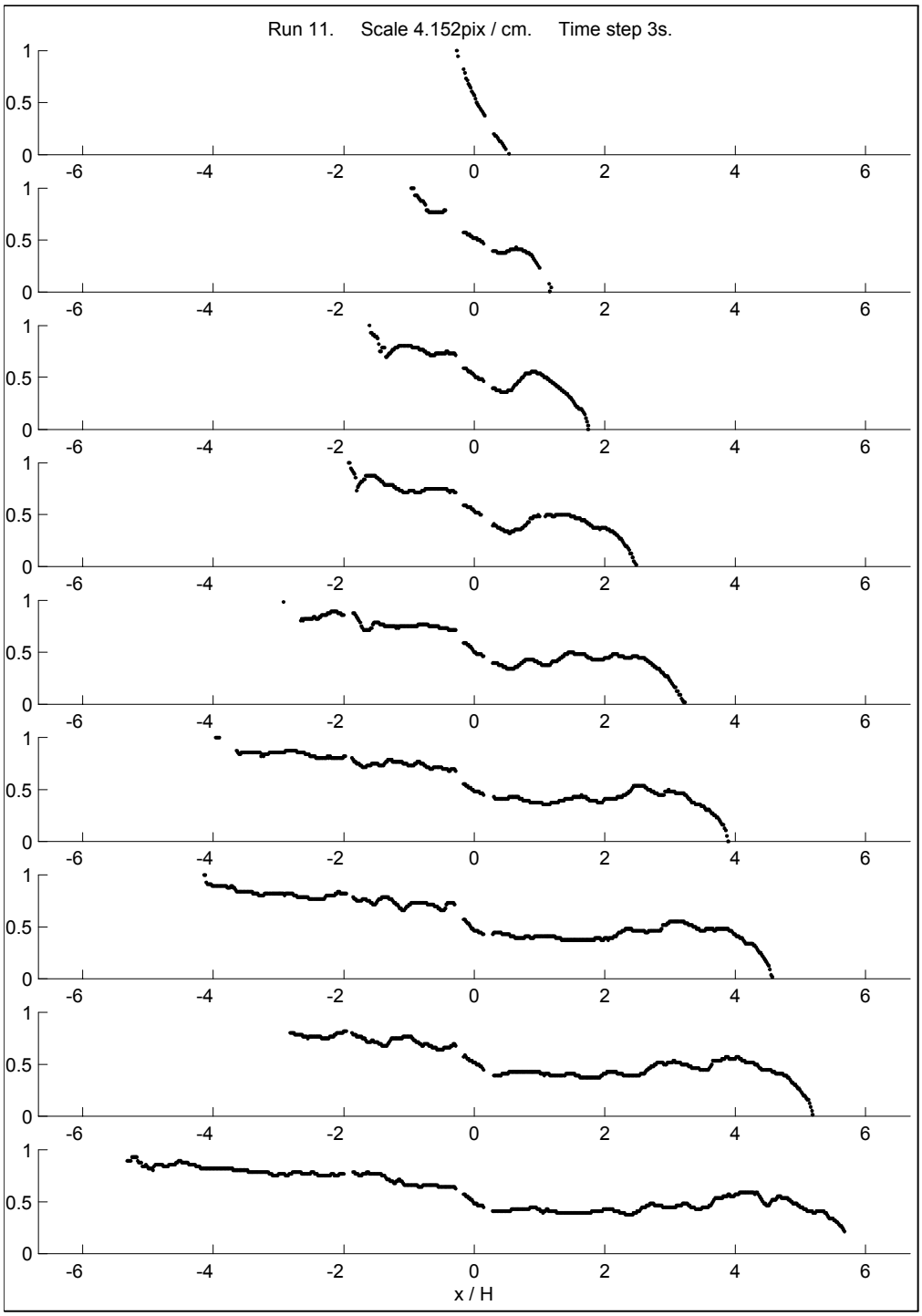

Figure C-10: Run 11.

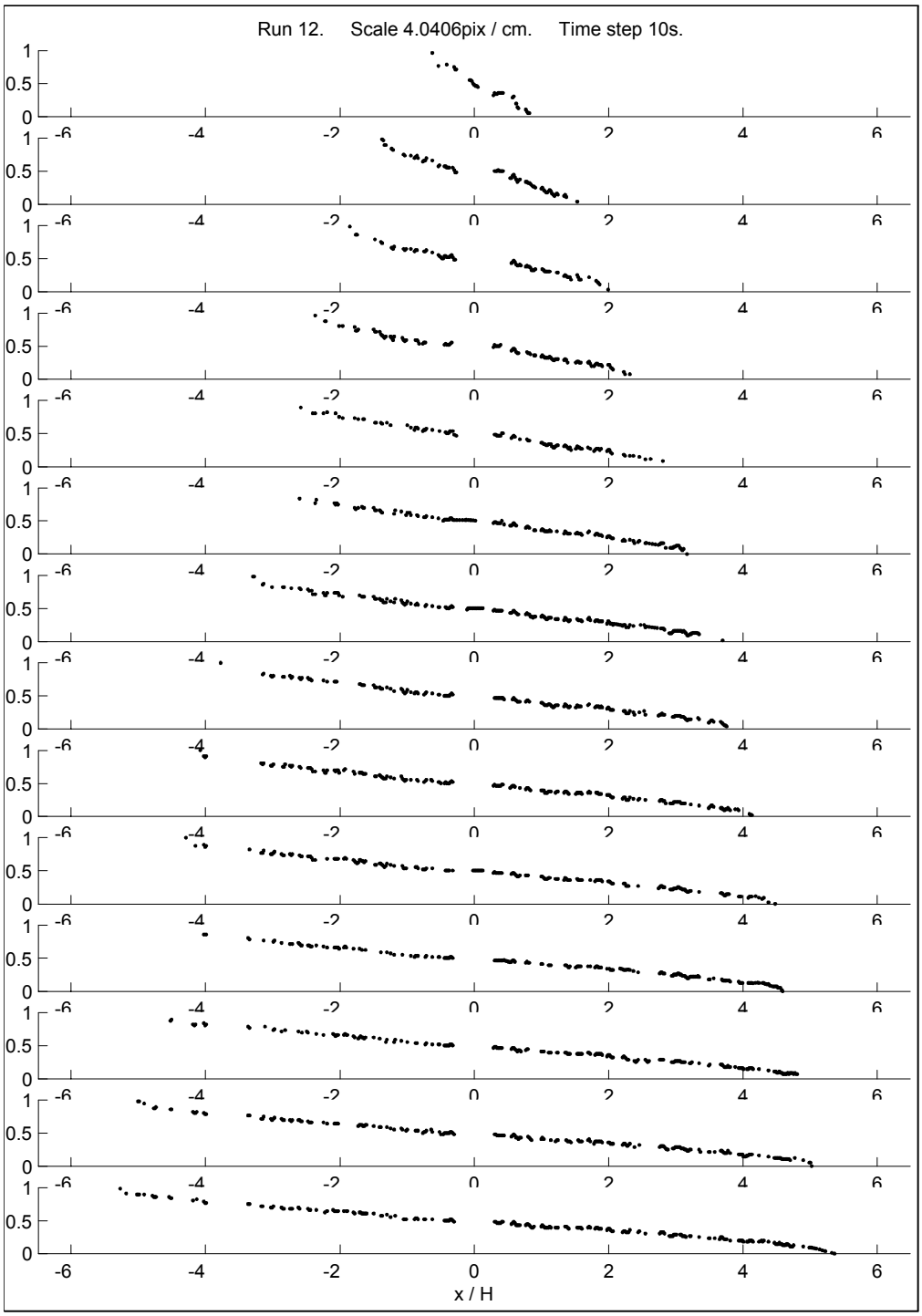

Figure C-11: Run 12.

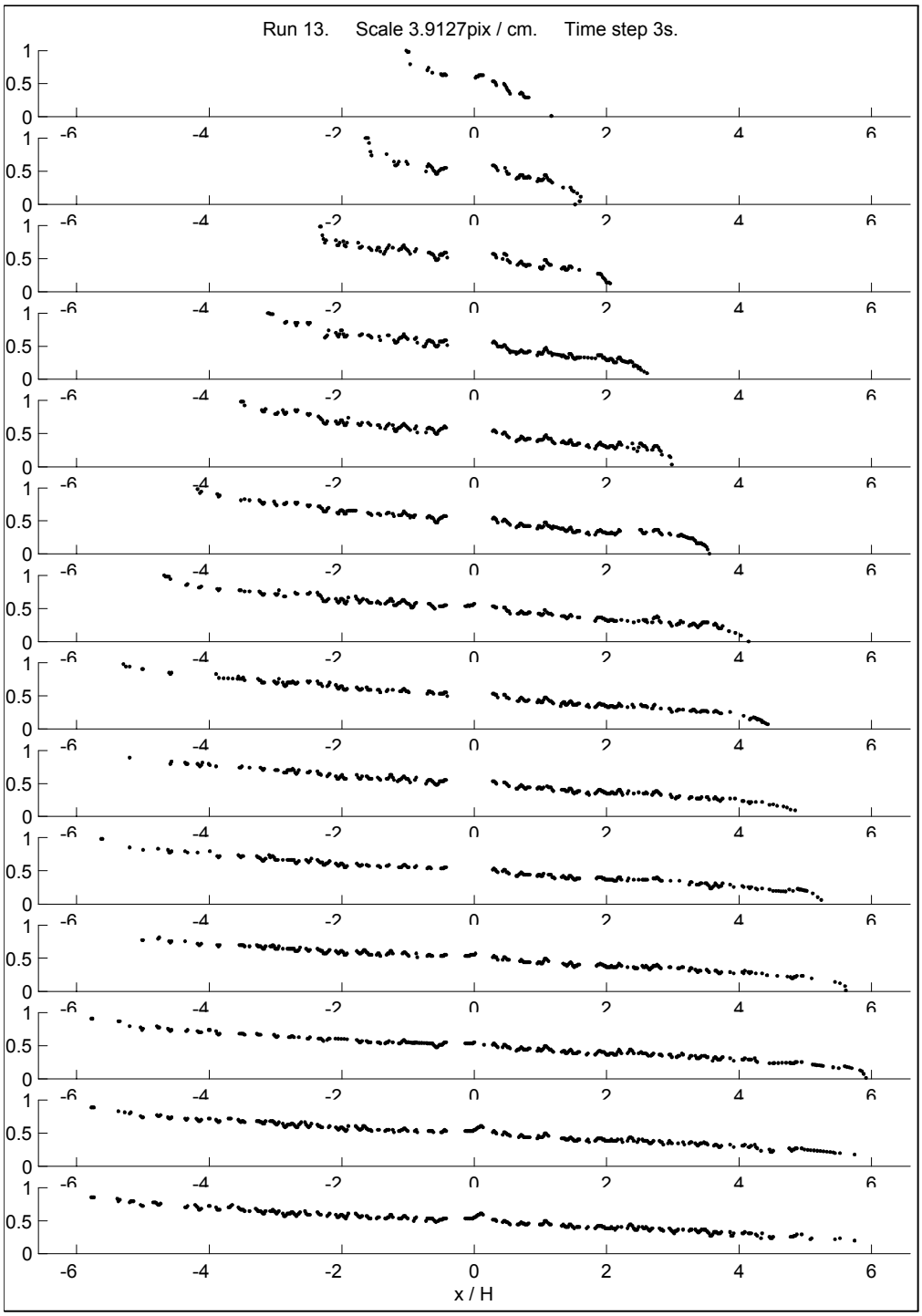

Figure C-12: Run 13.

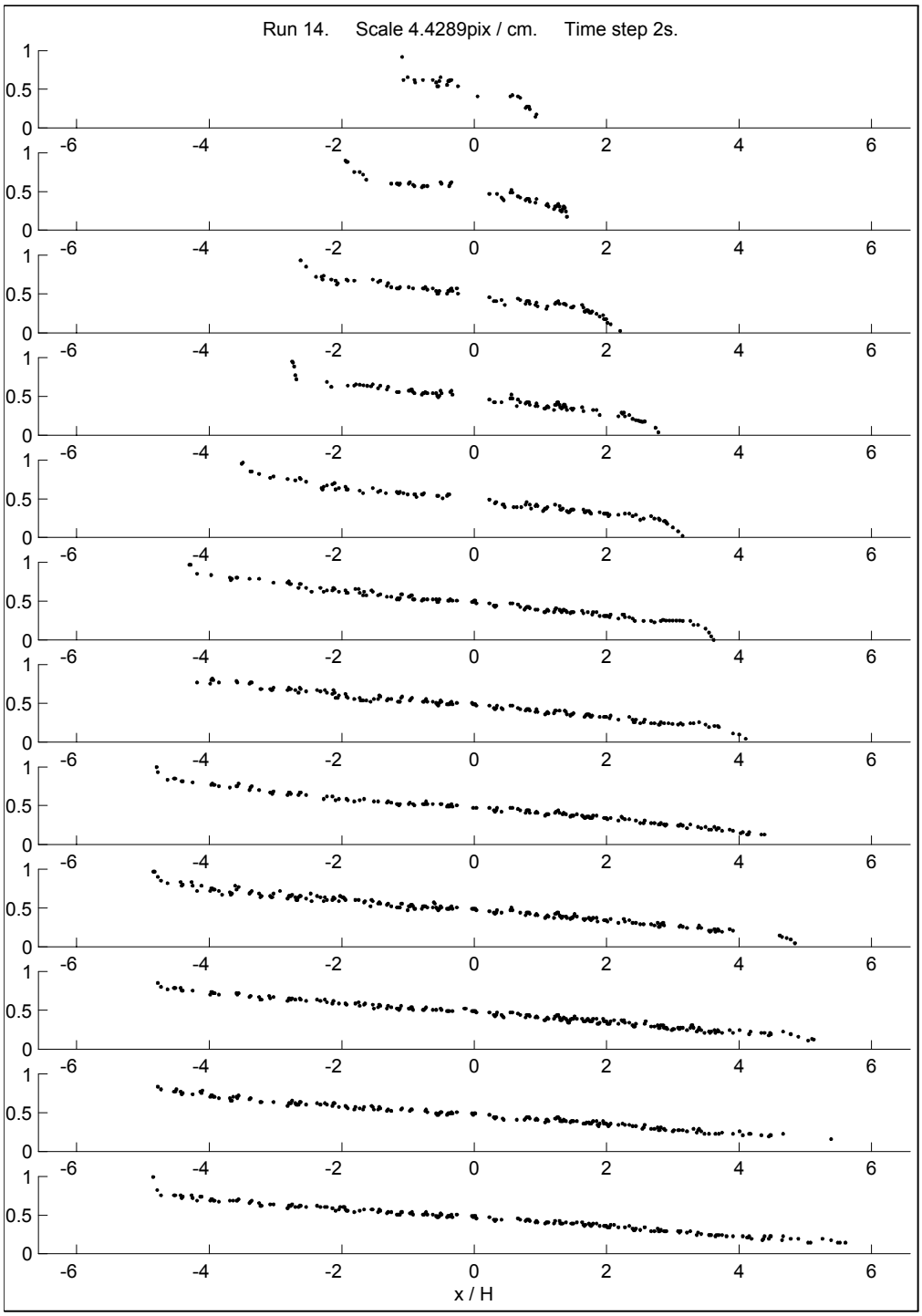

Figure C-13: Run 14.

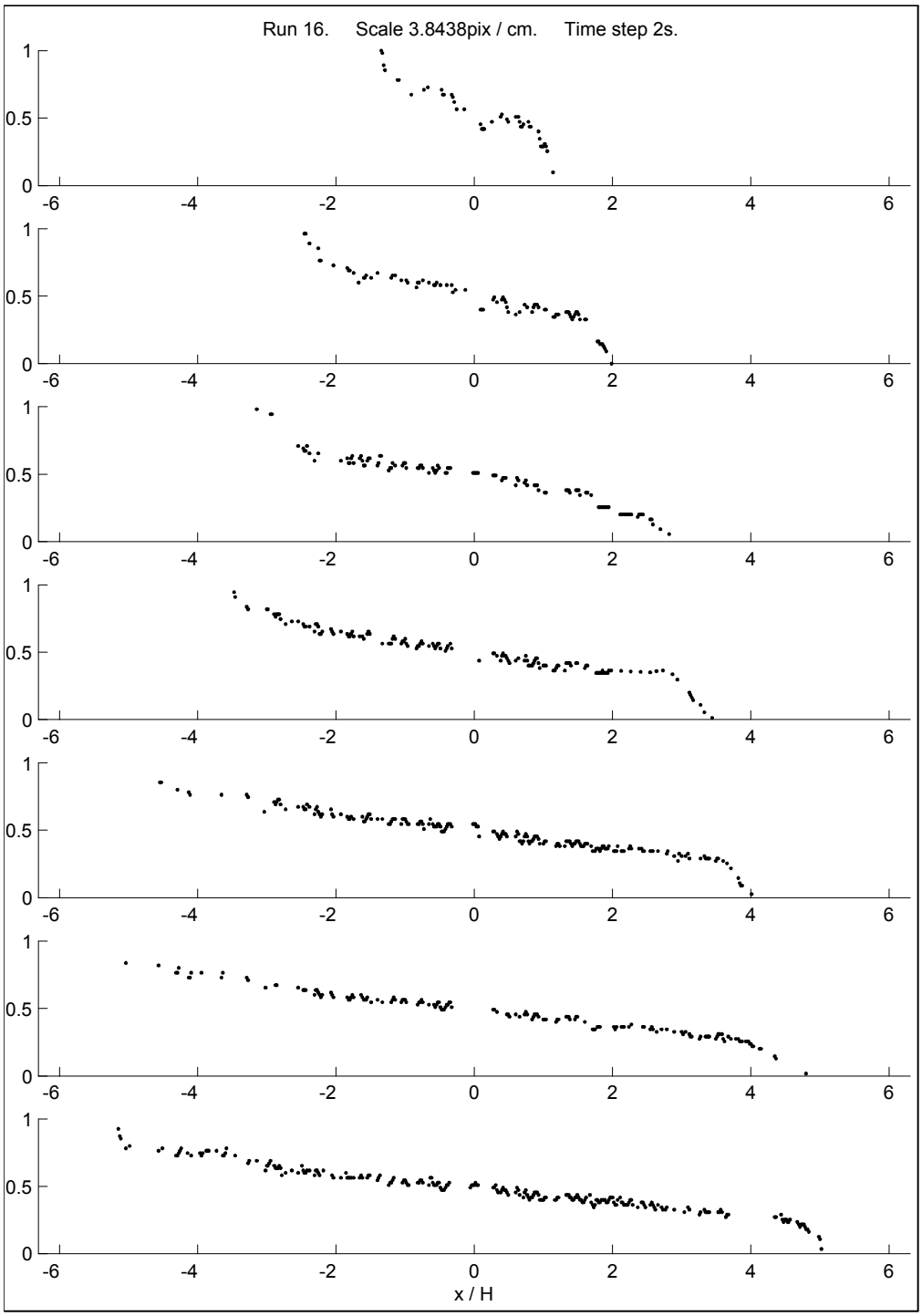

Figure C-14: Run 16.

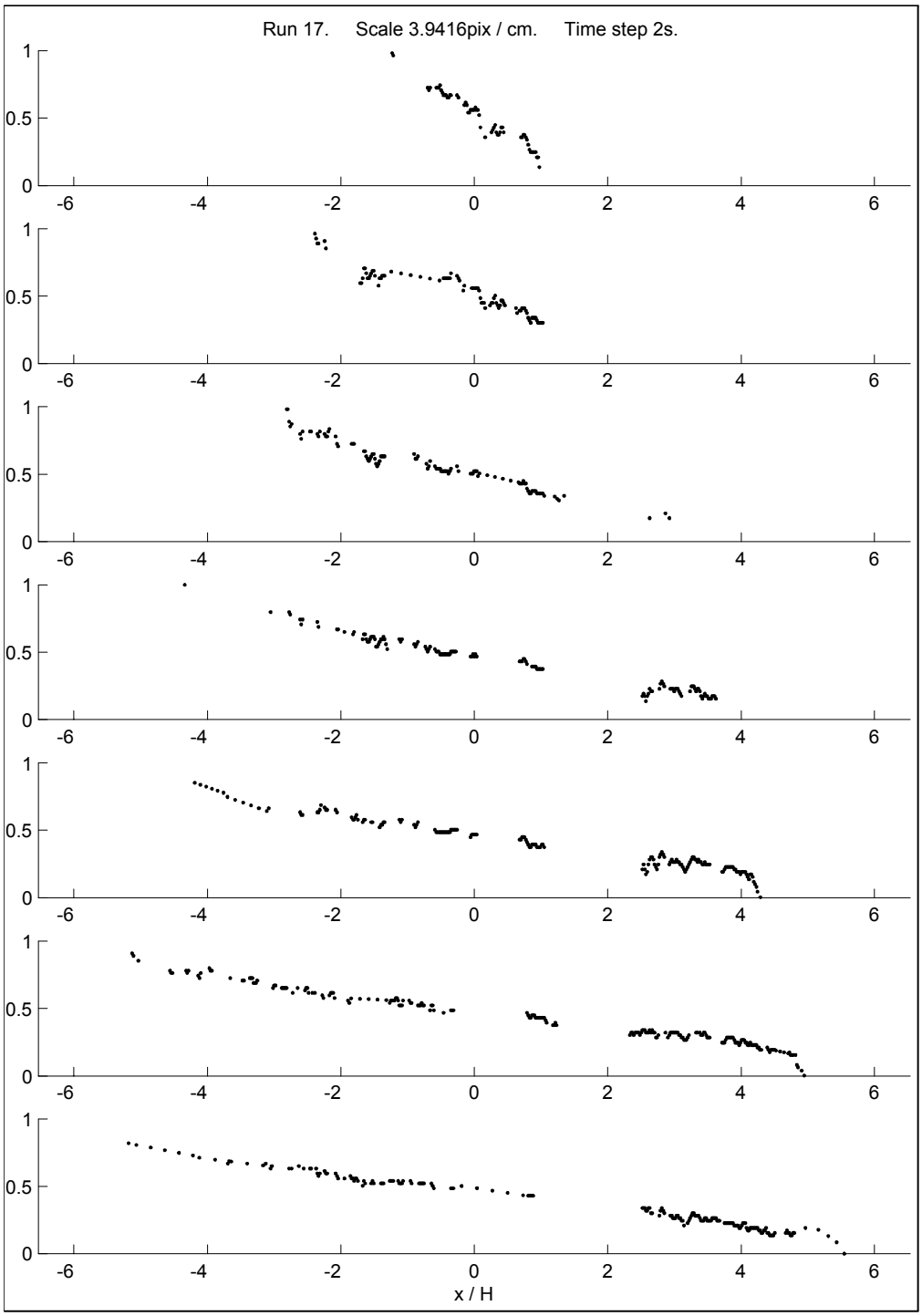

Figure C-15: Run 17.

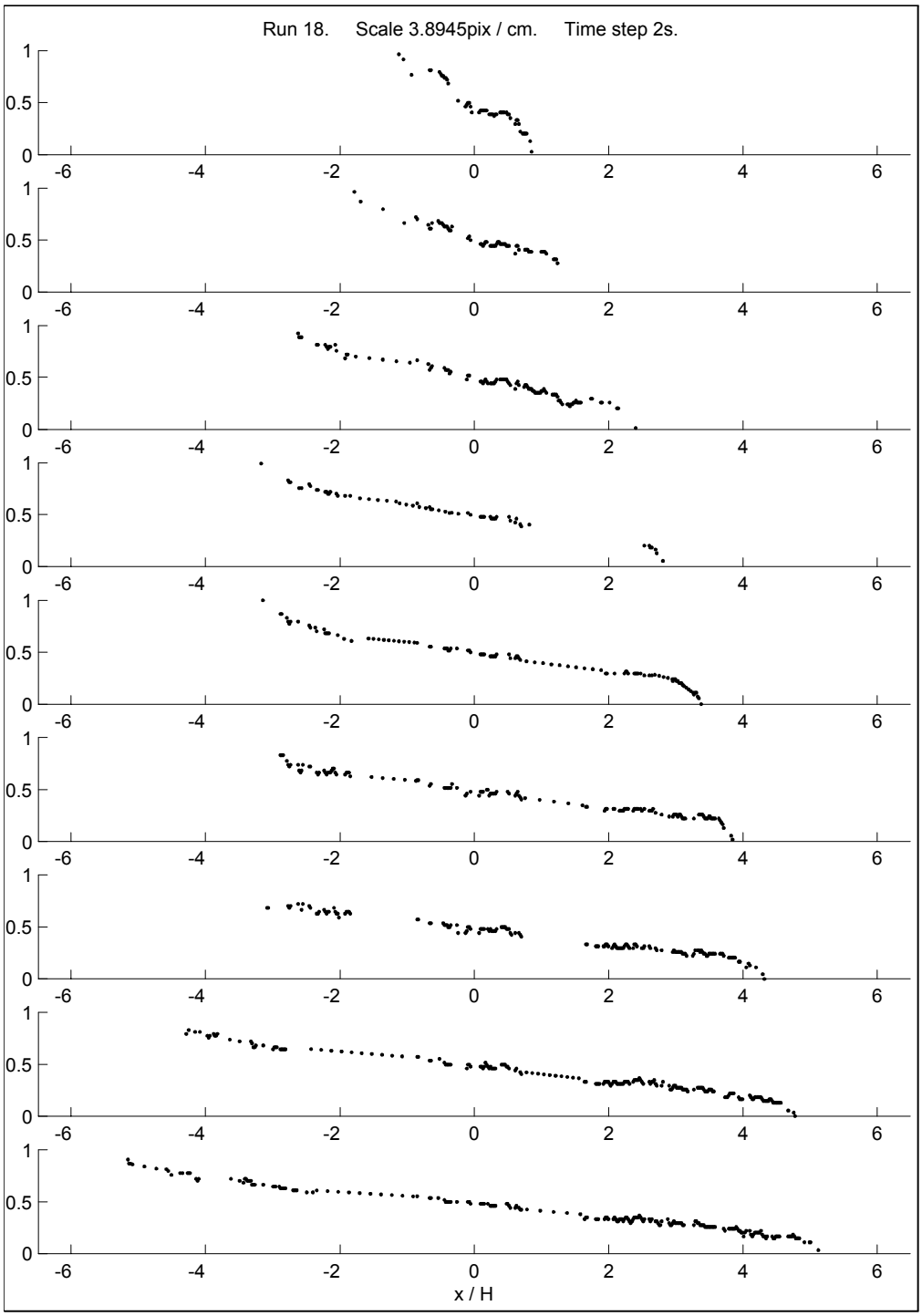

Figure C-16: Run 18.

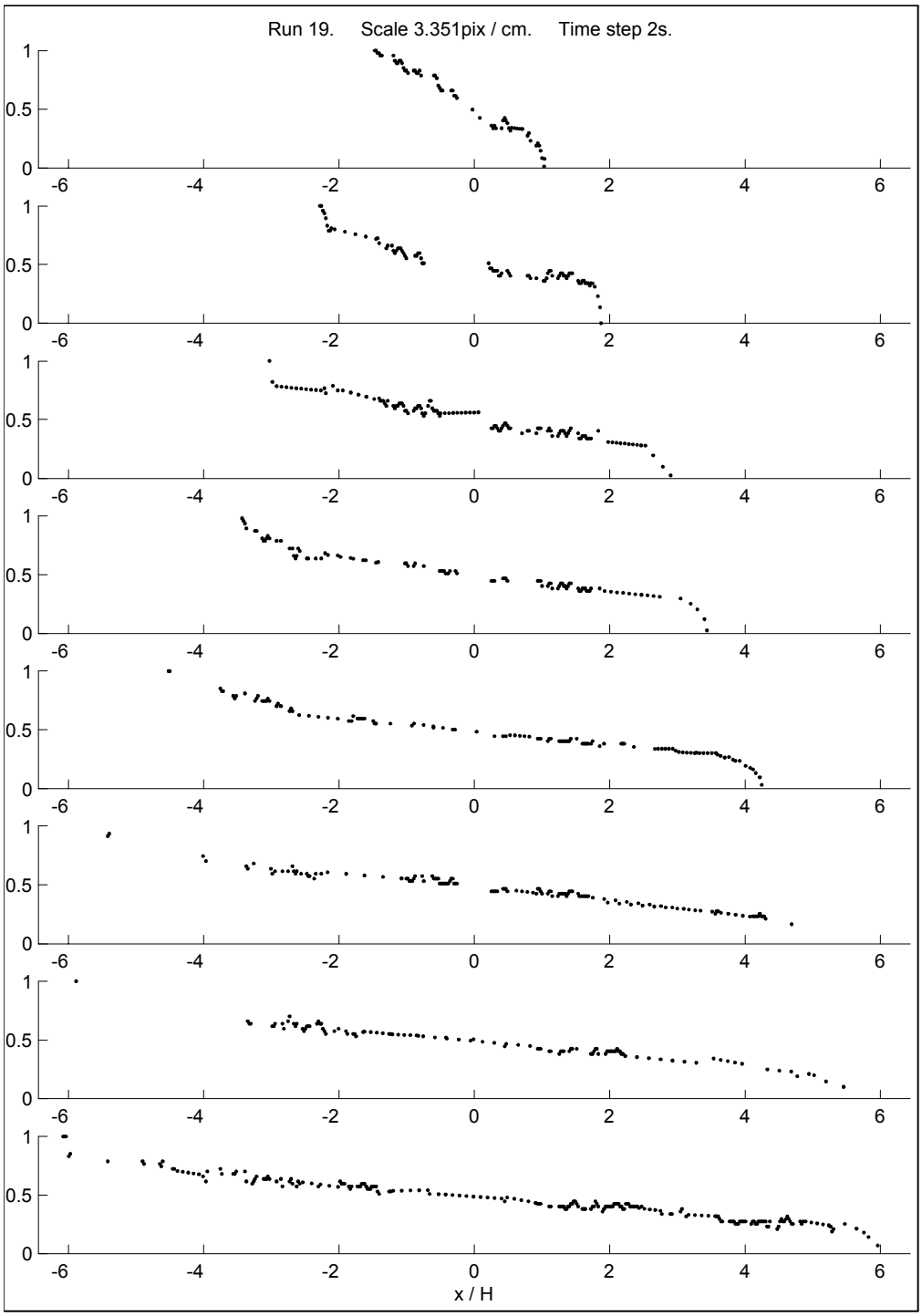

Figure C-17: Run 19.

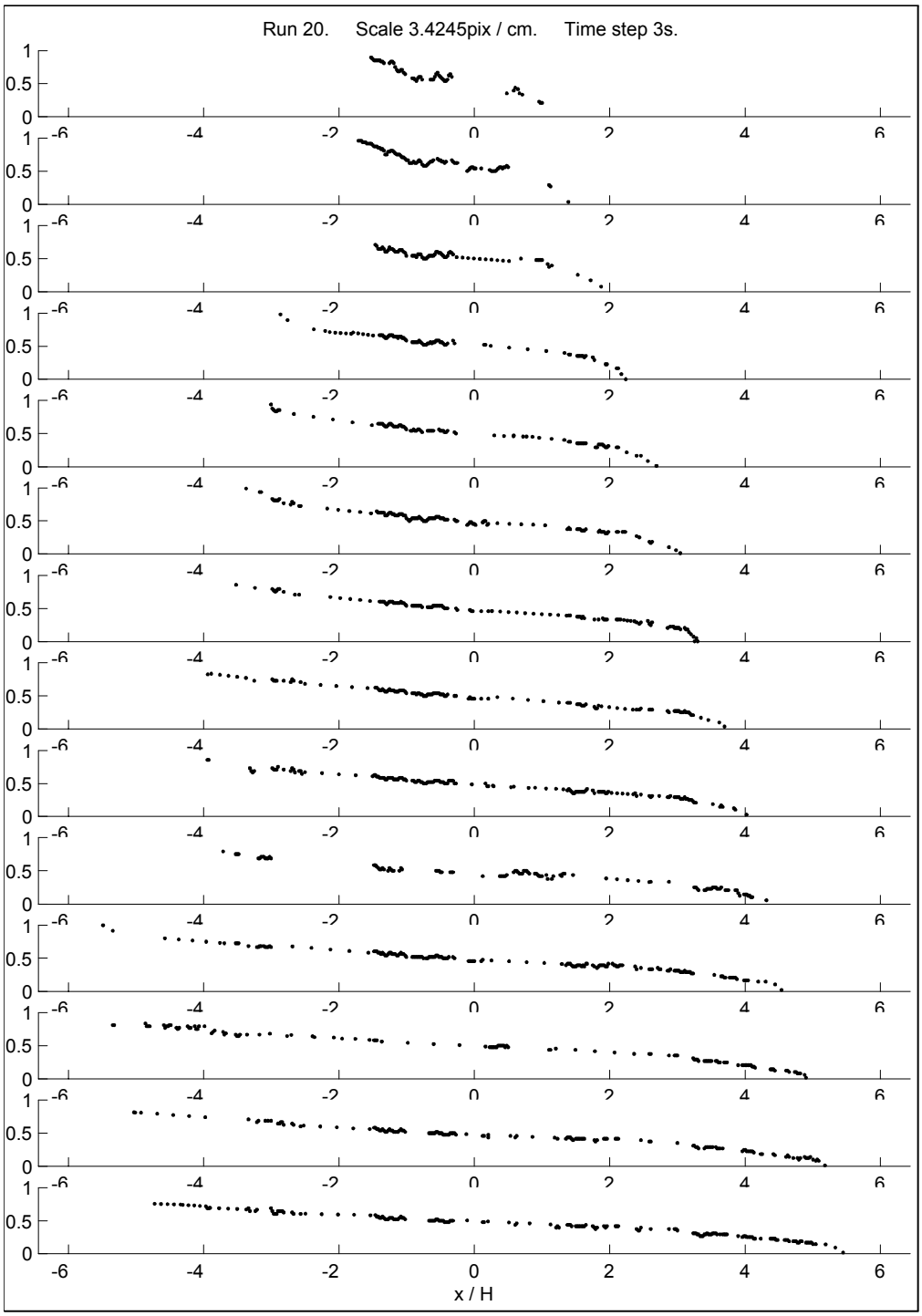

Figure C-18: Run 20.

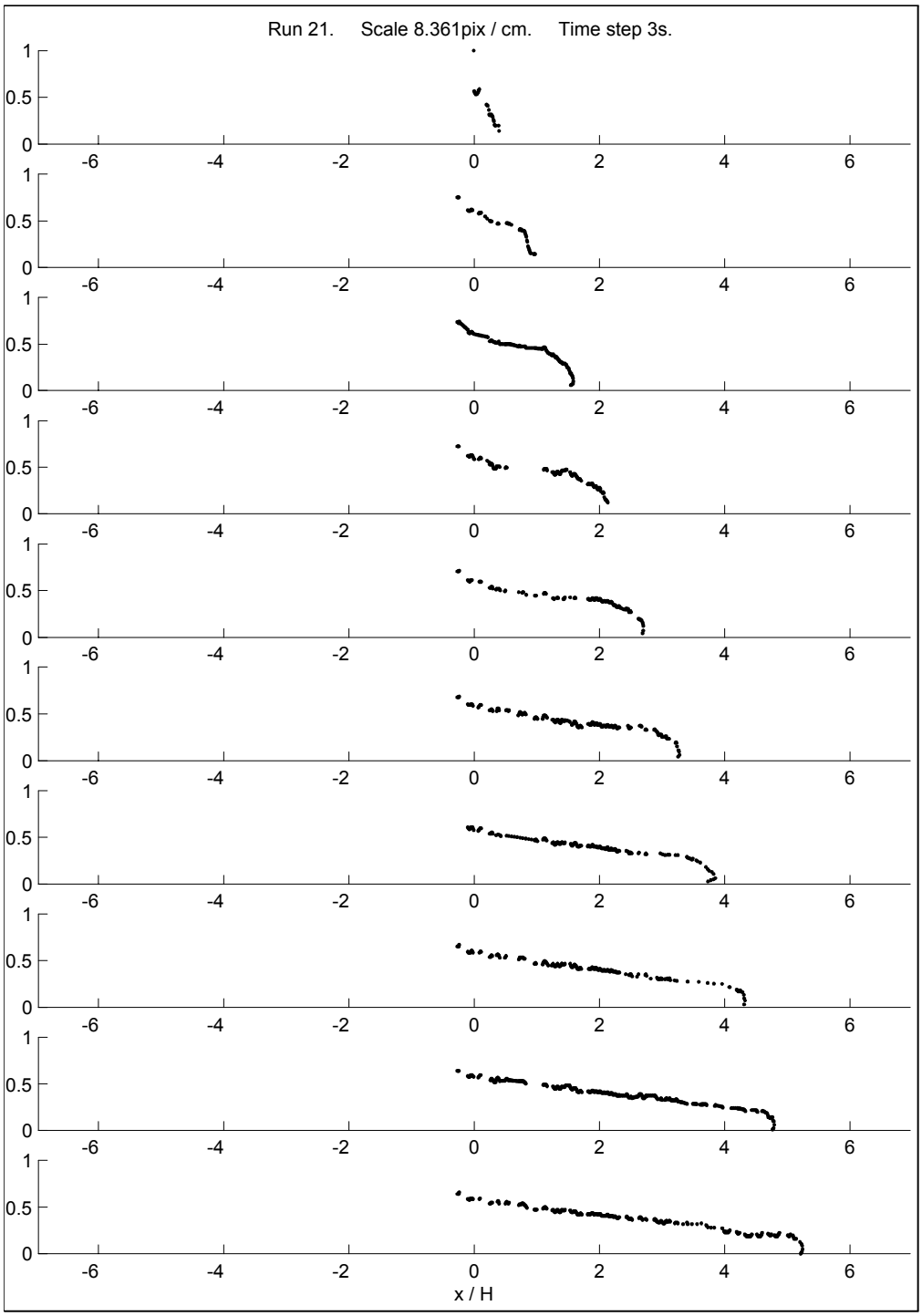

Figure C-19: Run 21.

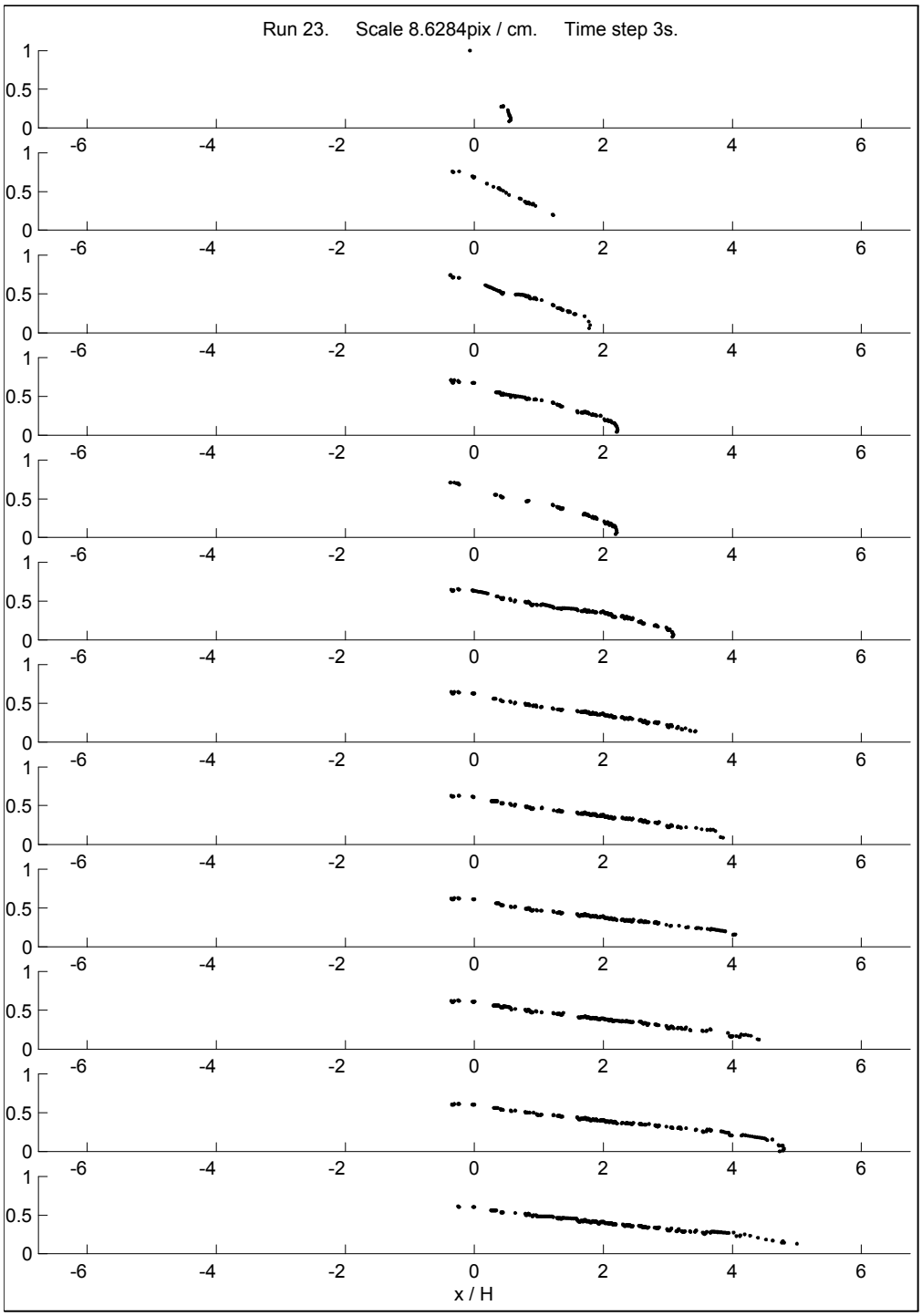

Figure C-20: Run 23.

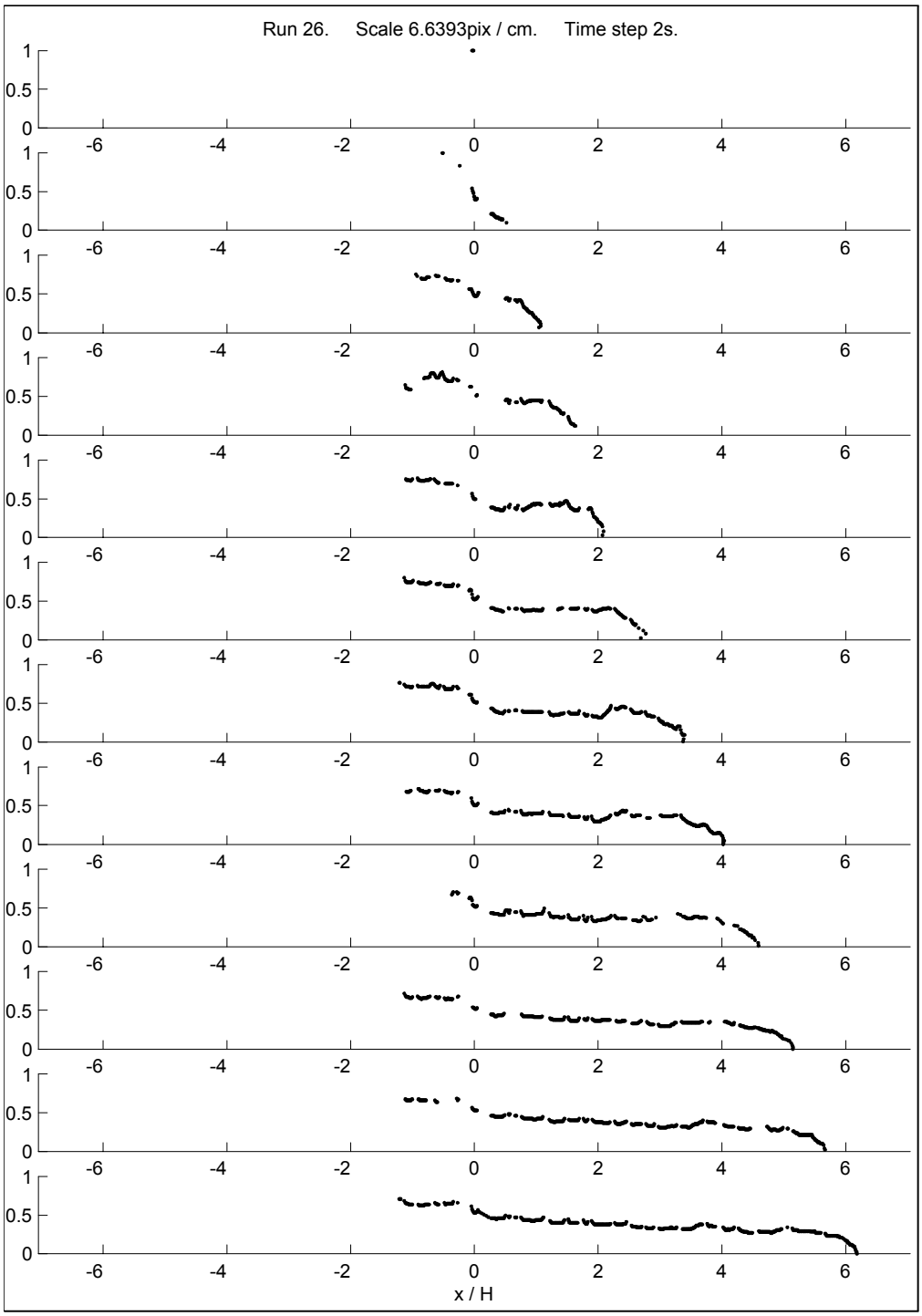

Figure C-21: Run 26.

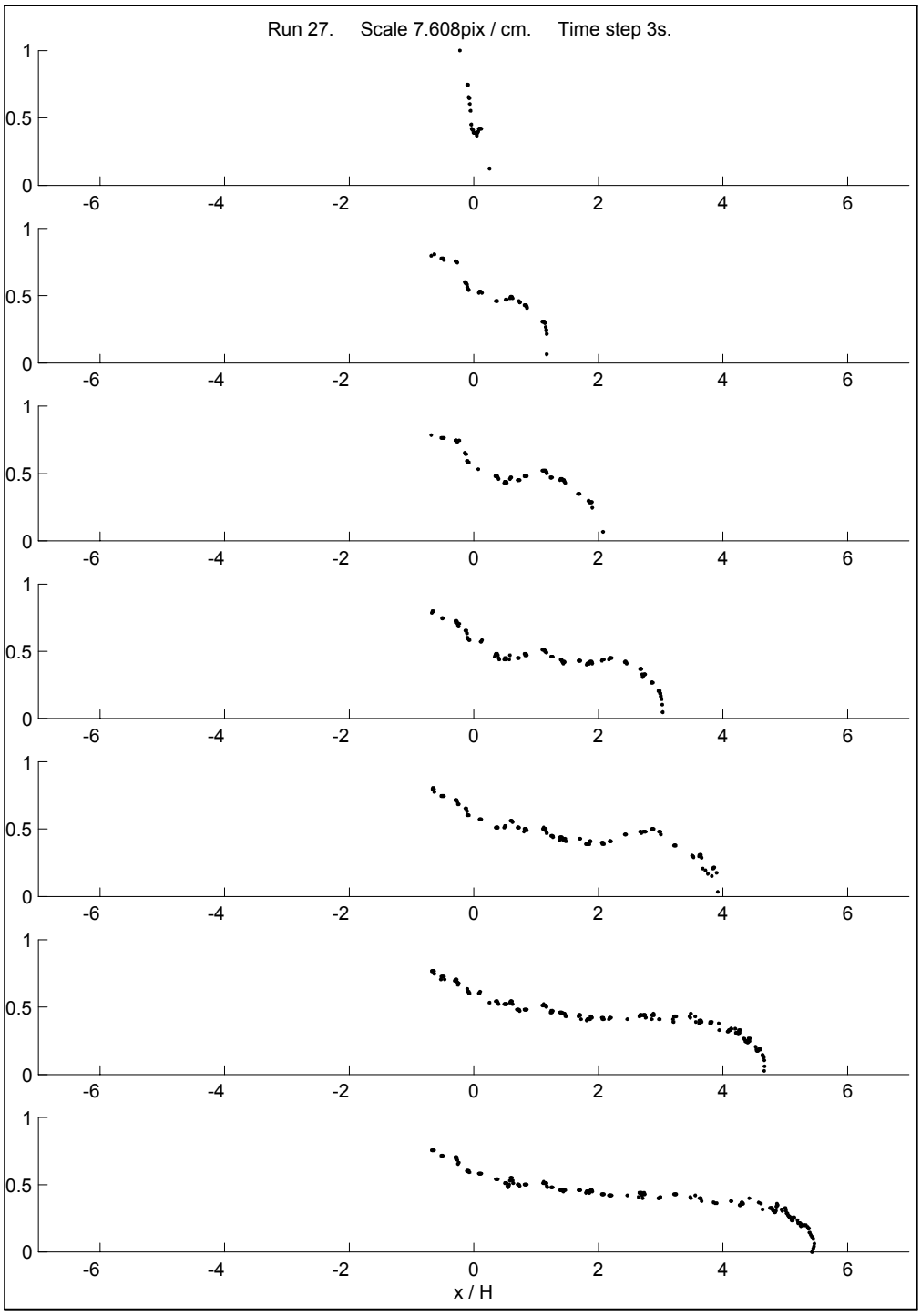

Figure C-22: Run 27.

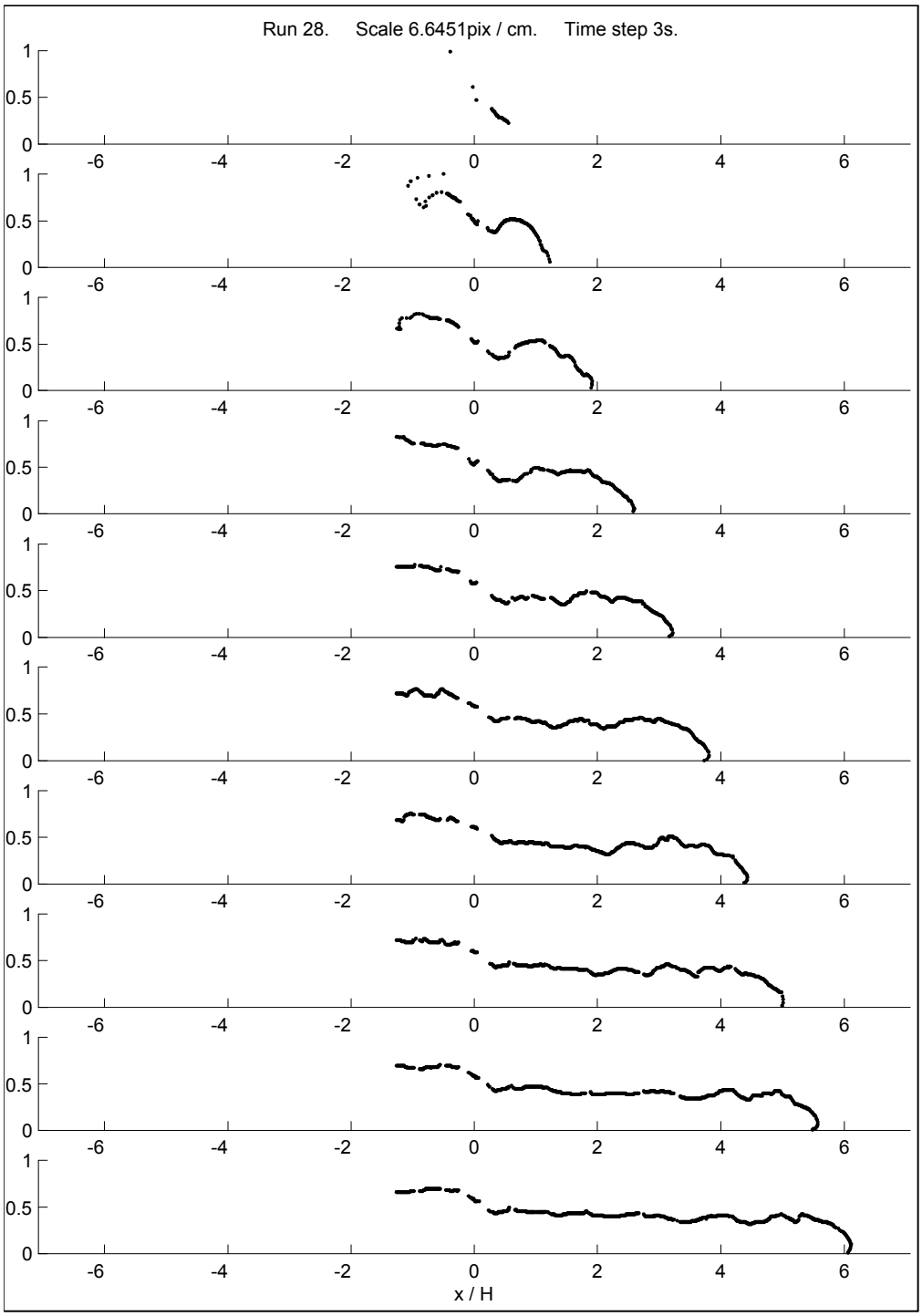

Figure C-23: Run 28.

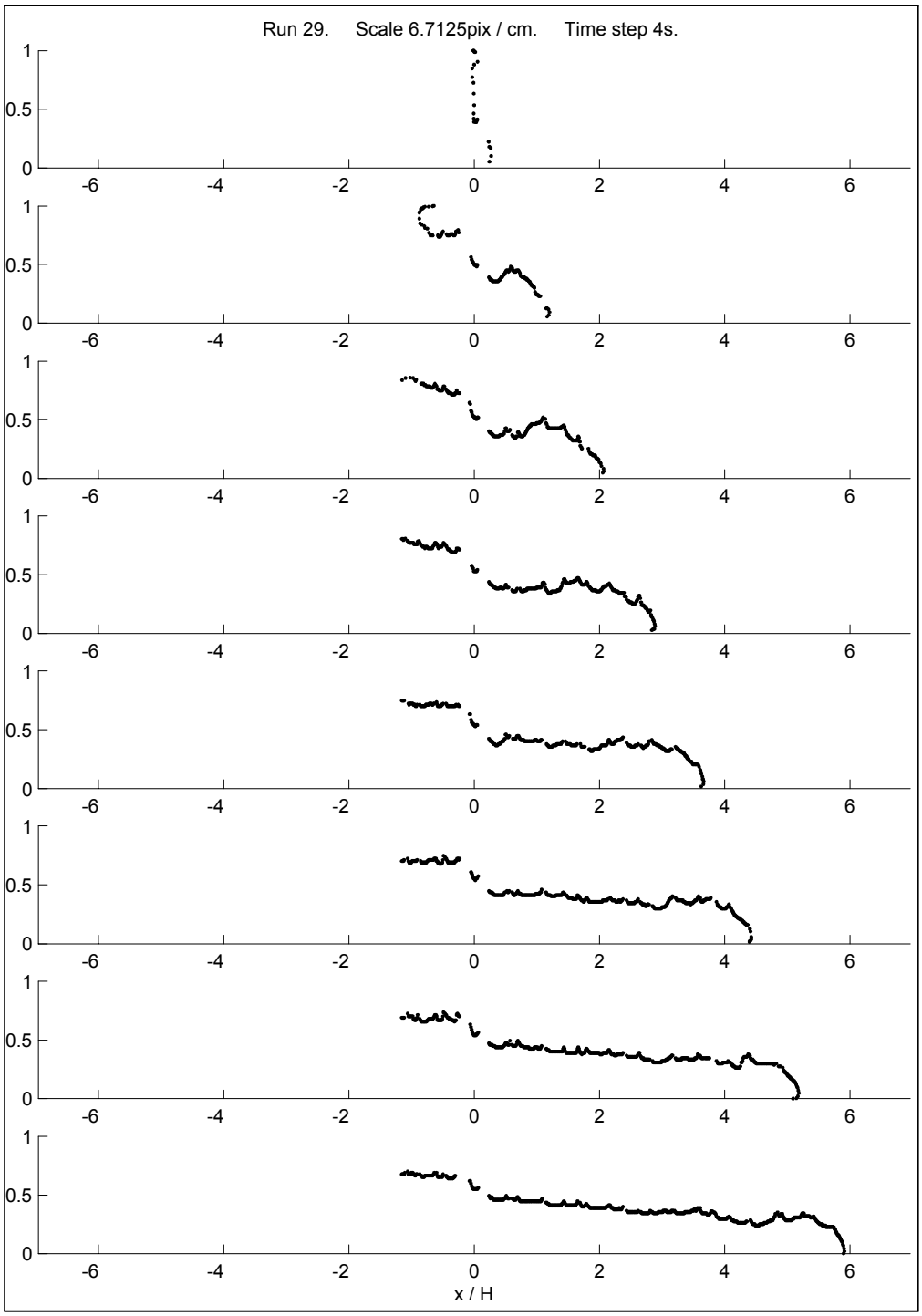

Figure C-24: Run 29.

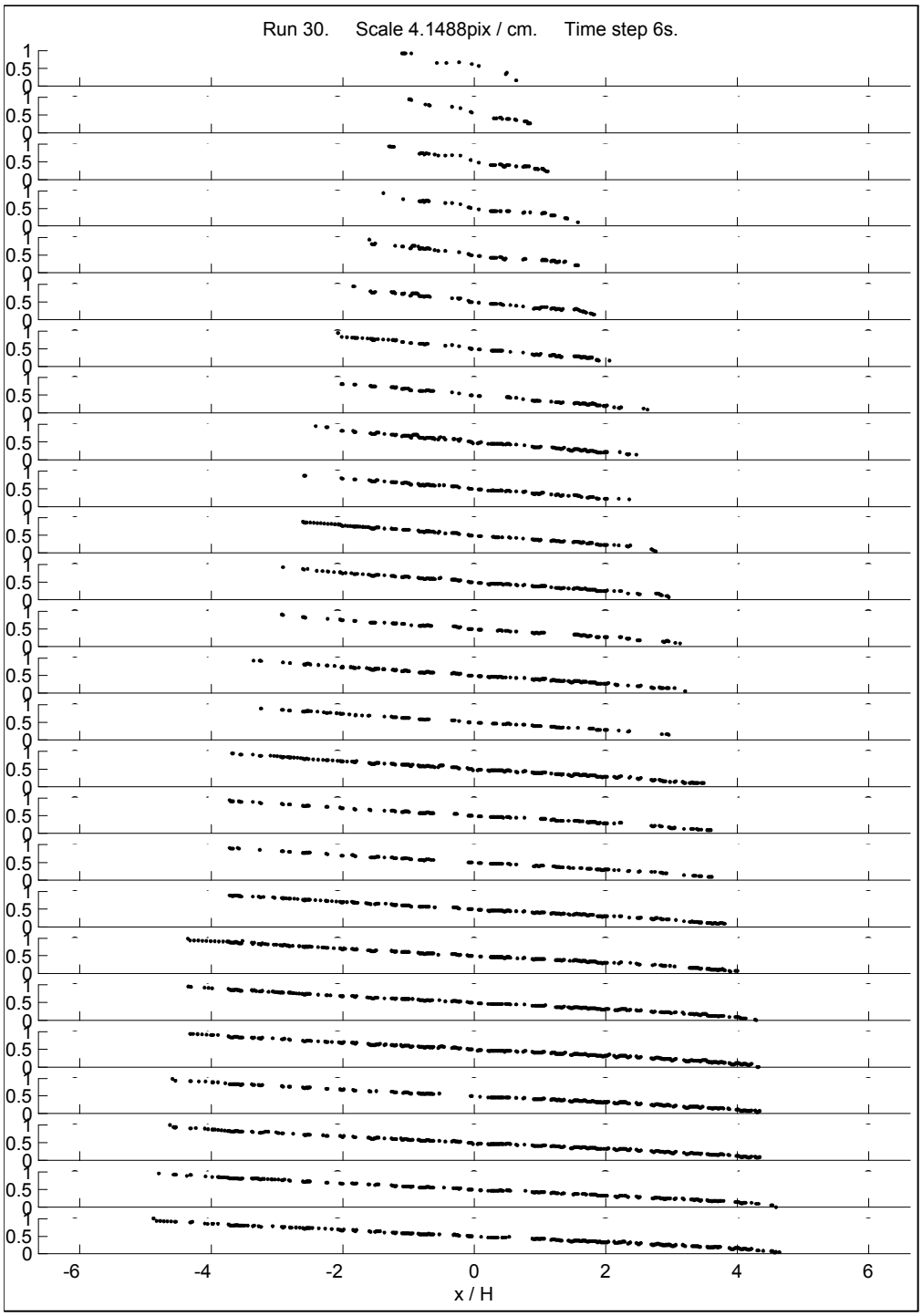

Figure C-25: Run 30.

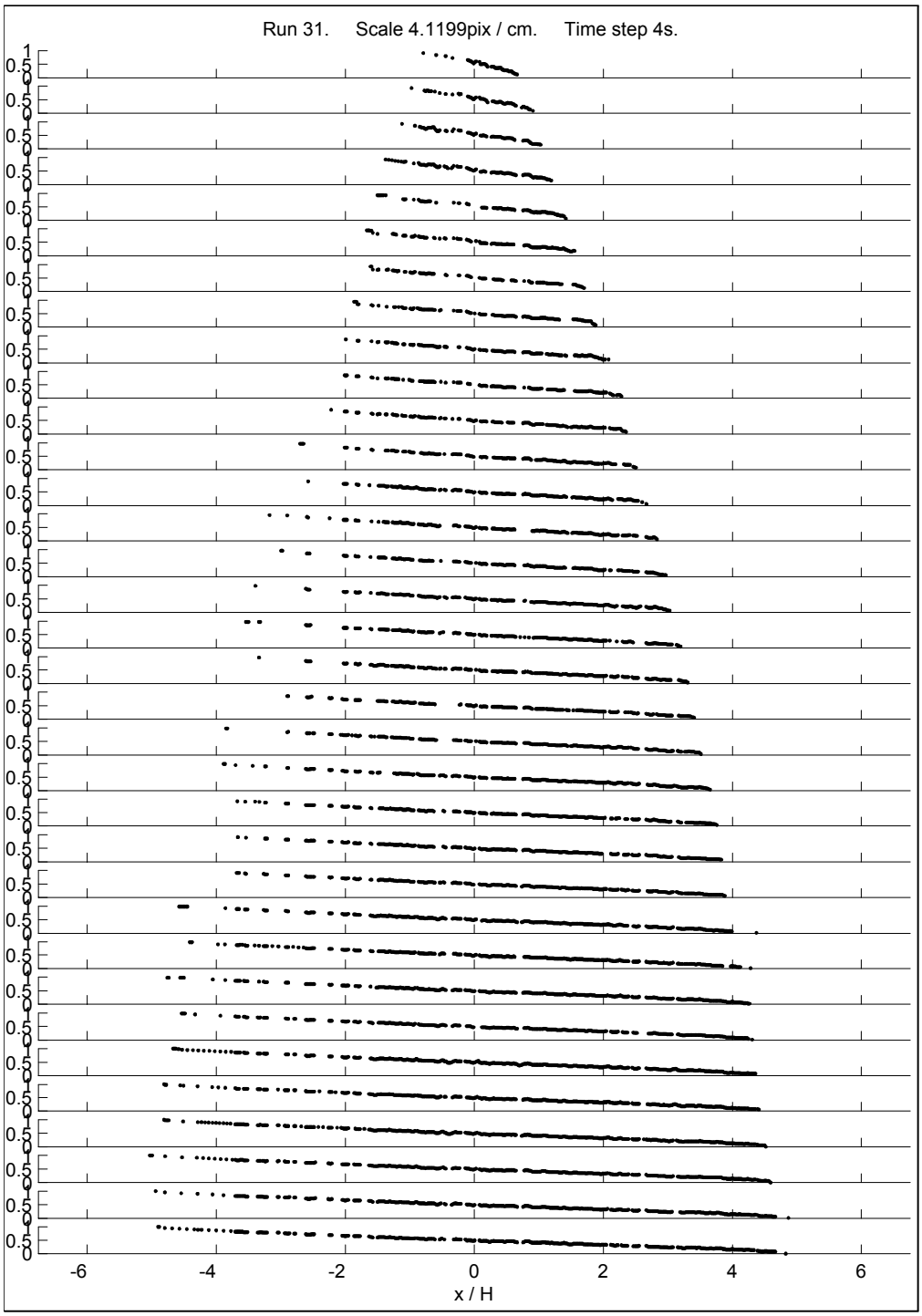

Figure C-26: Run 31.

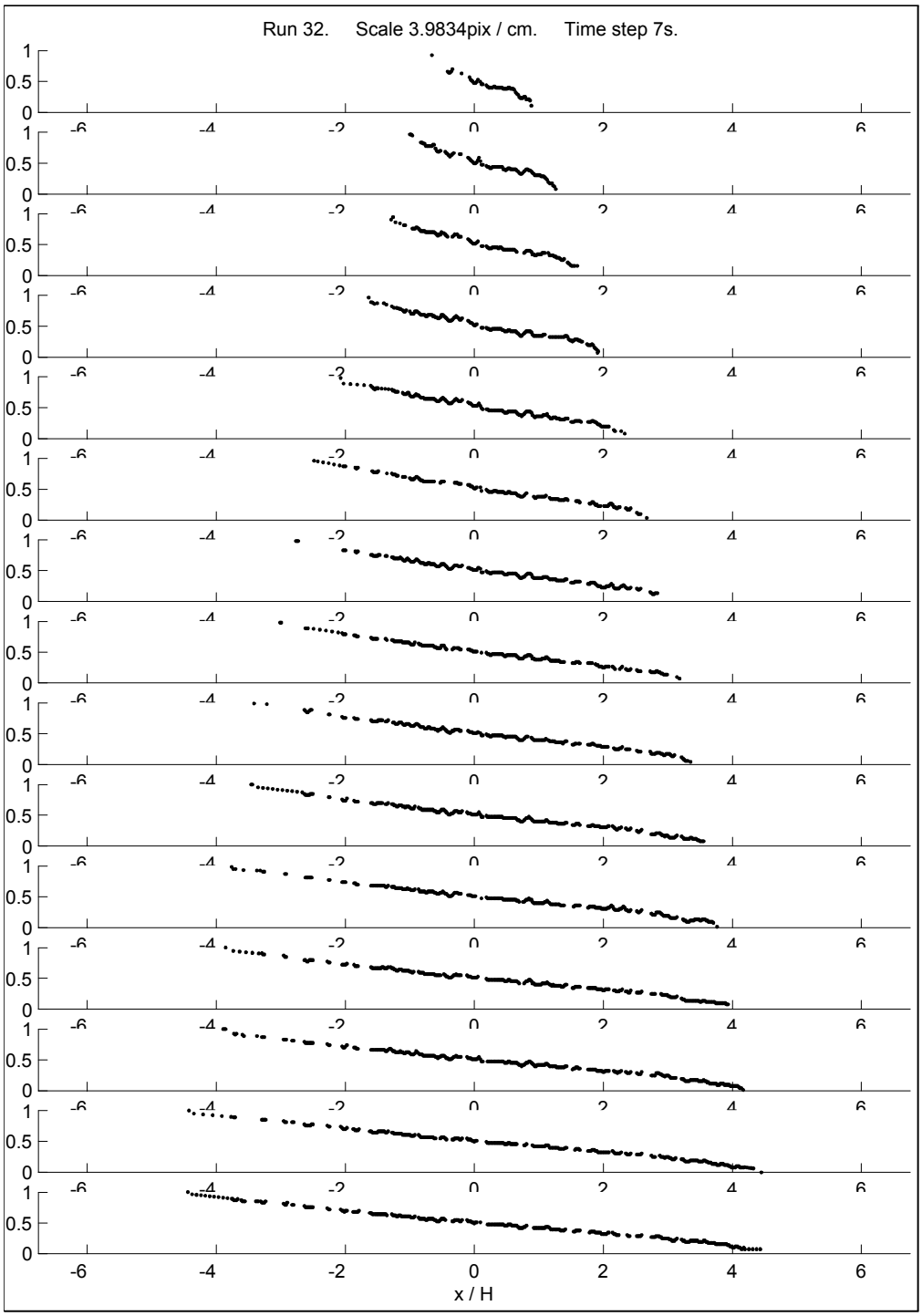

Figure C-27: Run 32.

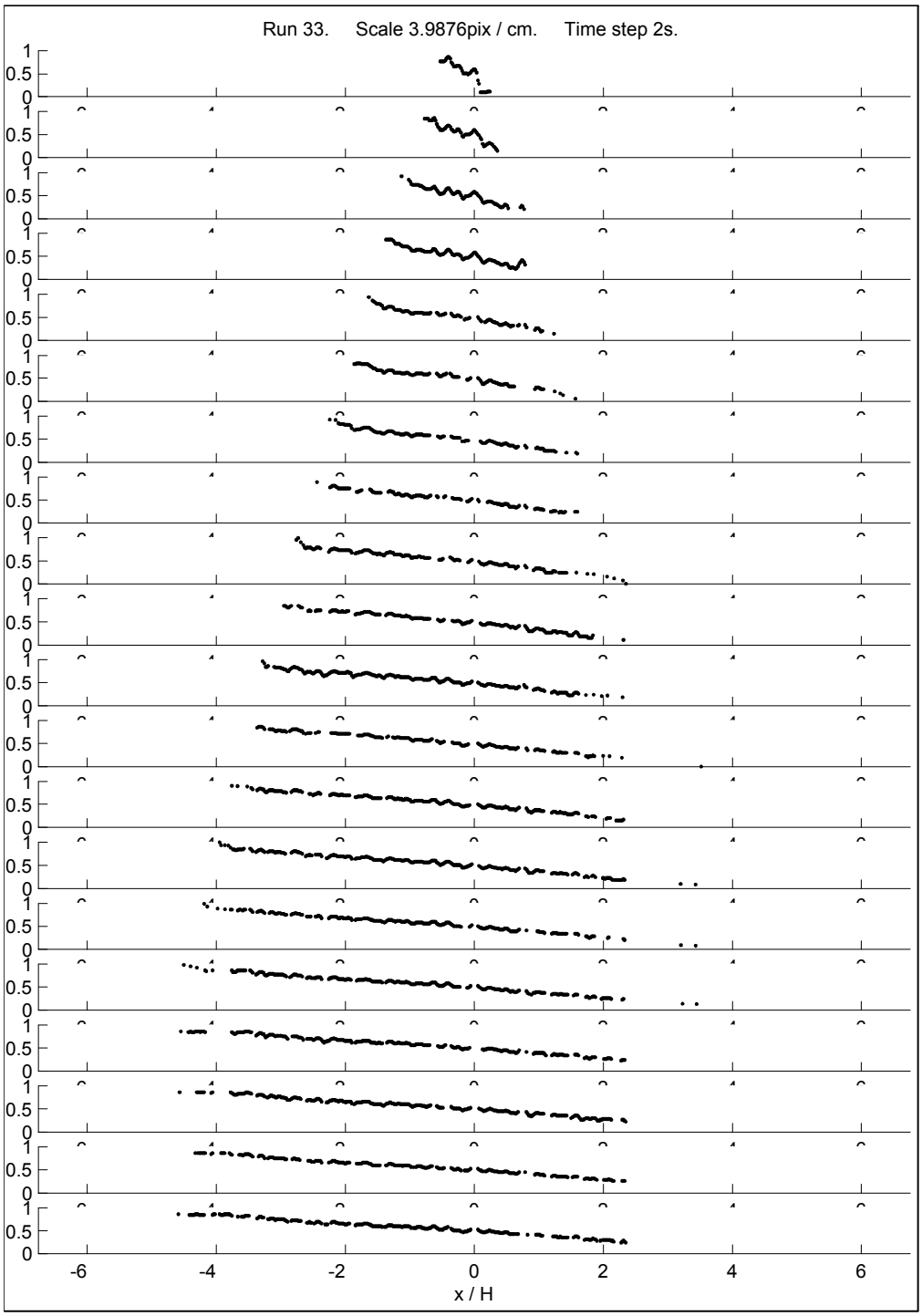

Figure C-28: Run 33.

Figure C-29: Run 34.

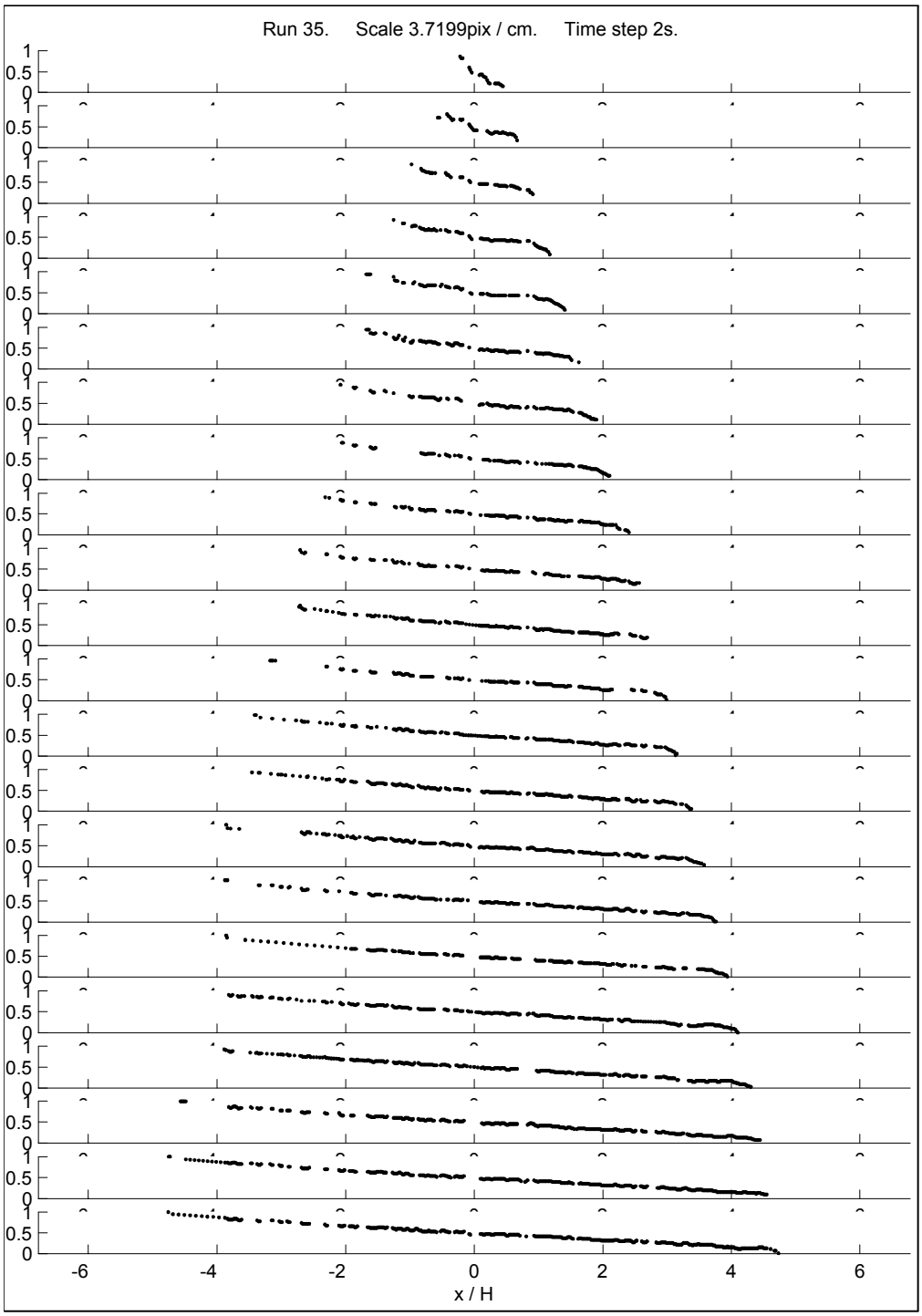

Figure C-30: Run 35.

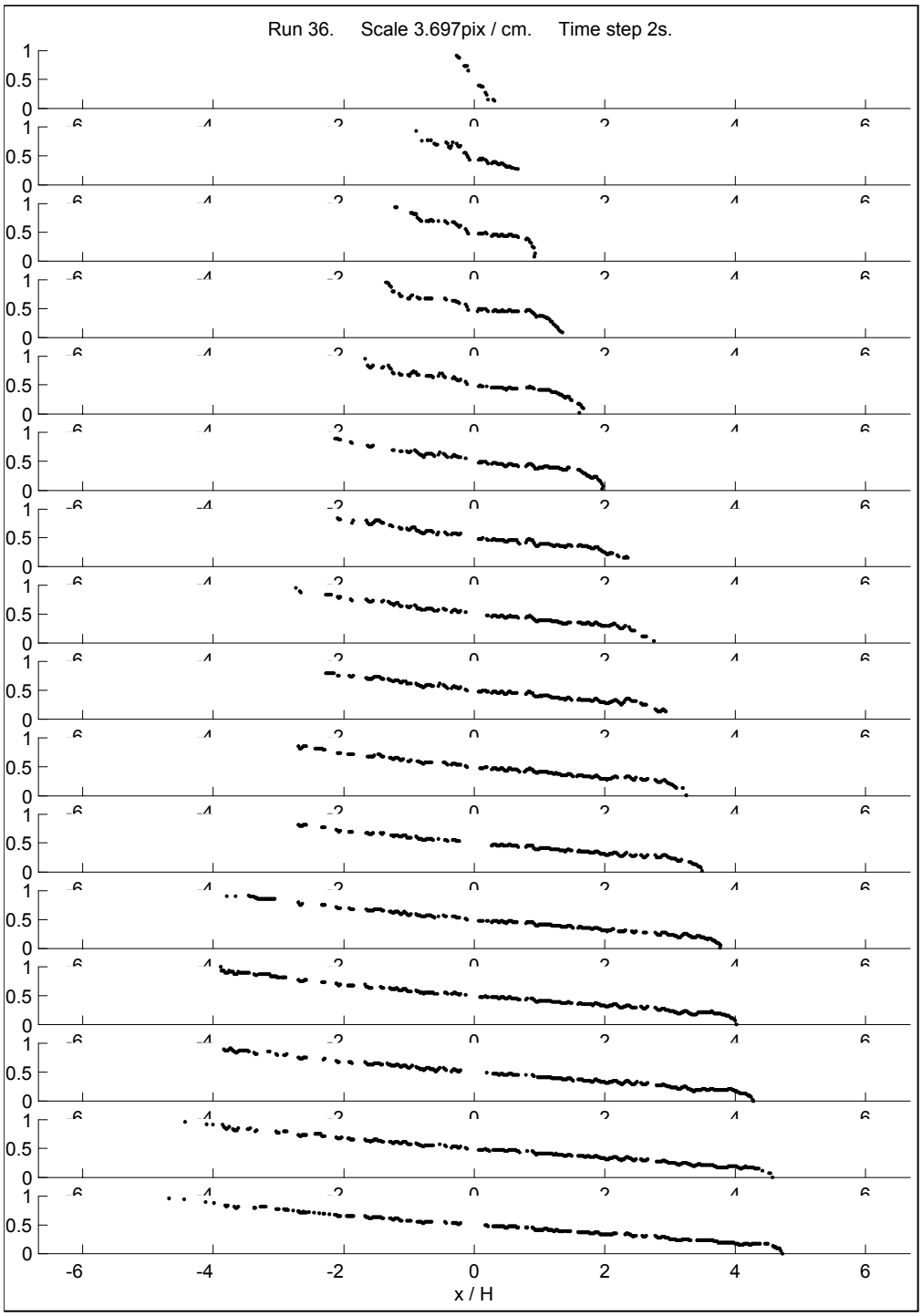

Figure C-31: Run 36.

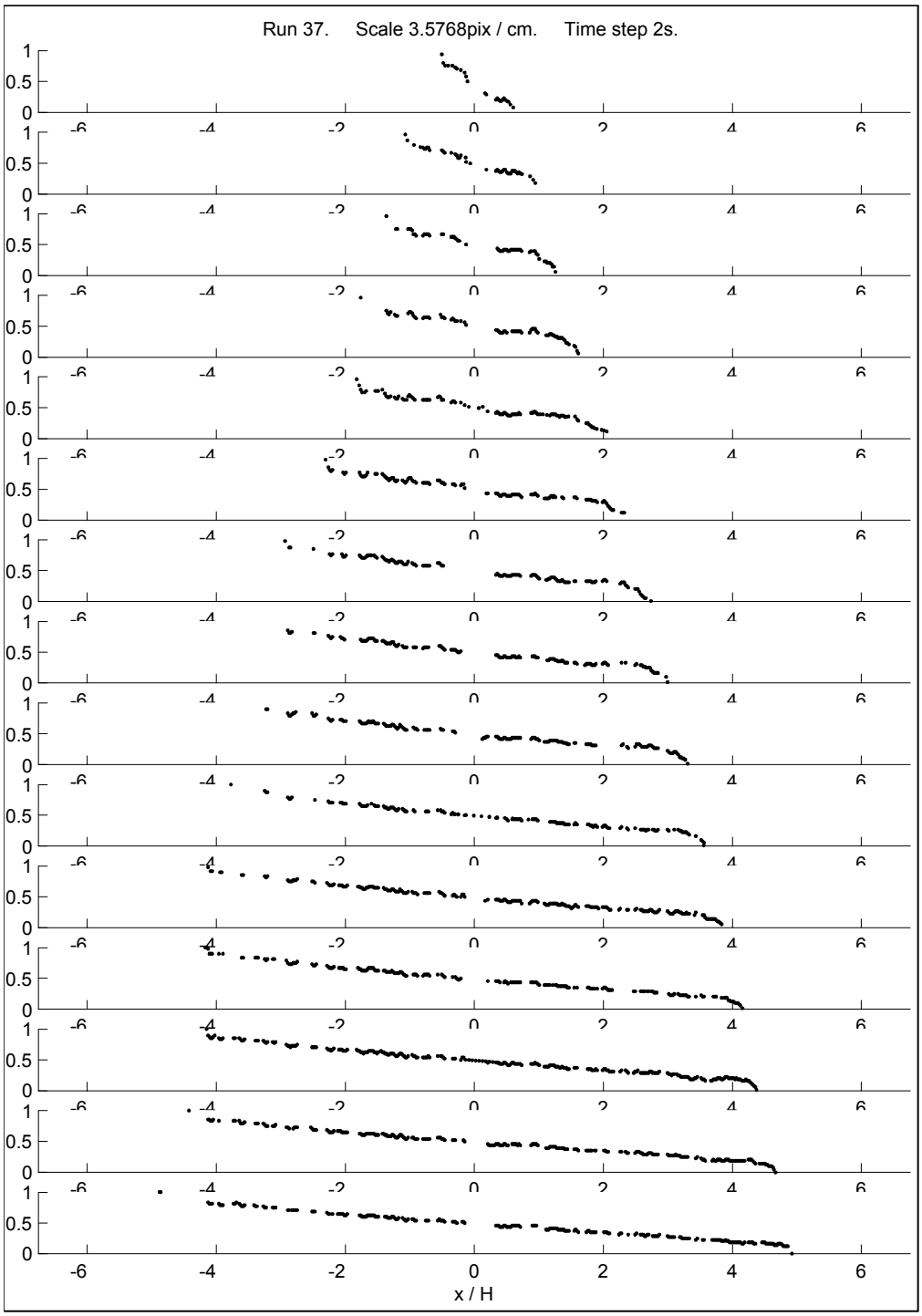

Figure C-32: Run 37.

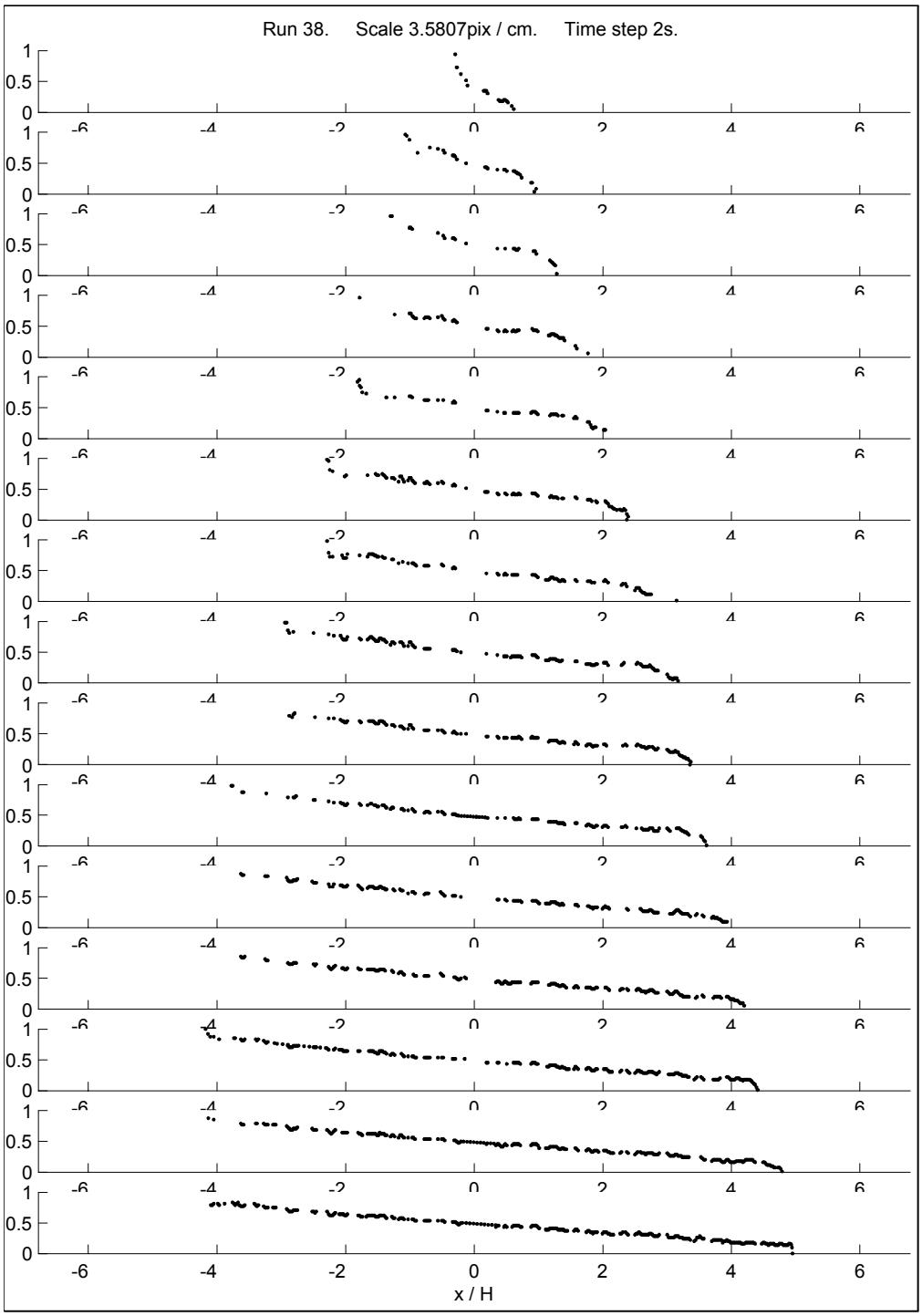

Figure C-33: Run 38.

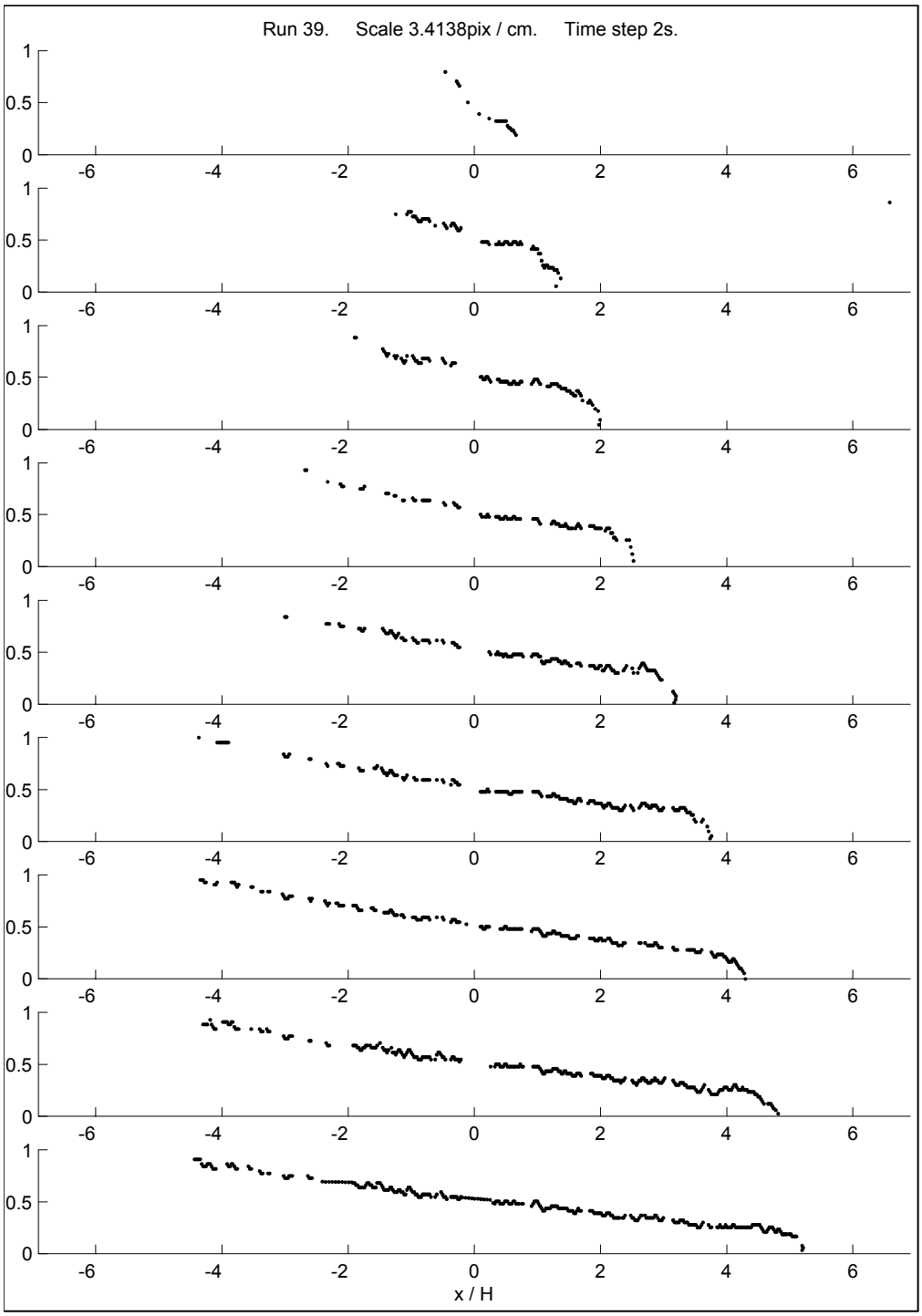

Figure C-34: Run 39.

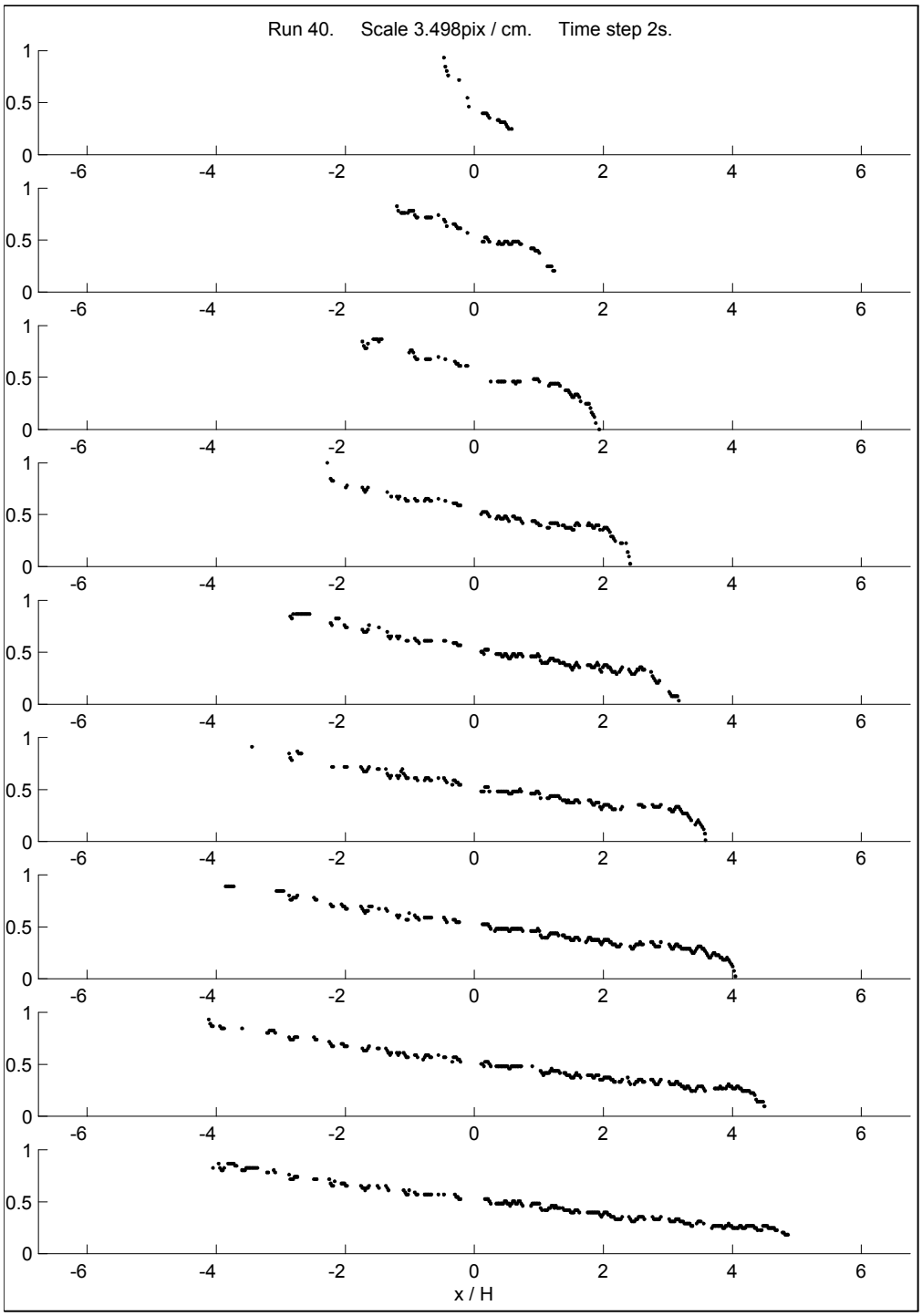

Figure C-35: Run 40.

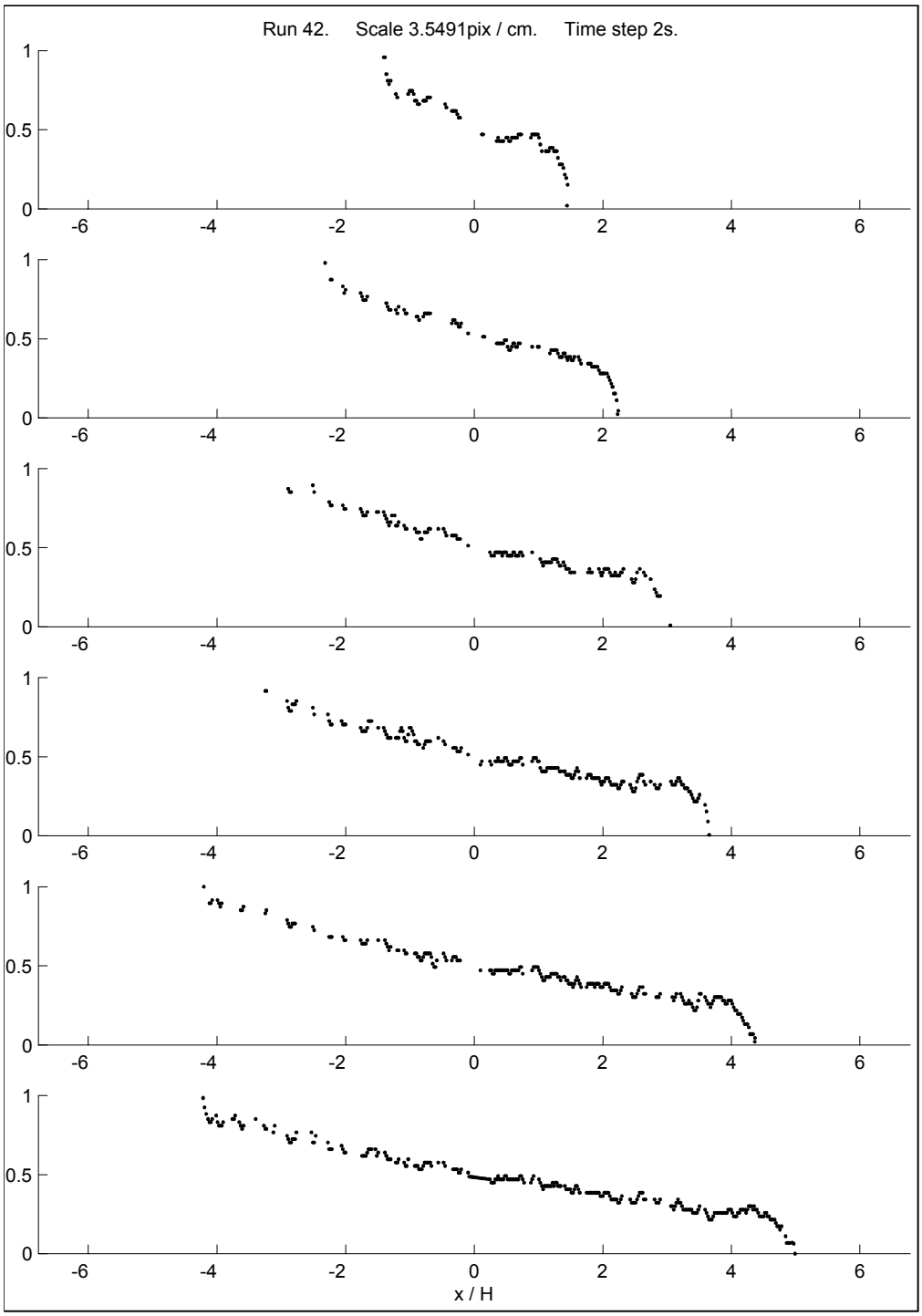

Figure C-36: Run 42.

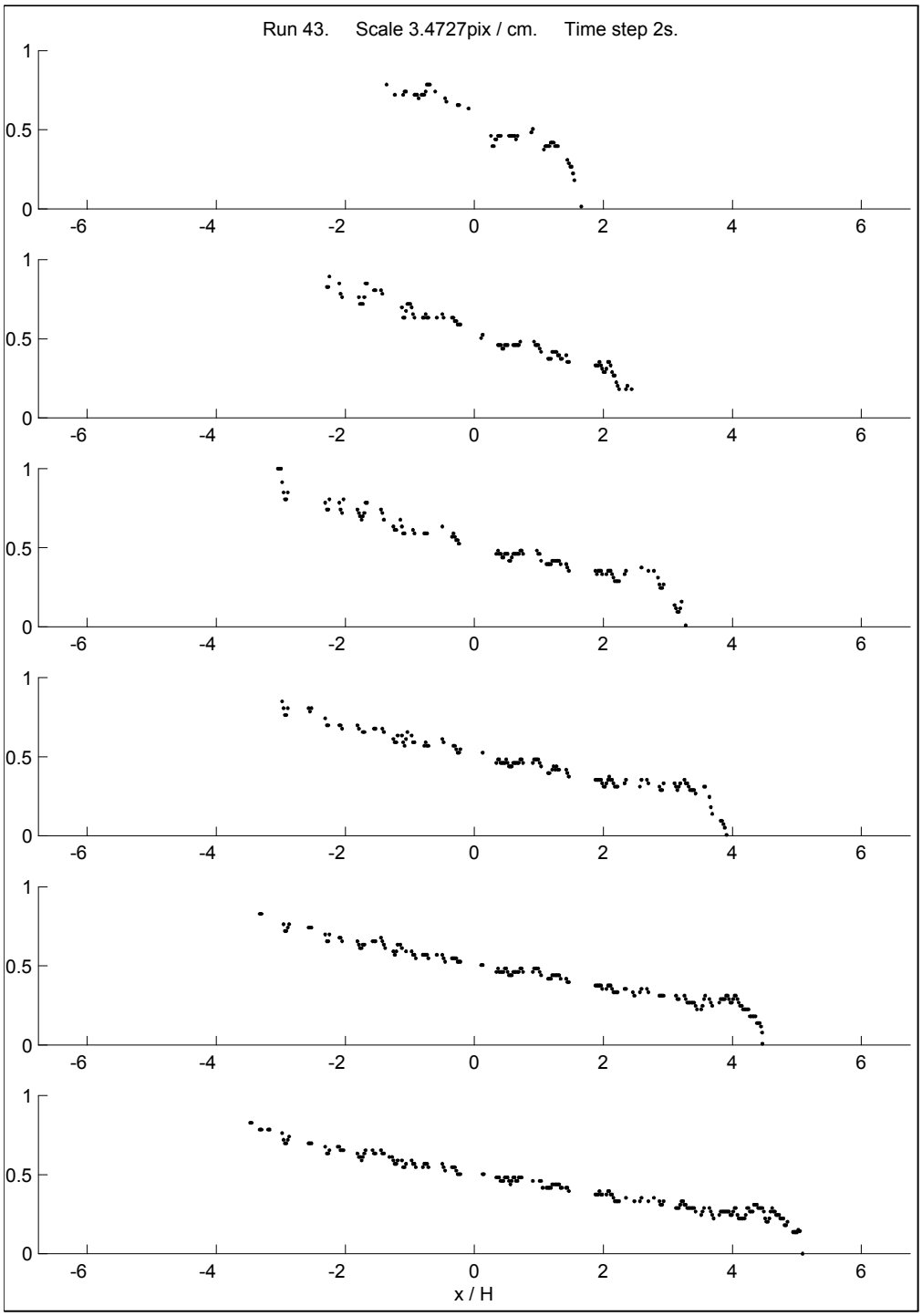

Figure C-37: Run 43.

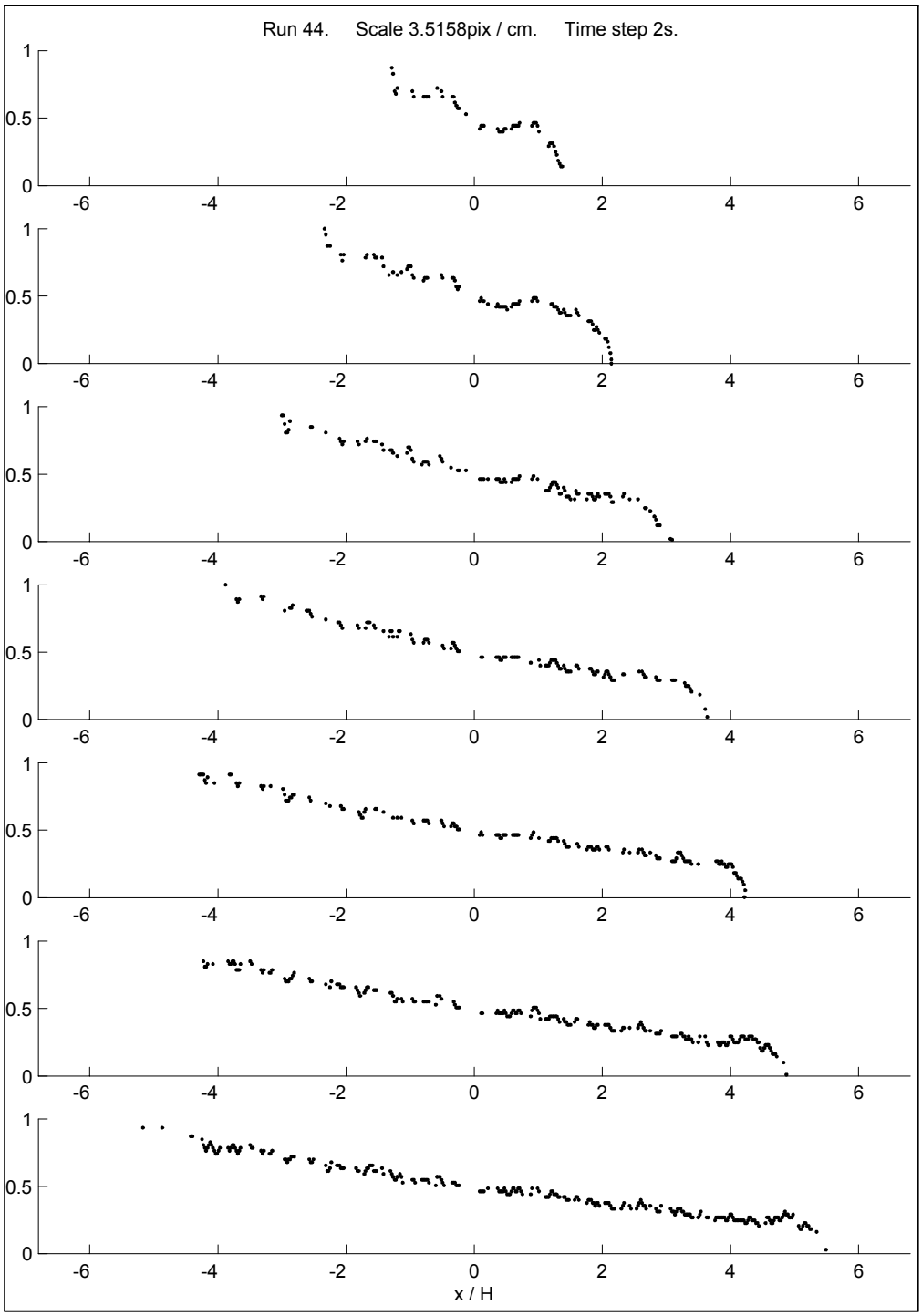

Figure C-38: Run 44.